NONLINEAR THERMOACOUSTIC OSCILLATIONS OF A DUCTED LAMINAR PREMIXED FLAME

Karthik Kashinath

Trinity College

Department of Engineering

University of Cambridge

A thesis submitted for the degree of

Doctor of Philosophy

August 2013

Declaration

This dissertation describes the work conducted in the Department of Engineering at the University of Cambridge, in fulfilment of the requirements for the degree of Doctor of Philosophy.

This dissertation is the result of my own work, and includes nothing which is the outcome of work done in collaboration except where specifically indicated in the text. No part of this dissertation has already been, or is being concurrently submitted for any other degree, diploma or qualification.

This dissertation contains approximately 40000 words and 60 figures.

....
Karthik Kashinath
8 October 2013

To my teachers.

Acknowledgements

I would like to thank my supervisor, Dr. Matthew Juniper, for his guidance and motivation during my PhD. His encouragement to pursue risky ideas led to some of the most exciting experiences during my doctoral study. I still struggle to say exactly what I mean when I write, but his emphasis on clear, precise and simple scientific writing has helped me understand and communicate my work better.

I would like to thank Dr. Santosh Hemchandra, my collaborator. I have found that an hour-long Skype chat with him is worth about a week in front of my computer. His enthusiasm has been infectious, despite the fact that we've only met thrice during my PhD.

I would also like to thank Iain Waugh. If not for his help, I would probably still be debugging my code. I would also like to thank Larry Li for his insight during the last phase of my PhD.

My thanks go to Simon Illingworth, with whom I have shared a significant amount of time discussing work and having fun. I would also like to thank Vikrant, Giulio, Outi, Luca, Alessandro, Chris and Ubaid, who have made my time at work and outside work memorable.

I would like to express my deep gratitude to my brother and my parents. Lastly, I owe a large amount of thanks to my partner, with whom I have shared the best, and the worst times, of my PhD.

Abstract

Finding limit cycles and their stability is one of the central problems of nonlinear thermoacoustics. However, a limit cycle is not the only type of self-excited oscillation in a nonlinear system. Nonlinear systems can have quasi-periodic and chaotic oscillations. This thesis examines the different types of oscillation in a numerical model of a ducted premixed flame, the bifurcations that lead to these oscillations and the influence of external forcing on these oscillations.

Criteria for the existence and stability of limit cycles in single mode thermoacoustic systems are derived analytically. These criteria, along with the flame describing function, are used to find the types of bifurcation and minimum triggering amplitudes. The role that the gain and the phase of the flame describing function play in determining the growth or decay of perturbations is identified. The choice of model for the velocity perturbation field around the flame is shown to have a strong influence on the types of bifurcation in the system. Therefore, a reduced order model of the velocity perturbation field in a forced laminar premixed flame is obtained from Direct Numerical Simulation. This model has a perturbation convection speed that is frequency-dependent and different from the mean flow, unlike the model commonly used in the literature. Limit cycles and bifurcations are found with both these models and it is shown that the model currently used in the literature precludes subcritical bifurcations and multi-stability in single mode thermoacoustic systems.

The self-excited thermoacoustic system is simulated in the time domain with several modes in the acoustics and analysed using methods from nonlinear dynamical systems theory. The transitions to the periodic, quasiperiodic and chaotic oscillations are via sub/supercritical

Hopf, Neimark-Sacker and period-doubling bifurcations. The trajectory of the system involves transient attraction and repulsion by one or more unstable attractors before the system reaches a stable state. Two routes to chaos are established in this system: the period-doubling route and the Ruelle-Takens-Newhouse route.

It is shown that the single mode system, which gives the same results as a describing function approach, fails to capture the period-2, period-k, quasi-periodic and chaotic oscillations or the bifurcations and multi-stability seen in the multi-modal case, and underpredicts the amplitude of period-1 oscillations.

Instantaneous flame images reveal that the wrinkles on the flame surface and pinch off of flame pockets are regular for periodic oscillations, while they are irregular and have multiple time and length scales for quasi-periodic and chaotic oscillations. Cusp formation, their destruction by flame propagation normal to itself, and pinch-off and rapid burning of pockets of reactants are shown to be responsible for generating a heat release rate that is a highly nonlinear function of the velocity perturbations. It is also shown that for a given acoustic model of the duct, several modes are required to capture the influence of this highly nonlinear unsteady heat release rate on the acoustics and the interactions between the acoustic modes via the unsteady heat release rate. Both of these are required to simulate the rich dynamics seen in experiments.

The infuence of external harmonic forcing, at different frequencies and amplitudes, on self-excited periodic, quasi-periodic and chaotic oscillations are examined. The bifurcations that lead to lock-in are either saddle-node or inverse Neimark-Sacker bifurcations. The transition to lock-in, the forcing amplitude required for lock-in and the system response at lock-in depend on the proximity of the forcing frequency to the natural frequency and whether the forcing frequency is above or below the natural frequency. At certain frequencies, even low-amplitude forcing is sufficient to suppress period-*1* oscillations to

amplitudes that are 90% lower than that of the unforced state. Therefore, open-loop forcing can be an effective strategy for the suppression of thermoacoustic oscillations.

This thesis shows that a ducted premixed flame behaves similarly to low-dimensional chaotic systems and that methods from nonlinear dynamical systems theory are superior to the describing function approach in the frequency domain and time domain analysis currently used in nonlinear thermoacoustics.

Contents

Chapter 1

Introduction

Many gas turbine combustion systems suffer from large-amplitude velocity and pressure oscillations [1]. These self-excited oscillations occur due to coupling between unsteady heat release and acoustic waves in confined spaces that can lead to resonance [1]. Unsteady combustion is an efficient source of acoustic waves and the boundaries of a combustor are acoustically closed and have little acoustic dissipation [2]. Therefore acoustic waves are reflected at the boundaries and they propagate back to the combustion zone perturbing the flame, which results in fluctuating heat release and further generation of acoustic waves. When the acoustic pressure fluctuations and the unsteady heat release are sufficiently in phase, the acoustic waves may be amplified [1; 3]. In gas turbine combustion systems the amplification can be very severe, because of the large energy density and small acoustic dissipation. This results in increased emissions, a deterioration in the performance of the gas turbine system, flame blowoff or flashback, and high heat transfer rates and highly energetic vibrations resulting in damage of the combustion chamber [1].

Modern gas turbines operate under lean premixed conditions in order to lower NO_x emissions by lowering the temperature in the combustion zone. Operating under lean premixed conditions, however, makes gas turbines highly susceptible to thermoacoustic oscillations [4]. Preventing these oscillations by avoiding operating conditions where they occur or controlling them to stay below acceptable amplitudes, therefore, are of great importance to gas turbine manufacturers. Thermoacoustic oscillations remains as one of the most challenging problems in gas turbine technology today.

Thermoacoustic oscillations may be controlled by either passive or active means [5]. Passive control uses damping mechanisms, such as Helmholtz resonators or perforated plates, to dissipate some of the acoustic energy or modification of the combustion system to alter time delays, combustor geometry or flame stabilization regions [1]. The use of passive control is constrained by the geometries of combustors and the limited range of frequencies over which passive control devices are effective. Active control aims to modify the feedback between the acoustics and the flame so that thermoacoustic oscillations decay [1]. Active control uses actuation that provides external energy to the system, and can be further divided into open-loop and closed-loop active control [6]. Open-loop active control does not use sensors for feedback and the forcing (actuation) does not depend on the measurement of any physical quantity [6]. Closed-loop active control uses sensors to measure physical quantities, controllers to determine the signal required to alter the feedback between the unsteady heat release and acoustics based on the input signal from the sensors, and actuators to alter some physical quantity based on the signal from the controller [7]. The limited accuracy and reliability of sensors in the harsh environment of combustors, and the limited speed, bandwidth and amplitude of actuators, however, makes their use difficult. Controller design is challenging because of large time delays, the noisy environment of combustors and the existence of multiple unstable modes [8; 9]. Active control of combustion oscillations remains an active area of research [1; 5; 10].

Both designing controllers and finding regions of safe operation of the system require good understanding of the dynamics of the system. The dynamics of the system depends broadly on two types of physical processes: (i) the feedback between the flame and the acoustics, which is responsible for feeding energy into the oscillations, and (ii) the damping within the system and at its boundaries, which is responsible for dissipating the energy. The mechanisms involved in the interaction between the flame and the acoustics often include hydrodynamic instabilities, gas dynamics, chemical reactions, heat transfer, multi-phase flows etc. Importantly, these mechanisms are not confined to the vicinity of the combustion zone [11]. They include a range of length scales because acoustic waves propagate much faster than the mean flow (in gas turbines) and boundaries far upstream or downstream of the combustion zone can affect the dynamics of the system. Likewise, hydrodynamic instabilities initiated in the injector cause perturbations that advect downstream at convection speeds of the order of the mean flow. When these arrive at the flame, they perturb the flame surface causing heat release rate fluctuations far downstream of the region of absolute instability. The mechanisms involved in dissipating energy include viscous and thermal losses in boundary layers, radiation of acoustic energy, and the interactions between acoustic waves, entropy waves and vorticity [12]. Therefore, understanding the underlying mechanisms that couple the unsteady heat release rate from flames and acoustic waves is a challenging task. The mechanisms responsible for driving thermoacoustic oscillations in gas turbine combustors and the interactions between these mechanisms, as well as those that cause damping, have been reviewed by Candel [10], Lieuwen [13] and Huang and Yang [14].

Besides understanding the mechanisms, the nature of these oscillations (e.g. periodic, quasi-periodic, chaotic) must also be understood to predict when they are likely to occur, how operating conditions must be changed to avoid their occurrence and whether they can be triggered by noise in the system. The onset of these oscillations is well understood using linear theories [3; 15; 16; 17]. However, the transient behaviour, the ultimate state reached by the system, and the susceptibility to triggering, which all depend on its nonlinear behaviour, are poorly understood.

1.1 Nonlinear thermoacoustics

Nonlinear thermoacoustics has been studied for over five decades. This field was actively researched during the 1960s and 70s because it was a persistent problem in rocket motors with liquid and solid propellants [18]. There has been renewed interest recently, incorporating research from nonlinear dynamics from the 1970s and 80s, which was not available to researchers in the 1960s and 70s.

1.1.1 Sources of nonlinearity in thermoacoustics

In solid and liquid propellant rocket motors, the primary source of nonlinearity is the gas dynamics. In rocket motors, the pressure perturbations are comparable to the mean pressure, therefore nonlinearities in the acoustics are important. Formation of weak shock waves is common [18; 19]. Culick [20] derived an analytical expression for the existence and stability of limit cycles using second-order nonlinearity in the gas dynamics. Subsequent studies considered other types of nonlinearity, including nonlinearities in the heat release rate response to velocity perturbations [21].

In gas turbine systems, however, the pressure perturbations are small compared to the mean pressure and the velocity perturbations are small compared to the speed of sound. Furthermore, the mean flow is small compared to the speed of sound. Therefore second and higher order terms involving the mean flow Mach number and perturbation Mach number in the nonlinear gas dynamic equations are negligible [18]. The primary source of nonlinearity in gas turbine systems is the nonlinear behaviour of the unsteady heat release rate from flames.

In gas turbines, the heat release rate is influenced more strongly by the velocity perturbations than by the pressure perturbations. This is because the pressure perturbations are small compared to the mean pressure, but the velocity fluctuations are not small compared to the mean flow [22].

In general, acoustic waves can interact with entropy and vorticity waves [16]. When the unsteady perturbations are small, however, the acoustics can be approximated to behave independently of each other, except at the boundaries and zones of heat release [16]. The generation of acoustic waves due to the acceleration of entropy waves in nozzles is an important mechanism of thermoacoustic oscillations [23], but is not the subject of this thesis.

Most modern gas turbine systems operate with lean premixed or partially premixed flames [13]. The heat release rate of a premixed flame depends on the following: (i) the density of the reactant flow, (ii) the burning rate or flame speed, (iii) the heat of reaction, and (iv) the flame surface area. Therefore the unsteadiness in the heat release rate depends on the fluctuations of these quantities. The fluctuations of the flame speed, in turn, depend on the perturbations in temperature, stretch rate and mixture composition of the reactant flow. The fluctuations in flame surface area depend on the disturbances that change the position and shape of the flame, which are due to fluctuations either in the flame speed or in the flow velocity. Finally, the fluctuations in the heat of reaction are due to perturbations in the mixture composition. A detailed discussion of the heat release rate response to fluctuations in each of these physical quantities is given by Lieuwen [12].

The mechanisms that cause heat release rate fluctuations in gas turbines are mainly due to velocity-coupling and equivalence ratio-coupling. The linear dynamics of these mechanisms have been studied extensively [24]. Several processes control the heat release rate nonlinearities in premixed flames. Figure 1.1, reproduced from Bellows' thesis [25], shows a typical example of the nonlinear dependence of the magnitude and phase of the unsteady heat release rate on perturbation velocity amplitude in a lean premixed gas turbine combustor.

The dynamics of premixed flames are nonlinear for the following reasons:

(i) the propagation of the flame normal to itself, also known as kinematic restoration, depends nonlinearly on the amplitude and wavelength of the flame wrinkle. The amplitude and wavelength of flame wrinkles, in turn, depend on the amplitude and frequency of velocity disturbances that perturb the flame [12].

(ii) The flame behaviour depends not only on the instantaneous velocity field around the flame but also on the history of the velocity perturbations [26]. This is because wrinkles generated on the flame surface are advected at the velocity tangential to the flame surface and propagate along the flame until they are destroyed by flame propagation.

(iii) Fluctuations in the velocity field can cause an oscillating flame surface to pinch off, which causes a sharp change in the flame surface area and, therefore, in the heat release rate [27].

(iv) Fluctuations in the velocity field cause local flow straining resulting in flame stretch, which affects the flame speed, and therefore the heat release rate, nonlinearly [28].

(v) In attached flames, the motion of the flame attachment point depends nonlinearly on the amplitude of velocity perturbations. At low velocity perturbation amplitudes, the attachment point does not move. At high perturbation velocity

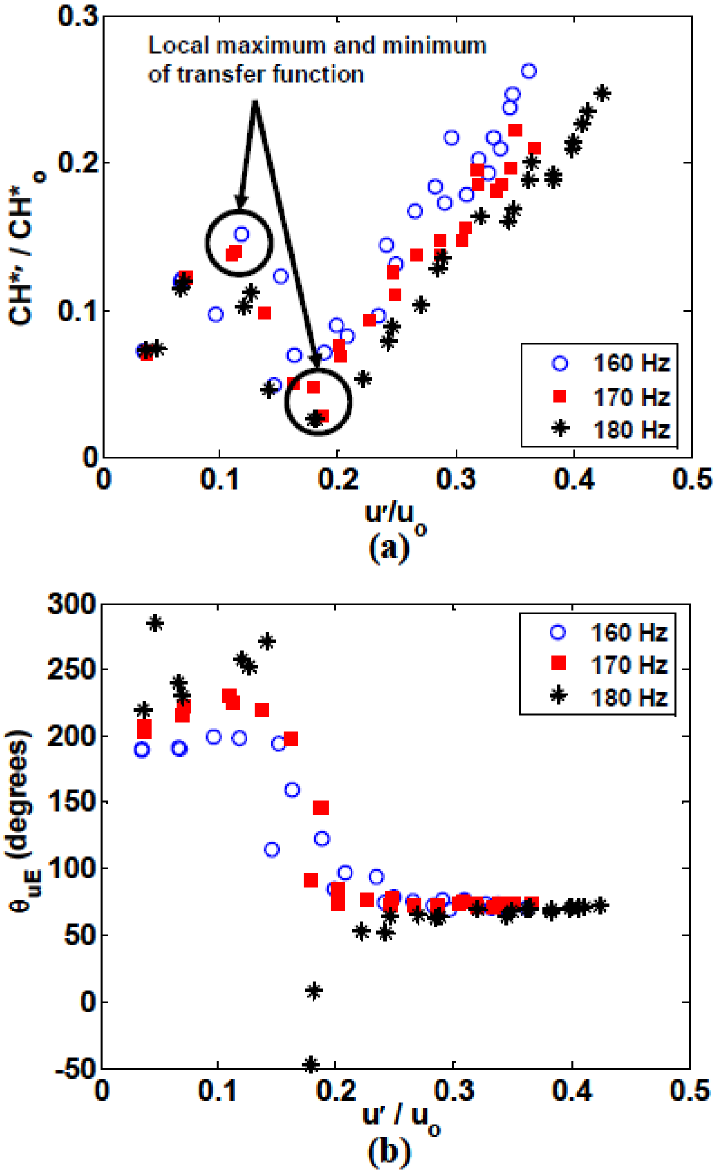

Figure 1.1: Nonlinear dependence of the unsteady heat release rate on velocity perturbation amplitude in a lean premixed gas turbine combustor: (a) Magnitude (b) Phase. Figure reproduced from Bellows' thesis [25].

amplitudes, however, the attachment point moves over a part of the cycle [29]. Furthermore, flashback may occur at high perturbation velocity amplitudes and this introduces an additional nonlinearity [27].

(vi) Flame geometry affects the degree to which local nonlinear effects influence the global nonlinearities in the heat release rate (integrated over the entire flame surface) [30; 31]. In a 2-D flame the contribution of points on the flame surface close to the attachment point and further downstream to the global heat release rate are the same. In an axi-symmetric flame, however, this depends on the flame shape (conical, wedge-shaped etc).

(vii) Fluctuations in the equivalence ratio cause fluctuations in the flame speed and heat of reaction, which are nonlinear functions of the equivalence ratio [32].

1.1.2 Nonlinear behaviour of thermoacoustic systems

The nonlinearities in the gas dynamics of rocket motors and combustion dynamics of gas turbines govern the transient and steady state behaviour (at long times) of the thermoacoustic oscillations. The simplest type of oscillation is a periodic oscillation or a limit cycle. Limit cycles are closed orbits in phase space and are characterized by a fixed period. The spectrum of a limit cycle can, however, contain more than one peak, *i.e.* limit cycles are not necessarily harmonic.

Often the nonlinear behaviour of thermoacoustic systems is explained in terms of amplification and damping terms [13; 31], as shown in Figure 1.2. In this figure, the amplitude dependence of the amplification and damping of acoustic energy are shown as $H(\epsilon)$ and $D(\epsilon)$ respectively. Limit cycles exist at the intersections of these two curves, where the net energy change over a cycle of the oscillation is zero. The amplification has often been taken to be the gain of the flame describing function [31]. In fact, it depends also on the phase. $D(\epsilon)$ represents the energy dissipation due to damping and is often assumed to be a linear function of the velocity perturbation amplitude in gas turbines. Damping can also behave nonlinearly, however, and this has been shown to be important in the dynamics of shock waves in rocket motors [33]. Nonlinear damping was later used by Culick and co-workers to explain the origins of subcritical bifurcations in thermoacoustics of rocket motors [18].

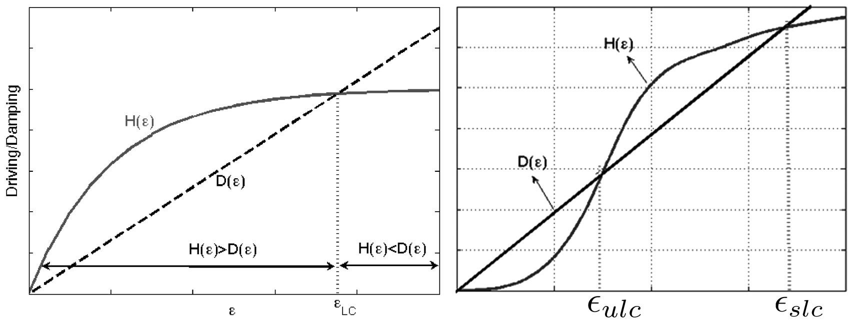

Figure 1.2: Amplitude dependence of acoustic driving curve, $H(\epsilon)$ and damping curve, $D(\epsilon)$, typically used to describe the nonlinear behaviour of thermoacoustic system qualitatively. (a) ϵ_{LC} marks the amplitude of stable limit cycle oscillations, (b) ϵ_{slc} and ϵ_{ulc} mark the amplitude of stable and unstable limit cycle oscillations respectively. Figure reproduced from Preetham *et al.* [31].

Studying the stability and bifurcations of the stable states of a nonlinear system is a useful way to understand its nonlinear behaviour quantitatively [34]. In this context, *stable* is used in the sense of asymptotically stable [35]. A bifurcation is a qualitative change in the steady state (long time) behaviour of a nonlinear system due to a change in an operating condition (control parameter) and occurs when a stable state becomes unstable [35]. Generally in thermoacoustics, a steady unperturbed state (fixed point) loses stability at a Hopf bifurcation and a branch of limit cycles originates at this point (Hopf point) in parameter space. These limit cycles can be stable or unstable. If they are stable the bifurcation is called a supercritical bifurcation, otherwise it is called a subcritical bifurcation. The branch of unstable limit cycles in a subcritical Hopf bifurcation sometimes undergoes another bifurcation called a fold bifurcation to become a branch of stable limit cycles. These bifurcations are shown in figure 1.3 for some control parameter R. On the vertical axis is the steady state amplitude of the system (half the peak-to-peak amplitude of limit cycle oscillations). Figure 1.3(a) shows a supercritical Hopf bifurcation, the solid curve originating at R_H, and figure 1.3(b) shows a subcritical Hopf bifurcation, the dashed curve originating at R_H, followed by a fold bifurcation at R_F. Figure 1.3(c) shows a supercritical Hopf bifurcation, followed by two fold bifurcations. These types of bifurcation have been seen in thermoacoustic systems [36; 37; 38].

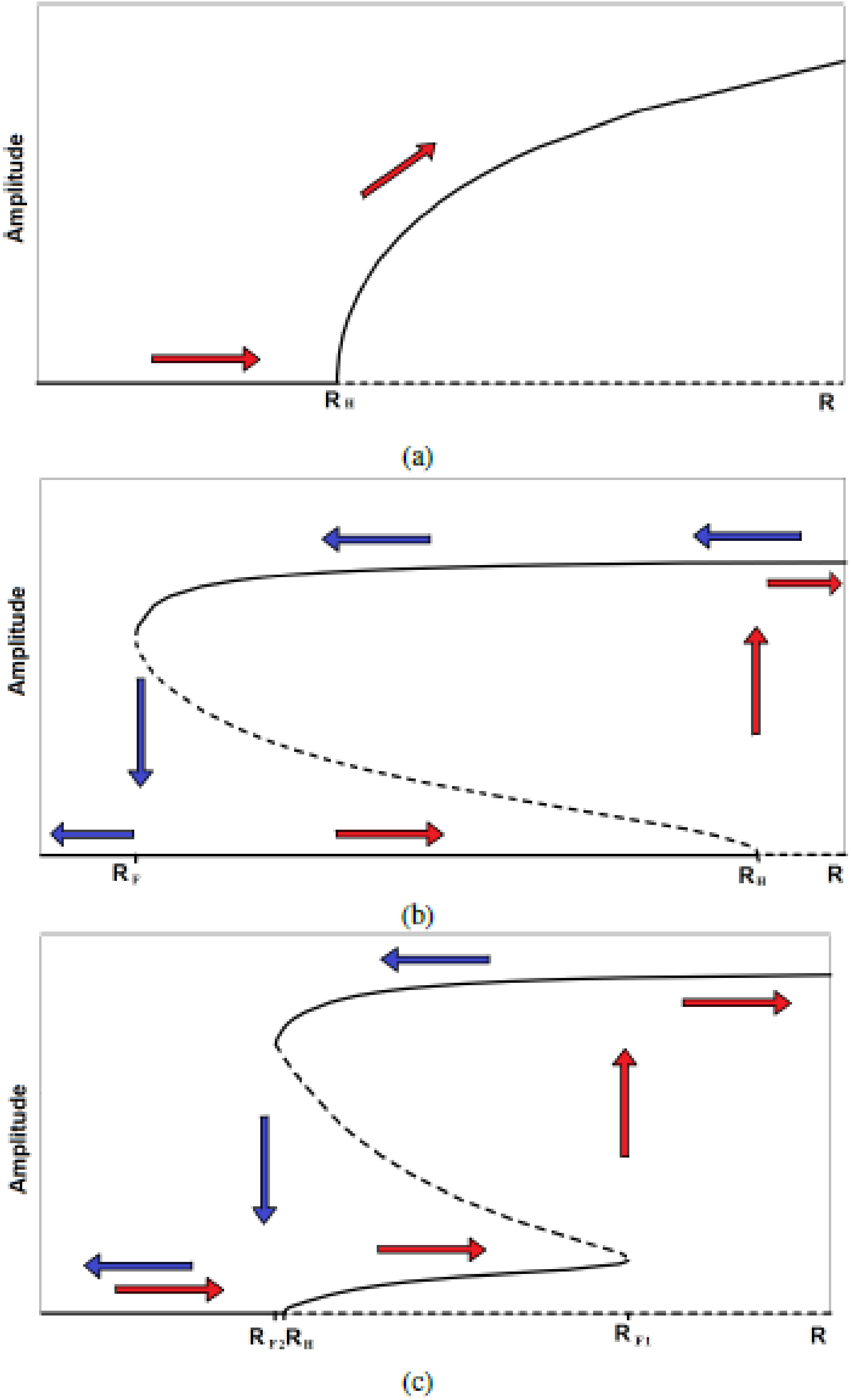

Figure 1.3: Hopf bifurcations to limit cycles. Figure reproduced from Campa and Juniper [39].

In figure 1.3(b) and (c) the system has a bi-stable region, where a sufficiently large impulse can pulse the system from one stable state to another [40]. This is called triggering. In figure 1.3(b) the system can be triggered from the stable fixed point to a stable limit cycle and in figure 1.3(c) the system can be triggered from one stable limit cycle to another. Triggering may be induced by noise or by a carefully designed pulse from an actuator. The system also exhibits hysteresis in a bi-stable region. These are shown the by the red and blue arrows in figure 1.3. The red arrows indicate the path of the system when the control parameter R is increased (from left to right), while the red arrows indicate the path when it is decreased.

1.1.3 Triggering in thermoacoustics

Triggering was first studied in thermoacoustics by Crocco *et al.* [18]. Triggering was commonly observed in rocket motors and has been researched extensively in both solid and liquid rockets [18]. Since these early works, triggering has been analysed in several other systems due to subcritical bifurcations of the dynamical states of the system [41; 42]. They have also been seen in gas turbine systems [37; 43; 44].

Early attempts to explain this phenomenon in rocket motors focussed on gas dynamic nonlinearities because these were significant in rocket motors where the pressure perturbations are comparable to the mean pressure [18]. Lores and Zinn used an n-τ model for the (linear) heat release rate but were unsuccessful in predicting triggering [45]. They mention that their analysis can be repeated for a nonlinear combustion model but do not pursue this because no reliable nonlinear combustion models were developed at the time. One of the main conclusions of the studies on triggering from the 1960s through the 90s was that nonlinear gas dynamics alone was insufficient to explain triggering because this form of nonlinearity only transfers energy from low frequency modes to high frequency modes as the amplitude increases [46]. Therefore nonlinear combustion had to be included.

The first nonlinear combustion model that successfully explained the phenomenon of triggering was by Levine and Baum and used a nonlinear combustion model of the form $q \sim |u|$ [21]. Wicker *et al.* showed that triggering could be explained using models of the form $q \sim u^2$ or $q \sim pu$ [47]. More recently, triggering in an electrically driven Rijke tube has been investigated using a heat release model of the form $q(t) \sim |u(t-\tau)|$ where τ is a time delay [42; 48; 49; 50; 51]. Triggering in a ducted diffusion flame model was studied by Balasubramanian and Sujith [52] and recently revised by Magri *et al.* [53].

In gas turbine systems, where the acoustics may be treated linearly, triggering occurs due to nonlinear combustion or nonlinear damping. A necessary and sufficient criterion for triggering due to nonlinear combustion was derived recently by Juniper using a weakly nonlinear analysis around the Hopf point [54]. The nonlinear combustion model in that study is a general function of the amplitude of the fundamental acoustic mode with a time delay, a commonly used model in gas turbine combustors, although the time delay is required to be small in that study.

In single mode thermoacoustic systems, the minimum amplitude of a pulse required for triggering is given by the amplitude of the unstable limit cycle at that operating point (the dashed lines in figure 1.3(b) and (c)). Triggering and hysteresis have been investigated recently in experiments on thermoacoustic systems with premixed flames [44; 55; 56; 57]. Noiray *et al.* and Boudy *et al.* find the minimum amplitude for triggering using a describing function analysis. Kabiraj *et al.* find the same experimentally by forcing their system from its stable fixed point using harmonic perturbations of increasing amplitudes, for a fixed duration [56]. In their experiments, once the forcing was switched off, the system either decayed back to the stable fixed point or grew on to the stable periodic solution. The critical amplitude at which this transition occured was the minimum triggering amplitude.

Triggering can sometimes occur due to excitation from low levels of background noise [37]. This has been attributed to non-normality [54]. This is because the low levels of background noise that cause triggering appear to have much smaller amplitudes than those of the unstable limit cycles estimated from a single mode analysis. Non-normality causes transient growth of perturbations in a linearly stable regime until nonlinear effects become important and determine the dynamics of the system. In a recent study Juniper draws an analogy between bypass transition in hydrodynamics and triggering in thermoacoustics [50]. Noise-induced transition to instability has been investigated in a Rijke tube theoretically by Waugh and Juniper [58]. They find the type of noise that is most effective at causing triggering. The mechanisms they find are in good agreement with experimental work by Jegadeesan and Sujith on a ducted diffusion flame [59].

In general, nonlinear thermoacoustics involves the interaction between several modes. Even when non-normality is not considered, the minimum amplitude required for triggering is not simply the amplitude of the unstable attractor [60]. The type of impulse that can cause triggering depends strongly on the distribution of energy among the different modes and their relative phases. This was noticed in experiments by Wicker *et al* [47] and in recent simulations by Waugh *et al* [58]. In nonlinear dynamics the minimum impulse is defined more precisely and depends on the depth of the potential well of an attractor in a n-dimensional phase space [35].

Furthermore, in general, nonlinear thermoacoustic systems can have several unstable states at each operating condition [56]. In such cases, the minimum excitation that causes transition from one steady state to another depends strongly on the trajectory of the system, which can be complex. Therefore triggering mechanisms can be quite elaborate.

1.1.4 Elaborate nonlinear behaviour

Hopf bifurcations are not the only types of bifurcation observed in thermoacoustics. Nonlinear systems can have bifurcations that lead to period-2^n, period-k, quasi-periodic and chaotic oscillations. A detailed discussion of the bifurcations of nonlinear systems is given by Guckenheimer and Holmes [35] and Thompson and Stewart [61].

The first observations of quasi-periodicity in thermoacoustics were by Sterling and Zukoski in their experiments on a dump combustor [41]. They attributed this behaviour to the time delays associated with vortex roll-up, mixing and reaction. Subsequently, these experiments were modelled by Sterling using linear acoustics and two nonlinear combustion models: (i) an amplitude dependent time-delay and

(ii) a twice-kicked nonlinear oscillator to model the behaviour of the heat release in their experiments [62]. Sterling showed that limit cycles undergo period-doubling bifurcations and transition to chaos. Jahnke and Culick applied techniques from dynamical systems theory to find bifurcations of limit cycles [36]. They used a linear combustion model but nonlinear gas dynamics and 6 coupled modes in their discretization of the acoustics. They showed that a branch of limit cycles undergoes a torus birth bifurcation to quasi-periodic oscillations.

More recently, Lei and Turan used a discrete version of Sterling's models and introduced an additional time-delay associated with the vaporization of fuel droplets [63]. Their model showed, as in Sterling's analysis, the classic cascade of period-doubling bifurcations to chaos. Subramanian *et al.*, using tools from dynamical systems theory and nonlinear time series analysis, showed the same transition to chaos in their model of a horizontal Rijke tube [49].

Recent experiments by Kabiraj *et al.* show the elaborate nonlinear behaviour of a ducted laminar premixed flame [56; 64; 65]. Kabiraj *et al.* have shown that their thermoacoustic system can have period-2^n, period-k, quasi-periodic and chaotic oscillations depending on the operating conditions [56]. They have also shown different routes to chaos in their system [64]. In a recent study they show the role of intermittency in their system, which leads to blowout of their premixed flame [65]. When they change the flame position inside the duct they find that limit cycle oscillations lose stability via a torus birth bifurcation and quasi-periodic oscillations are observed. On changing the flame position further, the quasi-periodic state undergoes a transition to intermittency (a type of chaos), which is observed as repeated lift-off and reattachment, ultimately leading to flame blowout. Recent experiments by Gotoda *et al.* on industrial-scale lean premixed gas turbine combustors show that these systems behave similarly. In particular, they show the presence of low-dimensional chaos and quasi-periodicity in the thermoacoustic oscillations in their system [66; 67].

From the above studies it is evident that elaborate nonlinear thermoacoustic behaviour is not uncommon, even in simple systems. The analysis of these types of oscillation and their bifurcations require tools from dynamical systems theory and nonlinear time series analysis.

1.2 Simulating thermoacoustic systems

The starting point for numerical analysis of thermoacoustic systems is the governing equations of the unsteady reacting flow in combustion chambers. The computational cost usually determines the extent of modelling necessary before the equations can be solved. The computationally most expensive technique is direct numerical simulation (DNS). Here, the governing equations are integrated from a set of initial conditions to study the time evolution of the system. All the scales of motion are resolved on a very fine grid with very small time-steps.

Techniques in reacting flow CFD (LES, PDF, CMC, URANS etc) are the next most expensive and require models for one or more physical processes such as turbulence, chemistry, heat transfer, compressibility effects etc. While these methods provide a high level of detail about the dynamics of the system, there are a few drawbacks about such high order methods: (i) they are computationally expensive, (ii) usually only the most unstable mode of oscillation can be identified, and (iii) appropriate acoustic boundary conditions are hard to implement [11].

Reduced order modelling (ROM), which is the next lower level of complexity, aims to capture the main physical processes governing the dynamics of the system while neglecting all other processes or accounting for them in an *ad-hoc* manner. This requires good understanding of the dominant physical processes in a given problem. In the analysis of nonlinear thermoacoustics, such methods aim to capture the main nonlinearities in the system, while approximating other processes. For example, when premixed flame dynamics in thermoacoustic systems are modelled using the G-equation model, the flame is approximated to be a thin surface separating the reactants and products and the influence of gas expansion across the flame front on the flow upstream of the flame is neglected [68]. The main nonlinearities in the flame dynamics (§1.1.1) such as kinematic restoration, the formation and destruction of cusps, and the pinch-off of flame pockets, however, are captured well. With the advent of fast computers, reacting flow CFD has become more common, however, generalizing the results of CFD to gain fundamental understanding still remains a challenging task. ROM aims to fill this gap by providing quick results that can be analysed to draw fundamental conclusions about the behaviour of a system.

1.3 The wave equation

In the analysis of thermoacoustics, the mean flow and perturbation are usually considered separately, even when the perturbation is not small [18]. The perturbation equations are combined to obtain the inhomogeneous wave equation for the pressure, with source terms for the unsteady heat release rate. A detailed discussion of the role of gas dynamic nonlinearities in the wave equation is given by Culick [18].

Dowling compares the different methods of solving the wave equation and discusses the effects of unsteady heat input, mean flow, drag forces and distributed heat input on the solutions obtained using different methods [22]. The two most common approaches are (i) d'Alembert's solution with matching conditions across discontinuities (the wave approach), (ii) the method of spatial averaging.

1.3.1 The wave approach

The wave equation can be solved using left and right travelling waves (in the 1-D case), also known as d'Alembert's solution [69]. In this approach non-trivial boundary conditions and variable speed of sound can be handled conveniently. This method facilitates a description of the entire geometry of the system as a network of elements with suitable matching conditions at interfaces, boundaries and across discontinuities such a temperature jumps [70]. Damping is accounted for in the boundary conditions or in the governing equations.

This approach is used widely in thermoacoustics, especially in the gas turbine industry, and is commonly known as thermoacoustic network analysis [70; 71]. A description of the acoustic elements and boundary conditions is usually obtained in the frequency domain, either theoretically or from experiment. As mentioned in §1.1.1, the main source of nonlinearity in gas turbines is the flame. A nonlinear analysis using the wave approach can be done in the frequency domain, where the flame describing function (FDF) is used to characterise the nonlinear heat release rate from the flame, or in the time domain, where the Green's function and a nonlinear time domain model of the flame are used.

1.3.1.1 Flame describing function approach

The main assumptions of the FDF approach are (i) the harmonics of the unsteady heat release rate are filtered out by either the flame or the acoustics, or (ii) the higher harmonics generated by the flame are small [55]. Therefore the acoustic oscillations are assumed to be purely harmonic. The FDF is calculated, experimentally or theoretically, by forcing the flame with harmonic acoustic velocity perturbations and measuring the heat release rate response. In general, the heat release rate response contains a response not only at the forcing frequency but also at higher or lower frequencies due to nonlinear processes. In this approach, however, the harmonics are discarded and only the response at the forcing frequency is retained. This process is repeated at several frequencies and amplitudes. Hence, at each forcing amplitude, the FDF is a single-input single-output transfer function. Thus the nonlinear response of the flame to harmonic velocity perturbations is reduced to an amplitude-dependent gain and phase. Physically, the gain represents the amplification, and the phase represents the delay, in the response of the flame to acoustic forcing. The DF is then coupled with the linear acoustic system to yield a dispersion relation that is solved in the frequency domain or using methods from control theory. The describing function (DF) was first applied to thermoacoustics in rocket motors by Natazon and co-workers in the 1970s in USSR [72]. They called it the method of harmonic linearization. For thermoacoustics in gas turbines it has was first applied analytically by Dowling [27; 73] and later to an experiment by Noiray *et al* [55].

Although widely used, this approach is not always accurate. Subramanian *et al.* show that the system behaviour predicted using the DF approach is quantitatively as well as qualitatively different from that seen using time domain simulations of simple thermoacoustic systems [74]. They point out that using a two-part approach and a modal analysis fail to capture the intricate coupling between combustion and acoustics. This is because the higher or subharmonics generated by the flame are not negligible in many cases and are not filtered out by the acoustics.

1.3.1.2 Green's function approach

The Green's function approach has been described clearly by Stow and Dowling [75]. Once the geometry and boundary conditions of the combustor are characterised using a network model, a transfer function for the response of flow perturbations to heat release rate fluctuations is found. An inverse Fourier transform is applied to convert this transfer function into the time domain to obtain the Green's function, which relates the unsteady flow to the unsteady heat release rate at previous times. This is combined with a nonlinear flame model that relates the unsteady heat release rate to flow perturbations to obtain a complete time domain model of the system. Stow and Dowling applied this method to a model of a gas turbine combustor using a simple saturation model for the nonlinear heat release rate [75]. They show the influence of harmonics and the interaction and exchange of energy between different modes. In their study they found that the time domain and frequency domain results matched well. This was because the harmonics were not significant for the geometry and flame model they considered. The point out that if a harmonic happened to be close to another unstable mode, it could have an important effect. More recently, the Green's function approach has been applied to longitudinal and annular combustors with a nonlinear flame model called the 'flame-tracking approach', which is based on the G-equation [76; 77].

1.3.2 Method of spatial averaging

The method of spatial averaging converts the wave equation, a partial differential equation, to a system of ordinary differential equations (ODE) by using a suitable basis for series expansion of the physical variables and integrating over a volume. In theory, infinitely many terms are used in the series expansion, but in practice the series is truncated at some point. Therefore the results are approximate. This method was first applied to the acoustic wave equation by Powell and Zinn [78]. They used the orthogonal eigenmodes of the homogeneous wave equation as the basis functions. This method is called the Galerkin method. Essentially, this models the system as a set of coupled nonlinear oscillators, each associated with one of the classical acoustic modes of the chamber [18]. Interpreting each oscillator as an acoustic mode is only approximate, however, because the basis functions only satisfy the wave equation with homogeneous boundary conditions. The advantage of this method stems from the spatial averaging technique, which makes handling different geometries and physical processes convenient [18].

In general, the motions of the oscillators may be coupled by linear as well as nonlinear processes, although linear coupling is less important [18]. This is because the linear coupling terms are proportional to the square of the Mach number of mean flow, which can be neglected for flows with low Mach numbers, as in gas turbines. The nonlinear coupling terms arise from nonlinearities in the gas dynamics, the unsteady heat release rate and nonlinear damping [18].

The set of second order ODEs obtained by spatial averaging may be simplified if the timescales of the acoustic oscillations are much smaller than the timescales over which their amplitudes and frequencies evolve. Then a method called two-timing may be applied to study the dynamics of these scales separately [34]. This reduces the set of coupled second order equations obtained from the method of spatial averaging to a set of coupled first order equations in the amplitude and frequency change (slow phase) of the oscillations [18]. This has recently been applied to a weakly nonlinear analysis of thermoacoustics [54] and to an investigation of the stability of standing and spinning modes in annular combustors [79].

The method of spatial averaging was used by Culick to predict the nonlinear behaviour of rocket motors. He used a single mode approximation with nonlinear damping and neglecting gas dynamic or heat release rate nonlinearities [40]. This was unsuccessful because the higher harmonics were not negligible and systems having many degrees of freedom had to be used. This was resolved in a subsequent study where a system of coupled nonlinear oscillators was solved numerically to predict nonharmonic limit cycles [20].

Awad and Culick included gas dynamic nonlinearities in their analysis using this method. In the single-mode analysis with only gas dynamic nonlinearities, the nonlinear terms disappear [80]. This is not true, however, when nonlinear combustion is included because the nonlinearity is in the heat source term [81].

Nonlinear mode coupling was investigated by Culick and co-workers using the two-mode approximation and gasdynamic nonlinearities [36; 80; 82; 83]. They showed that stable and unstable limit cycles exist. One of their conclusions was that using only two modes limits the energy transfer between modes and affects the transient dynamics of the system. They mention that unless the initial conditions of their simulation are close to the stable state, the results of their analysis may be incorrect [82].

Ananthkrishnan, Deo and Culick showed that 8 modes are necessary to correctly describe the coupling between two linearly unstable modes with gas dynamic nonlinearities [38]. This is because the number of modes used determines the energy transfer between the modes. Initially one or more of the lower modes become unstable and their energy grows exponentially. When the amplitudes are no longer small the nonlinearities transfer energy to the higher modes, thus limiting the amplitude growth and establishing a limit cycle. They emphasized that this result depends on the type of nonlinearity included in the model. This condition is not necessary, however, when nonlinear combustion models are used because the energy transfer mechanisms are different. They also conclude that their system is stable when each nonlinear oscillator is stable. In general, however, stability limits obtained from the analysis of each mode indivdually can differ from stability limits obtained by a multi-mode analysis. The necessary and sufficient condition for linear stability is given by the Routh-Hurwitz stability criterion [84]. This was applied by Awad and Culick to a two-mode system [80].

In general, many terms must be included in the expansion to accurately capture the behaviour of a thermoacoustic system [70]. The resulting set of ODEs for the system of coupled oscillators is solved numerically, either by direct time-marching or by using continuation methods [51]. In a continuation method, the general technique is to fix all parameters of the system but one and track the steady states of the system as a function of this parameter [36]. Continuation methods can be used to track fixed points, as well as limit cycles, and their bifurcations [85]. Continuation methods were first applied to thermoacoustics by Culick and co-workers [36]. The methods in these studies are only feasible in systems with a few variables [38]. Recent work by Waugh shows how matrix-free continuation can be used successfully for large thermoacoustic systems with several thousand variables [60].

1.4 Nonlinear interactions between forced and self-excited oscillations

In previous sections the nonlinear behaviour of self-excited thermoacoustic systems and methods to analyse them have been described. When nonlinear oscillations in a self-excited system are subjected to external forcing, the response of the system depends on the interaction between the forcing and the self-excited oscillation. When the amplitude of forcing is sufficiently large, usually ‘lock-in’ occurs, where the self-excited system loses its natural frequency and follows the forcing. This nonlinear phenomenon was observed in thermoacoustics by Lieuwen and Neumeier [86]. Bellows *et al.* notice the same phenomenon in their experiments on a swirl-stabilized lean premixed combustor. They examined some aspects of the nonlinear interactions between acoustic forcing and self-excited thermoacoustic oscillations [25; 43]. They also found that, at some operating points, the overall acoustic power was substantially reduced due to the external forcing and this occured when the self-excited system locked into the forcing. The forcing frequencies in their study were not close to the natural frequency of the system.

There are a few studies that have investigated the success of open-loop forcing in suppressing thermoacoustic oscillations. Prasanth *et al.* used low-frequency modulation of the fuel-injection to suppress oscillations in their model combustor [87]. Their study based on a linear model gave some guidelines for fuel-injector pulsing strategies, as well as the number of fuel injectors and their locations, for optimal suppression of pressure oscillations. The presence of hysteresis was used by Knoop *et al.* to devise a low-frequency pulsing strategy to suppress oscillations. These studies only examined low-frequency equivalence ratio pulsing far away from the natural frequency of the system.

Recent experiments in a self-excited hydrodynamic system [88] have shown that the system can lock into forcing when the forcing frequencies are close to the natural frequency. It has also been shown that the transition to lock-in can be elaborate and occurs via a sequence of bifurcations [88]. Furthermore, the system response (amplitude of oscillations) once it locks into the forcing can be significantly lower than the natural unforced state. Such behaviour is well known in nonlinear dynamics [89]. Lock-in has been proposed as a means of suppressing flow oscillations based on theory [90] and experiments [91]. A similar strategy may be successful in thermoacoustics as well.

1.5 Scope of the thesis

Finding limit cycles and their stability is one of the central problems of nonlinear thermoacoustics. The first aim of the thesis is to find an analytical expression for the amplitude and stability of limit cycles in single mode thermoacoustic systems. Along with the flame describing function, this expression can be used to determine the types of bifurcation in such systems and to estimate the minimum amplitude required to trigger a single-mode system into stable limit cycle oscillations. Furthermore, it can be used to show the precise role of the gain and phase of the FDF on the nonlinear behaviour of single mode systems.

Hydrodynamic instabilities play an important role in thermoacoustics because they influence the dynamics of the flow field around the flame. In particular, in laminar premixed flames, acoustic waves induce velocity perturbations at the base of the flame by exciting a convectively unstable shear layer. These velocity perturbations then travel along the flame, distorting its surface and therefore causing flame area fluctuations that result in unsteady heat release rate oscillations. The velocity perturbations are modelled by a travelling wave in thermoacoustic models that use the G-equation model for the flame. The second aim of the thesis is to confirm the validity of this model using direct numerical simulation and to determine the influence of the speed of these travelling waves on the nonlinear dynamics of thermoacoustic systems.

Recent experiments in a ducted laminar premixed flame [56] and in industrial gas turbine combustors [66] reveal that the nonlinear behaviour of thermoacoustic systems is elaborate. In particular, Kabiraj *et al.* find that their system undergoes several bifurcations resulting in quasi-periodic, frequency-locked and chaotic oscillations and has different routes to chaos [64]. Such behaviour has not been simulated using realistic flame models. The third aim of the thesis is to simulate the elaborate nonlinear behaviour in this system, to characterize this behaviour using dynamical systems theory and nonlinear time series analysis and to interpret this behaviour using instantaneous flame images of different types of oscillation. Furthermore, the thesis aims to compare time domain calculations using a single mode in the acoustics, which is equivalent to the flame describing function approach, against time domain calculations using several modes in the acoustics.

Self-excited nonlinear systems exhibit synchronization, the phenomenon in which a system changes its frequency due to external forcing. Suppressing self-excited nonlinear oscillations by applying external forcing has been proven to be successful in several nonlinear systems. These phenomena have received little attention in the field of thermoacoustics. The fourth aim of the thesis is to identify synchronization phenomena in thermoacoustics within the framework of nonlinear dynamics and to explore the potential of external forcing in suppressing self-excited thermoacoustic oscillations.

Nonlinear dynamical systems theory and nonlinear time series analysis offer many tools to characterize and interpret elaborate nonlinear behaviour. Few studies in thermoacoustics have used such analyses. An overall aim of the thesis is to compare their utility against frequency domain and time domain techniques currently used in nonlinear thermoacoustics.

1.6 Structure of the thesis

Chapter 2 describes the models and methods used in this thesis. The rest of the thesis is divided into three parts. Chapters 3 and 4 form part one, chapter 5 is part two and chapter 6 is part three.

Each chapter is an article that has either been published or has been submitted for publication, with minor changes. All the articles were written by Karthik Kashinath with input and feedback from the other authors. The DNS code for article 2 was written by Santosh Hemchandra and simulations were run by him. The articles are:

1. “Nonlinear phenomena in thermoacoustic systems with premixed flames”,
Karthik Kashinath, Santosh Hemchandra, Matthew Juniper
ASME Journal of Engineering for Gas Tubines and Power, Vol.135, 061502, 2013.

2. “Nonlinear thermoacoustics of ducted premixed flames: the influence of perturbation convection speed”,

Karthik Kashinath, Santosh Hemchandra, Matthew Juniper
Combustion and Flame, (in press)
3. “Nonlinear self-excited thermoacoustic oscillations of a ducted premixed flame: bifurcations and routes to chaos”,
Karthik Kashinath, Iain Waugh, Matthew Juniper
Journal of Fluid Mechanics (submitted).
4. “Nonlinear oscillations in a self-excited thermoacoustic system: the influence of external open-loop forcing”,
Karthik Kashinath, Matthew Juniper
Journal of Sound and Vibration (in preparation).

The thermoacoustic system investigated in this thesis is a slot-stabilized 2-D laminar ducted premixed flame. The level set solver for the G-equation was originally written by Santosh Hemchandra during his PhD at Georgia Tech [26]. Coupling the flame with a model for the acoustics was done by Karthik Kashinath. More recently, Iain Waugh and Karthik Kashinath have made several other modifications to the code, when Iain Waugh applied continuation analysis to the ducted premixed flame in 2012/13 [60].

Chapter 2 contains a description of the model for the acoustics, which uses the Galerkin method, and a description of the model for the flame, which is a kinematic model based on the level set approach (the G-equation).

In chapter 3 analytical criteria are derived for the amplitude and stability of limit cycles. The types of bifurcation and triggering amplitudes are found. The role of the gain and the phase of the flame describing function on the growth or decay of perturbations is identified. The results in this chapter show that the choice of velocity model strongly influences the types of bifurcation in the system. Chapter 4 therefore focuses on finding a reduced order model of the velocity perturbation field in a forced laminar premixed flame from Direct Numerical Simulation (DNS). The criteria derived in chapter 3 are applied to the thermoacoustic system, but with the reduced order model of the velocity perturbation field. These criteria are also applied to the thermoacoustic system with a model of the velocity perturbation field commonly used in the literature. The results from the two sets of simulations are compared and the influence of the choice of velocity model on the nonlinear behaviour of the system is identifed. The results in the first part of the thesis show some of the limitations of single-mode approaches.

The second part of the thesis therefore focuses on simulating the system in the time domain with several modes in the acoustics. Chapter 5 introduces techniques from nonlinear dynamical systems theory and nonlinear time series analysis, which are applied to characterise the self-excited behaviour of the model. The bifurcations that result in different types of oscillation: periodic, quasiperiodic and chaotic, are identified. The influence of the number of modes in the acoustics on the bifurcations of the system is examined. The transient behaviour of the system is analysed and the role of unstable attractors in the system's trajectory from the fixed point to its stable states is highlighted. The routes to chaos in this system are established. Instantaneous flame images are used to examine the different types of oscillation. Finally, the origins of the elaborate nonlinear behaviour is explained.

The third part of the thesis (chapter 6) focuses on the infuence of external harmonic forcing, at different frequencies and amplitudes, on self-excited periodic, quasi-periodic and chaotic thermoacoustic oscillations. The sequence of bifurcations leading up to lock-in are identified using tools from dynamical systems theory and nonlinear time series analysis. The stability of the locked-in state is examined. The implications of the response of the system at lock-in for the suppression of thermoacoustic oscillations is emphasized.

The thesis ends with conclusions and suggestions for future work.

Chapter 2

Methodology

Summary

This chapter describes the models and methods used in this thesis. The acoustics of planar waves in the tube are governed by linearised momentum and energy equations. The flame is modelled using a nonlinear kinematic model based on the G-equation. Open-loop forced simulations are used to calculate the flame describing function (FDF). Time domain simulations of the coupled thermoacoustic system are performed with a Galerkin discretization for acoustic pressure and velocity.

Nomenclature

G	Level set function
L_f	Nominal flame height
L_0	Length of duct
x_f	Flame position in the duct normalised by length of duct
R	Half-width of slot burner
u	Streamwise velocity
v	Transverse velocity

u_0	Mean streamwise velocity
u_c	Disturbance convection speed
c_0	Speed of sound
M	Mach Number
p	Pressure
s_L	Laminar flame speed
h_R	Heat of reaction per unit mass
$\dot{Q}$	Heat release rate
$\dot{Q}_0$	Mean heat release rate
β_f	Flame aspect ratio, L_f/R
ζ	Damping parameter
c_1	Damping factor corresponding to acoustic radiation
c_2	Damping factor corresponding to boundary layer losses
ρ	Density
γ	Ratio of specific heats
δ	Dirac-delta distribution
ϕ	Equivalence ratio

2.1 Model for the acoustics

For simplicity, the acoustic chamber in the thermoacoustic system considered here is a duct of length L_0 open at both ends with a slot-stabilized 2-D laminar premixed flame located at a distance $\tilde{x}_f$ from one end. Fig. 2.1 shows a schematic. The base flow velocity is $\tilde{u}_0$, the pressure is $\tilde{p}_0$ and a constant mean density assumption is invoked so that the mean density, $\tilde{\rho}_0$, and speed of sound in the unburnt mixture, $\tilde{c}_0$, remain constant everywhere in the duct. The Mach number, $M \equiv \tilde{u}_0/\tilde{c}_0$, is assumed to be small and hence nonlinear effects in the acoustics are negligible [27]. This is a reasonable assumption for gas turbine combustors [27]. Furthermore, the Mach number is assumed to be much less than unity, $M \ll 1$, hence terms involving u_0 may be neglected. A compact flame assumption is used here because the flame length is small compared to the wavelengths of the duct's acoustic modes. The duct width is large compared to the slot width, so the influence of gas expansion on the steady base flow upstream of the flame is assumed to be small [92]. In this formulation we have not accounted for the effect that the temperature change across the flame on the acoustic modeshapes and frequencies. This is a reasonable assumption because the flame occupies a small fraction of the cross-section of the duct ($\alpha \leq 0.2$), and the bypass air causes the temperature jump to be small.

The dimensional governing equations for the acoustic perturbations are the momentum and energy equations:

$$\tilde{\rho}_0 \frac{\partial \tilde{u}}{\partial \tilde{t}} + \frac{\partial \tilde{p}}{\partial \tilde{x}} = 0 \tag{2.1}$$

$$\frac{\partial \tilde{p}}{\partial \tilde{t}} + \gamma \tilde{p}_0 \frac{\partial \tilde{u}}{\partial \tilde{x}} + \zeta \frac{\tilde{c}_0}{L_0} \tilde{p} - (\gamma - 1) \tilde{\dot{Q}} \delta(\tilde{x} - \tilde{x}_f) = 0 \tag{2.2}$$

where the rate of heat transfer from the flame to the gas is given by $\tilde{\dot{Q}}$, which is applied at the flame's position by multiplying $\tilde{\dot{Q}}$ by the dimensional Dirac delta distribution $\tilde{\delta}(\tilde{x} - \tilde{x}_f)$. The acoustic damping is represented by ζ and the model for this is described later.

The above equations may be non-dimensionalised using $\tilde{u}_0$, $\tilde{p}_0 \gamma M$, L_0 and $L_0/\tilde{c}_0$ for speed, pressure, length and time respectively. The dimensionless governing equations are:

$$\frac{\partial u}{\partial t} + \frac{\partial p}{\partial x} = 0 \tag{2.3}$$

$$\frac{\partial p}{\partial t} + \frac{\partial u}{\partial x} + \zeta p - \beta \dot{Q} \delta_D (x - x_f) = 0 \tag{2.4}$$

$$\beta \equiv \frac{(\gamma - 1) \tilde{\dot{Q}}_0 \alpha}{\gamma \tilde{p}_0 \tilde{u}_0}, \dot{Q} \equiv \frac{\tilde{\dot{Q}}}{\tilde{\dot{Q}}_0} \tag{2.5}$$

where $\beta \dot{Q}$ is the nondimensional heat release rate perturbation, which encapsulates all relevant information about the flame, base velocity and ambient conditions. The heat release rate is averaged over the cross-sectional area of the duct and the ratio of the area of base of the flame to the cross-sectional area of the duct, α, is small.

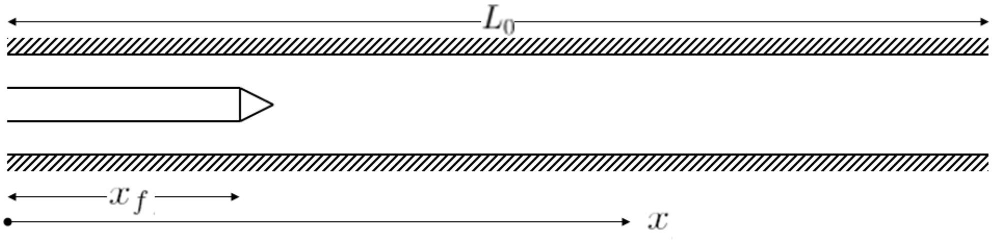

Figure 2.1: Schematic of the two-dimensional slot stabilized premixed flame in a duct. L_0 is the length of the duct, $\tilde{x}_f$ is the flame position along the duct, and the flow is from left to right.

For the open duct examined here, the pressure perturbations and gradient of velocity perturbations are both set to zero at the ends of the tube.

$$[p]_{x=0} = [p]_{x=1} = 0; \quad \left[\frac{\partial u}{\partial x}\right]_{x=0} = \left[\frac{\partial u}{\partial x}\right]_{x=1} = 0. \tag{2.6}$$

These boundary conditions are enforced by choosing basis sets that match these boundary conditions and satisfy the dimensionless momentum equation (2.3):

$$u(x,t) = \sum_{j=1}^{N} \eta_j(t) cos(j\pi x); \quad p(x,t) = -\sum_{j=1}^{N} \frac{\dot{\eta}_j(t)}{j\pi} sin(j\pi x). \tag{2.7}$$

In this Galerkin discretization, all the basis vectors are orthogonal. The state of the system is given by the amplitudes of the Galerkin modes that represent velocity, η_j, and those that represent pressure, $\dot{\eta}_j$. The energy equation is discretized by substituting (2.7) into the dimensionless energy equation (2.4). The acoustic damping, ζ, is dealt with by assigning damping parameters, ζ_j, to each mode, where $\zeta_j = c_1 j^2 + c_2 j^{1/2}$, where c_1 represents acoustic energy losses due to radiation from the open ends and c_2 represents dissipation in the acoustic viscous and thermal boundary layers at the duct walls.

$$c_1 = \frac{R^2\omega_1^2}{\tilde{c}_0^2}; \quad c_2 = \frac{\sqrt{2\omega_1}L_0}{\tilde{R}\tilde{c}_0}\left(\sqrt{\tilde{\nu}} + \sqrt{\tilde{\chi}}(\gamma - 1)\right). \tag{2.8}$$

This model is based on correlations developed by Matveev [42] from models in Landau & Lifshitz [93] and has been used in similar thermoacoustic systems [49; 50; 94]. Typical values for laboratory-scale Rijke tubes are $c_1 \approx 0.01 - 0.13$ and $c_2 \approx 0.005 - 0.03$. In particular, for a Rijke tube of length 70 cm and diameter 10 cm with an average duct temperature of 350K, $c_1 = 0.05$, $c_2 = 0.015$. Higher values of ζ correspond to shorter, wider tubes and lower values of ζ correspond to longer, thinner tubes.

In the Galerkin method, the dimensionless energy equation is then multiplied by $\sin(k\pi x)$ and integrated over the domain $x = [0, 1]$, thus reducing it to an ODE for each mode, j:

$$\frac{d}{dt}(\frac{\dot{\eta}_j}{j\pi}) + j\pi\eta_j + \zeta_j(\frac{\dot{\eta}_j}{j\pi}) + 2\beta sin(j\pi x_f) = 0, \tag{2.9}$$

which are integrated by direct time-marching from $t = 0$ using a 4th order Runge-Kutta algorithm.

2.2 Model for the premixed flame

The flame is described by a kinematic model based on the level set method proposed by Williams [68], which is also known as the G-equation model. In this approach the flame surface is modelled as a zero-contour of a continuous function G. The flame propagates normal to itself, while also being advected by the surrounding flow. In this model, the velocity field influences the heat release rate by distorting the flame's surface. This is often used in models of thermoacoustic systems, either directly [31; 95; 96; 97] or in the form a kinematic flame-tracking equation derived from the G-equation model [27; 30; 73; 76; 94; 98; 99]. Although this model is less complex than real premixed flames, it has been shown that it captures the major nonlinearities in premixed flame dynamics [73; 100].

The principal assumptions of the model are that (i) the flame is a thin surface separating unburnt reactants from burnt products; (ii) the influence of gas expansion across the flame front is negligible [32]. Assumption (i) allows for the flame to be tracked using the G-equation, which for the present two-dimensional case can be written as [68]:

$$\frac{\partial G}{\partial \tilde{t}} + \tilde{U}\frac{\partial G}{\partial \tilde{x}} + \tilde{V}\frac{\partial G}{\partial \tilde{y}} = s_L\sqrt{\left(\frac{\partial G}{\partial \tilde{x}}\right)^2 + \left(\frac{\partial G}{\partial \tilde{y}}\right)^2} \tag{2.10}$$

where tildes denote dimensional values and $G(x,y,t)$ is a time-varying function that takes negative values at points in the unburnt gas, positive values at points in the burnt gas and zero at points that lie on the flame surface. $\tilde{U}$ and $\tilde{V}$ are the instantaneous total velocities along the x and y directions. The flame speed, s_L, is a function of the equivalence ratio, but we only consider the dynamics of velocity perturbations imposed on fully premixed flames ignoring flame-stretch and curvature effects. Hence the equivalence ratio and flame speed are assumed to be uniform throughout the flow. Assumption (ii) allows for the velocity field to be independently specified, neglecting the coupling between the flow-field and flame surface evolution, and is the major simplifying assumption of this reduced order modelling approach. Equation (2.10) can be rewritten in terms of non-dimensional parameters: $x^* = \tilde{x}/L_f, y^* = \tilde{y}/R, u^* = \tilde{U}/\tilde{u}_0, v^* = \tilde{V}/\tilde{u}_0$, and $t^* = \tilde{t}\tilde{u}_0/L_f$ as,

$$\frac{\partial G}{\partial t^*} + u^*\frac{\partial G}{\partial x^*} + \beta_f v^*\frac{\partial G}{\partial y^*} = \left(\frac{s_L}{\tilde{u}_0}\right)\sqrt{\left(\frac{\partial G}{\partial x^*}\right)^2 + \beta_f^2\left(\frac{\partial G}{\partial y^*}\right)^2} \tag{2.11}$$

where, L_f is the nominal flame height, i.e. the height of the steady flame ignoring stretch effects, R is half-width of the burner and β_f is the flame aspect ratio, L_f/R. In this thesis the mean axial flow velocity, u_0, is uniform and there is no mean transverse velocity. The types of perturbation velocity models used and the resulting variations of equation (2.11) are described in subsequent chapters.

We have chosen to anchor the base of the flame to the burner lip, which simulates the case with a hot burner lip. Recent experiments on a self-excited ducted premixed flame show that flame lift-off occurs at large velocity fluctuation amplitudes and can lead to elaborate nonlinear behaviour such as intermittency, ultimately leading to flame blow-out [65]. This cannot be captured in our model. Flash back, however, is allowed, using the boundary condition proposed by Dowling [73] and implemented in the level set solver by Waugh [60].

We have neglected the influence of curvature on the flame speed in this thesis, but this has been included in a continuation analysis of a similar thermoacoustic system by Waugh [60]. Neglecting the influence of curvature on the flame speed leads to sharp cusps on the flame surface, which is unrealistic. This, however, allows faster computations because curvature is a second order quantity that requires a much smaller timestep for numerical stability.

Equation (2.11) is solved numerically using a 5th order Weighted Essentially Non-Oscillatory (WENO) scheme [101] and a 3rd order Total Variation Diminishing (TVD) Runge-Kutta scheme [102] for time integration. The non-dimensionalized spatial and temporal resolution in all the simulations are 5×10^{-3} and 5×10^{-4} respectively, with a uniform mesh spacing in both spatial directions. The local level set method is used to achieve a significant reduction in computational cost [103]. The boundary condition on the centerline (y=0) is symmetry, so we solve the G-equation only for one half of the flame. The boundary conditions on the other boundaries of the domain (top, bottom and right) are not needed because we use a local level-set method and the flame never reaches these boundaries for the range of conditions examined in this paper. The flame base is assumed to be anchored at a fixed location by specifying zero velocity in this region (hence the G-field does not advect here). These computations are performed within the framework of LSGEN2D, a general level set method solver, developed by Santosh Hemchandra [26; 32] with extensions and modifications by Waugh [60].

For a premixed flame, the heat release rate can be written as an integral of local heat release rate contributions over the flame surface, which can be expressed in terms of G as an integral over the whole domain,

$$q(t) = \int_D \rho s_L(\phi) h_R(\phi) \left|\nabla G\right| \delta(G) dx^* dy^* \tag{2.12}$$

where, $\delta(G)$ is the Dirac-delta function and $h_R(\phi)$ is the heat of reaction. The above integral, equation (2.12), is evaluated numerically using the formulation by

Smereka [104]. Note that, for fully premixed flames with constant flame speed, heat release rate oscillations are only due to flame surface area fluctuations induced by velocity perturbations that distort the flame surface. The simple velocity model and boundary conditions used in this thesis results in an unsteady heat release rate whose mean is less than the steady heat release rate of the unperturbed flame, which is unphysical. This is a well-known feature of the G-equation approach [105]. The thermoacoustic oscillations, however, are not affected by the mean of the heat release rate but only by its rate of change. So this simple model is retained.

Chapter 3

Nonlinear phenomena in thermoacoustic systems with premixed flames

Summary

Nonlinear analysis of thermoacoustic instability is essential for prediction of frequencies, amplitudes and stability of limit cycles. Limit cycles in thermoacoustic systems are reached when the energy input from driving processes and energy losses from damping processes balance each other over a cycle of the oscillation.

In this chapter an integral relation for the rate of change of energy of a thermoacoustic system is derived. This relation is analogous to the well-known Rayleigh criterion in thermoacoustics, but can be used to calculate the amplitudes of limit cycles, as well as their stability. The relation is applied to a thermoacoustic system of a ducted slot-stabilized 2-D premixed flame. Using open-loop forced simulations, the flame describing function (FDF) is calculated. The gain and phase information from the FDF is used with the integral relation to construct a cyclic integral rate of change of energy (CIRCE) diagram that indicates the amplitude and stability of limit cycles. This diagram is also used to identify the types of bifurcation the system exhibits and to find the minimum amplitude of excitation needed to reach a stable limit cycle from another linearly stable state,

for single-mode thermoacoustic systems. Furthermore, this diagram shows precisely how the choice of velocity model and the amplitude-dependence of the gain and the phase of the FDF influence the nonlinear dynamics of the system.

Time domain simulations of the coupled thermoacoustic system are using a single mode, as well as twenty modes, are compared against predictions from the CIRCE diagram. For the single mode system, the time domain calculations agree well with the frequency domain predictions. The heat release rate is highly nonlinear but, because there is only a single acoustic mode, this does not affect the limit cycle amplitude. For the twenty-mode system, however, the higher harmonics of the heat release rate and acoustic velocity interact resulting in a larger limit cycle amplitude. Multi-mode simulations show that in some situations the contribution from higher harmonics to the nonlinear dynamics can be significant and must be considered for an accurate and comprehensive analysis of thermoacoustic systems.

Nomenclature

f	Forcing frequency
f^*	Non-dimensional natural frequency of the self-excited system, $(c_0 L_f / 2\tilde{u}_0 L_0)$
St	Strouhal number, $f L_f / \tilde{u}_0$
K	Ratio of mean velocity to disturbance convection speed, $\tilde{u}_0 / \tilde{u}_c$
E	Acoustic energy density
ϵ	Nondimensional velocity perturbation amplitude
ϕ	Equivalence ratio
ω	Angular frequency
φ	Phase

3.1 Introduction

Linear stability analysis of thermoacoustic systems can be used to predict frequencies and growth rates of linearly unstable modes. However, they can neither predict limit cycle amplitudes, nor a system's susceptibility to oscillations triggered by finite amplitude excitations.

Nonlinear analyses of thermoacoustic systems in the frequency domain based on the Flame Describing Function (FDF) was described in §1.3. While this approach has been successful in some practical systems as shown by Noiray *et al.* [55], Subramanian *et al.* [49] argue that the system behaviour predicted using the FDF approach may be quantitatively as well as qualitatively different from that seen using time domain simulations of simple thermoacoustic models. They point out that using a two-part approach and a modal analysis fail to capture the intricate coupling between combustion and acoustics.

The aims of this chapter are (i) to examine nonlinear thermoacoustic phenomena of a ducted premixed flame; (ii) to evaluate the accuracy of limit cycle amplitudes calculated from the frequency domain against calculations from the time domain. An energy integral relation that assumes the existence of limit cycles is derived for a single mode thermoacoustic system. This integral relation is used with the FDF (i) to calculate the amplitudes and stability of limit cycles; (ii) to predict the types of bifurcation in such systems; (iii) to estimate the minimum amplitude required to trigger a single-mode system into stable limit cycle oscillations.

The rest of this chapter is organised as follows. §3.2 describe the details of the model specific to this chapter. In §3.3, criteria for the amplitude and stability of limit cycles are derived. §3.4 describes the linear and nonlinear velocity-coupled heat release response of the flame and the influence of the choice of velocity model on these. In §3.5, diagrams that map the stability of thermoacoustic systems and the nonlinear phenomena observed in these are discussed. §3.6 shows simulations in the time domain and a comparison between frequency and time domain calculations. Closing remarks with an outlook on future work are presented in §3.7.

3.2 Models

In chapter-2, equation (2.11), a perturbation velocity model is required to solve the G-equation. Early studies have used a uniform axial velocity perturbation [98; 106]. However, it was shown by Baillot *et al.* [107; 108] that the shear layer rolls up into vortices that advect downstream, distorting the flame surface. This was modelled as a convective wave that propagates through the velocity field of a vibrating flame by Schuller *et al.* [30] to calculate the Flame Transfer Function (FTF). This model predicted the gain and phase of the FTF over a range of Strouhal numbers with reasonable accuracy. Within the flame domain, if the divergence free assumption is used for the hydrodynamics, the continuity equation can be solved to find the transverse velocity perturbation field, given an axial velocity perturbation field. This was done by Preetham *et al.* [31] and more recently by Cuquel *et al.* [109], who have also derived analytical flame transfer functions with both axial and transverse velocity perturbations. However, Preetham *et al.* [31] show that the differences between transfer functions calculated using a purely axial velocity perturbation field and one with both axial and transverse perturbations are small. Hence, for the sake of simplicity, a purely axial convective wave velocity perturbation model is adopted in this chapter. This assumption will be re-visited in chapter-4.

The non-dimensionalised velocity field is specified as a harmonically oscillating travelling wave as,

$$u^* = 1 + \epsilon \cos(2\pi \mathrm{St}(Kx^* - t^*)); \quad v^* = 0, \tag{3.1}$$

where, $\epsilon = \tilde{u}/\tilde{u}_0$ is the non-dimensional velocity perturbation, $\mathrm{St} = fL_f/\tilde{u}_0$ is the excitation Strouhal number and $K = \tilde{u}_0/\tilde{u}_c$ is the ratio of mean velocity to disturbance convection speed (phase speed of velocity disturbances). Typically K is assumed to be equal to 1, i.e. the phase speed is assumed to equal the mean flow velocity. As seen in experiments [107; 110], however, the phase speed of velocity disturbances depends on a variety of factors such as the forcing frequency, amplitude, shear layer characteristics, temperature and density changes across the flame surface, burner geometry etc. In order to capture the dependence of the phase speed on the above-mentioned parameters, K is retained as a parameter in the model and the implications of the value of K on the nonlinear behaviour of the system is described in §3.5.

The nonlinearity in heat release fluctuations is more pronounced in short flames compared to long flames [100]. For a given mean velocity, the shortest flame is that which has the greatest flame speed. In order to allow for a greater degree of nonlinearity, ϕ is chosen such that s_L is maximized. For the ϕ-dependence used in this chapter [111], $\phi = 1.06$ maximizes s_L to $0.42m/s$ and this flame speed is used throughout this chapter. Note that thermoacoustic systems with lean flames (lower flame equivalence ratios) exhibit similar qualitative behaviour and will be described in chapter-4.

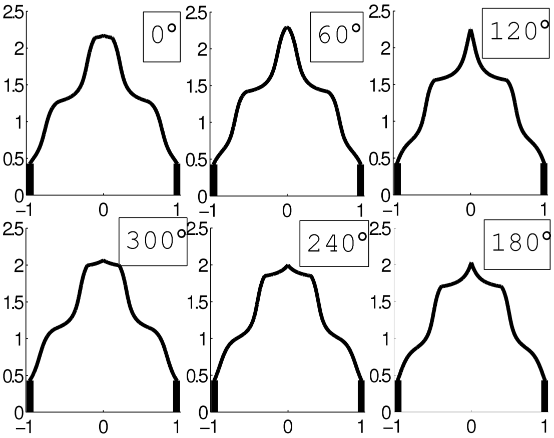

Figure 3.1: Instantaneous images of the flame during one forcing cycle, $\phi = 1.06$, $\beta_f = 2.14$, $\epsilon = 0.25$, St = 1, $K = 2.5$. The thick black line represents the slot burner and the thin black curve is the flame surface. Note the formation of sharp cusps towards the products, a distinct characteristic of premixed flames seen in experiments [29; 98; 107].

Fig. 3.1 shows instantaneous flame images over one forcing cycle. Note the formation of sharp cusps towards the products, a distinct characteristic of premixed flames seen in experiments [29; 98; 107].

3.3 Integral Criteria for Limit Cycles: Amplitudes and Stability

The Rayleigh criterion is a well-known and widely used criterion in thermoacoustics to determine whether acoustic disturbances in a system grow in magnitude [112; 113; 114]. In the generalized form, as stated by Dowling and Morgans [1], an acoustic mode grows in amplitude if the energy gain from combustion exceeds the energy losses from the boundaries averaged over a period of the acoustic oscillation. As noted by Rayleigh, the phase difference between pressure and heat release rate is crucial in determining the acoustic energy change over a cycle [3]. The Rayleigh criterion, however, does not provide the amplitude of limit cycle oscillations.

The purpose of this section is to propose a method to determine the amplitude of periodic oscillations in simple thermoacoustic systems and to identify their stability. The method used here is similar to the method of averaging used by Culick [20]. Culick derived coupled nonlinear first order differential equations for the amplitudes and phases of the acoustic modes which are then solved numerically. In order to simplify the analysis, we consider only the fundamental acoustic mode. This simplification is reasonable when either the higher acoustic modes are strongly damped, or when the flame response at the higher harmonics is small. While the single-mode assumption precludes interactions between modes, it allows one to derive analytical results that provide insight into the nonlinear dynamics of simple thermoacoustic systems.

The acoustic velocity perturbation is written as

$$\tilde{u} = \epsilon \tilde{u}_0 \cos(\omega \tilde{t} + \varphi) \cos\left(\frac{\pi \tilde{x}}{L_0}\right). \tag{3.2}$$

Solving for acoustic pressure perturbation using the dimensional momentum equation, (2.1), with the appropriate boundary conditions, (2.6), yields

$$\tilde{p} = \epsilon \tilde{u}_0 \tilde{\rho}_0 \frac{\omega L_0}{\pi} \sin(\omega \tilde{t} + \varphi) \sin\left(\frac{\pi \tilde{x}}{L_0}\right). \tag{3.3}$$

The acoustic energy is written as the sum of potential and kinetic energies as,

$$\tilde{E} \equiv \frac{1}{2}\left(\frac{\tilde{p}^2}{\tilde{\rho}_0\tilde{c}_0^2} + \tilde{\rho}_0\tilde{u}^2\right). \tag{3.4}$$

For a thermoacoustic system on a limit cycle, the change in the total acoustic energy in the domain over a cycle of oscillation is zero,

$$\int_{t'}^{t'+T}\int_D \frac{\partial\tilde{E}}{\partial\tilde{t}}\mathrm{d}\tilde{x}\mathrm{d}\tilde{t} = \int_{t'}^{t'+T}\int_D \left(\frac{\tilde{p}}{\tilde{\rho}_0\tilde{c}_0^2}\frac{\partial\tilde{p}}{\partial\tilde{t}} + \tilde{\rho}_0\tilde{u}\frac{\partial\tilde{u}}{\partial\tilde{t}}\right)\mathrm{d}\tilde{x}\mathrm{d}\tilde{t} = 0. \tag{3.5}$$

Using the dimensional energy equation, (2.2), for $\partial\tilde{p}/\partial t$, this reduces to

$$\int_{t'}^{t'+T}\int_D \left(\frac{(\gamma-1)\tilde{p}\tilde{\dot{Q}}\tilde{\delta}(\tilde{x}-\tilde{x}_f)}{\tilde{\rho}_0\tilde{c}_0^2} - \frac{\zeta\tilde{p}^2}{\tilde{\rho}_0\tilde{c}_0 L_0}\right)\mathrm{d}\tilde{x}\mathrm{d}\tilde{t} = 0. \tag{3.6}$$

Using equations (3.2) and (3.3) and integrating over the domain $\tilde{x} = [0, L_0]$, recollecting that $\tilde{x}_f$ is the flame position, yields

$$\int_{t'}^{t'+T}\left(2\beta\dot{Q}\sin(\omega\tilde{t}+\varphi)\sin\left(\frac{\pi\tilde{x}_f}{L_0}\right) - \frac{\omega L_0}{\pi\tilde{c}_0}\zeta\epsilon\sin^2(\omega\tilde{t}+\varphi)\right)\mathrm{d}\tilde{t} = 0. \tag{3.7}$$

In general, the heat release rate perturbation is a nonlinear function of $\tilde{u}$ and contains higher harmonics of the fundamental frequency, ω. It can be written as a Fourier series,

$$\dot{Q} = \sum_{k=1}^{\infty} q_k\cos(k\omega\tilde{t}+\varphi_k). \tag{3.8}$$

If the phase difference between the terms in the expansion of $\dot{Q}$ and the acoustic velocity perturbation are written as $\triangle\varphi_k \equiv k\varphi - \varphi_k$, and the orthogonality of the Fourier series is used, the cyclic integral equation (3.7) reduces to

$$\int_{t'}^{t'+T}(\Psi_{driv} - \Psi_{damp})\sin^2(\omega\tilde{t}+\varphi)\mathrm{d}\tilde{t} = 0, \tag{3.9}$$

$$\Psi_{driv} \equiv 2\beta\sin\left(\frac{\pi\tilde{x}_f}{L_0}\right)q_1\sin(\triangle\varphi_1), \quad \Psi_{damp} \equiv \frac{\omega L_0}{\pi\tilde{c}_0}\zeta\epsilon. \tag{3.10}$$

In the above equation, (3.9), the driving and damping terms, Ψ_{driv} and Ψ_{damp}, are constant on a limit cycle. Hence, for equation (3.9) to be true, the driving and damping terms must be equal, i.e. $\Psi_{driv} = \Psi_{damp}$, or,

$$2\beta \sin\left(\frac{\pi \tilde{x}_f}{L_0}\right) q_1 \sin(\triangle\varphi_1) = \frac{\omega L_0}{\pi \tilde{c}_0}\zeta\epsilon_s. \tag{3.11}$$

Equation (3.11) describes the balance between driving (LHS) and damping (RHS) processes on a limit cycle. Note that the gain of the velocity-coupled FDF, q_1/ϵ, and the phase of the velocity-coupled FDF, $\triangle\varphi_1$, are explicitly related to the damping factor, ζ, on a limit cycle. With measured or computed FDFs, the above equation can be used to find the amplitude of acoustic velocity perturbations, ϵ_s, on limit cycles. This equation also shows that for a single-mode system, over one cycle of the oscillation, only the fundamental of the heat release rate contributes to the limit cycle amplitude.

The stability of limit cycles is obtained by calculating the gradient of the LHS of (3.9) with respect to ϵ, i.e.

$$\left[\frac{\partial}{\partial\epsilon}\int_{t'}^{t'+T} (\Psi_{driv} - \Psi_{damp})\sin^2(\omega\tilde{t} + \varphi)\mathrm{d}\tilde{t}\right]_{\epsilon_s} < 0 \tag{3.12}$$

implies that the limit cycle is stable.

3.4 Linear and Nonlinear Flame Response

The linear and nonlinear velocity-coupled response of premixed flames has been studied extensively [29; 30; 31; 55; 100; 115]. The configuration investigated here, however, is a 2-D slot-stabilized flame, which has different response characteristics. Hence the FDF in this chapter was calculated by harmonically forcing the kinematic model of the premixed flame (using the G-equation) and extracting the heat release rate at the forcing frequency, discarding higher harmonics. The forcing frequency, St, was varied from 0.04 to 4 in steps of 0.02. The forcing amplitude, ϵ, was varied from 0.02 to 0.4 in steps of 0.02. The amplitude of the streamwise velocity perturbation, ϵ, was used to define the FDF. It is useful to highlight the main features of its FDF. Fig. 3.2 shows the gain and phase of the FDF of the heat release rate response to velocity perturbations. As noted by several researchers in the past, the gain at low frequencies tends to unity, the phase lag at low frequencies is zero and the low frequency behaviour is largely linear [116]. The phase lag increases with St, which is characteristic of systems with a time-delay.

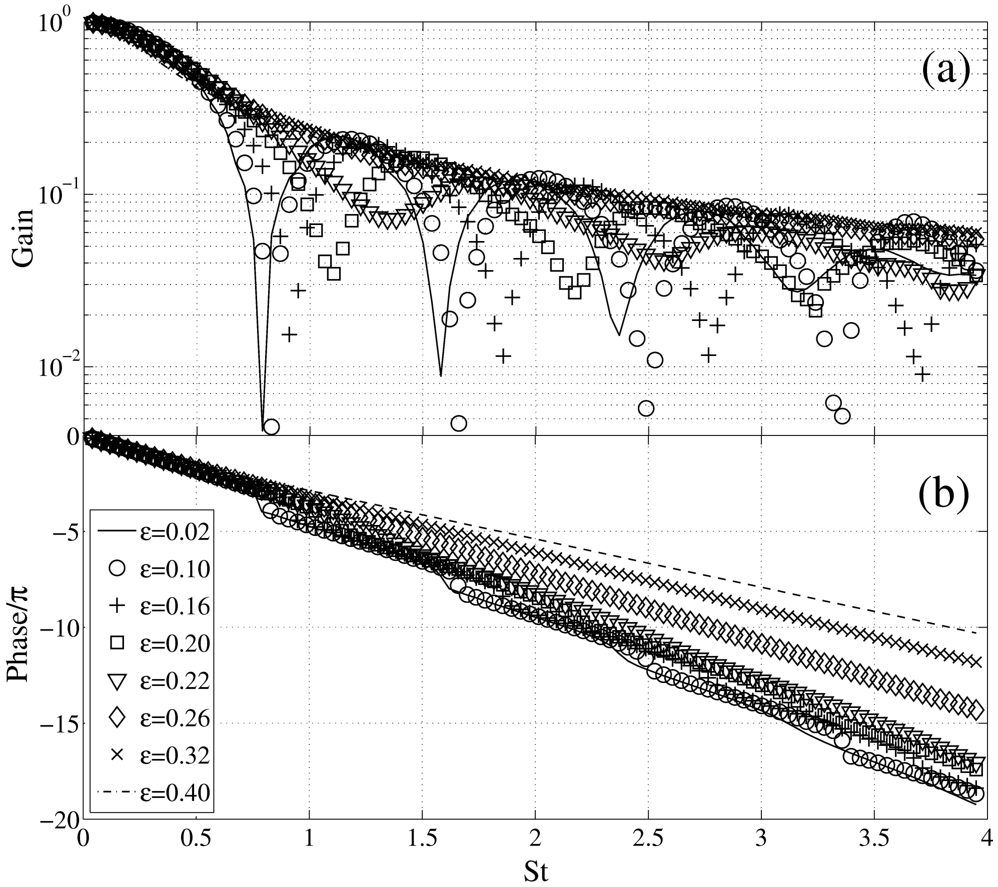

Figure 3.2: Flame Describing Function, $\left(FDF(\omega,\epsilon) = \dot{\tilde{Q}}'/\dot{\tilde{Q}}_0/\tilde{u}'/\tilde{u}_0\right)$: a) Gain and b) Phase, $K = 2.5$, $\beta_f = 2.14$, $\phi = 1.06$.

The FDF has zeros due to the destructive interference between disturbances created on the flame surface from flow non-uniformity and the flame anchoring boundary condition [31]. When these zeros are located close to the imaginary axis in the complex plane, they result in a sharp decrease in the gain and a phase jump of π across the St at which they are located, for example, at St $= 0.8, 1.6, 2.4, ...$ However, as the forcing amplitude increases, all zeros move to higher St. This suggests that the time-delay between the heat release rate and velocity perturbations decreases, which is due to the decrease in the mean flame height as amplitude increases. Secondly, as the forcing amplitude increases, the zeros move further away from the imaginary axis in the complex plane. Hence the decrease in gain is less dramatic in the vicinity of the zeros and the phase decrease of π is spread over a wider range of St. At large forcing amplitudes, the zeros are very far away from the imaginary axis. Hence the gain and phase are smooth and decrease monotonically with frequency.

The amplitude-dependent behaviour of the zeros results in significant gain and phase variation of the FDF. Crucially, at a given St, the amplitude dependence of the gain is not monotonic and saturation does not always occur. Indeed, at some frequencies, the gain increases as forcing amplitude increases. Preetham *et al.* proposed that the amplitude dependence of the gain determines whether a system exhibits subcritical bifurcations [31]. This rests on the assumption, however, that the FDF phase remains constant at all amplitudes, which is not the case for the flame investigated here. At a given St, the phase difference decreases as the amplitude increases and the decrease is most dramatic when a zero crosses that particular St. §3.5 shows how the combined effect of the amplitude-dependence of the gain and phase impacts the nonlinear dynamics of these systems.

Finally, it is important to note that when K, the ratio of the mean velocity, $\tilde{u}_0$, to the disturbance phase speed, $\tilde{u}_c$, is assumed to be zero (i.e. a uniform disturbance) or one (i.e. the disturbance phase speed equals the mean flow velocity), the FDF does not exhibit the features discussed above. The nonlinearities of the flame response for these special cases result in a monotonic decrease in the gain and negligible change in the phase, as amplitude increases [31; 100]. The effect of K on the nonlinear dynamics of this system will be highlighted in §3.5.

3.5 Cyclic Integral of Rate of Change of Energy (CIRCE) Diagrams

Using the integral criterion derived in §3.3, a stability diagram of single-mode thermoacoustic systems can be constructed, as shown in Fig. 3.3. This is a diagram of the cyclic integral of rate of change of energy (CIRCE) as a function of non-dimensional velocity perturbation amplitude (vertical axis), across different single-mode systems of varying non-dimensional resonant frequencies (horizontal axis). Note that each non-dimensional frequency corresponds to a thermoacoustic system with a different duct length. Hence, for a given system, the diagram is to be interpreted by moving along the amplitude axis (vertical axis) at the frequency that corresponds to the fundamental mode of that system. Each frame of Fig. 3.3 corresponds to a different value of K, the ratio of the mean velocity to the disturbance phase speed.

The grey-scale is such that regions where driving exceeds damping are light, while regions where damping exceeds driving are dark. The boundaries between light and dark regions, marked by the black curves, are locations where driving and damping are exactly equal, and hence they correspond to the limit cycles of the system. The vertical dashed lines in each frame represent the scenarios examined later, in terms of the number of limit cycles that exist and their stability. Furthermore, the criterion in equation (3.12) is used to infer the stability of these limit cycles.

Before investigating the different scenarios in detail, it is useful to note that the differences between Figs. 3.3 (a), (b) and (c) illustrate the strong influence of K, the ratio of the mean velocity to the disturbance phase speed, on the nonlinear behaviour of the system. The shapes of the limit cycle contours and the number of limit cycles that exist for a particular system (i.e. for a particular non-dimensional frequency) are direct manifestations of the gain and phase variation of the corresponding FDFs. The amplitude-dependence of the phase of the FDF for the $K = 1$ case is negligible, whereas the gain saturates at high amplitudes. Hence only a single intersection of the driving and damping curves is possible for linearly unstable systems and at most one limit cycle exists at a given frequency, as seen in Fig. 3.3(a). For the $K = 2.5$ case however, the gain is not monotonic

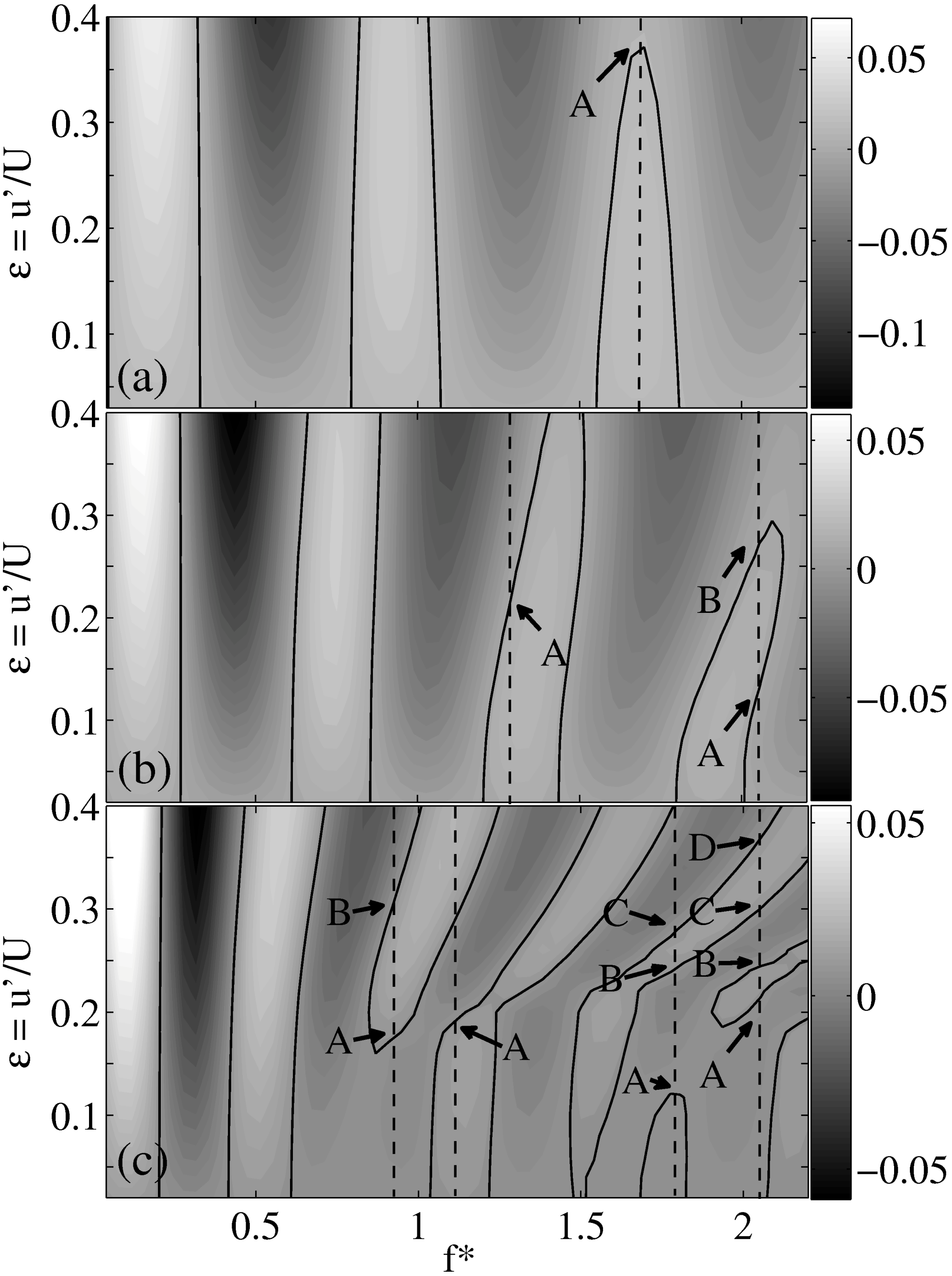

Figure 3.3: CIRCE Diagram: driving (Ψ_{driv}) – damping (Ψ_{damp}) as a function of amplitude, ϵ, for thermoacoustic systems with different natural frequencies, f^*. a) $K = 1.0$, b) $K = 1.5$, c) $K = 2.5$

and the phase changes by several multiples of π, as amplitude increases. Hence, as the amplitude increases, the driving curve has several sign changes and multiple intersections with the damping line are possible, resulting in several limit cycles, as seen in Fig. 3.3(c). The gain and phase of the FDF of the $K = 1.5$ case show weaker amplitude-dependence compared to the $K = 2.5$ case, hence it has fewer limit cycles at a given system frequency. As discussed in §3.4, the gain and phase variation is due to the behaviour of the zeros of the FDF, and their influence is seen clearly in these CIRCE diagrams.

Figures 3.4 and 3.5 are slices of the CIRCE diagram that depict the four different scenarios marked by the dashed lines in Fig. 3.3(c). In these figures, the solid line represents the driving term, Ψ_{driv}, while the dashed line represents the damping term, Ψ_{damp}. The complicated amplitude-dependence of Ψ_{driv} is due to the amplitude-dependence of the gain and phase of the FDF, and will be discussed in detail later.

Fig. 3.4(a) shows a system that is linearly unstable about the fixed point because driving exceeds damping at small amplitudes. At point-A, where the driving and damping balance each other, a limit cycle is established. Furthermore, the gradient of the CIRCE (see equation (3.12)) at point-A is negative, therefore this limit cycle is stable. This situation corresponds to a mono-stable state. In terms of a control parameter such as βq_1, this corresponds to a supercritical bifurcation.

On the other hand, Fig. 3.4(b) shows a system that is linearly stable about the fixed point. Indeed, the so-called driving term is negative in the linear limit due to the sign of the phase difference, i.e. $\sin(\triangle\varphi_1) < 0$ for small ϵ. However, as amplitude increases, changes in the driving term result in two intersections with the damping line at points A and B, which are an unstable and a stable limit cycle respectively. If the system in its linearly stable state is given an excitation with amplitude greater than the amplitude of state-A, oscillations in the system will grow until the system reaches state-B. This phenomenon is called triggering. In a single-mode thermoacoustic system, the minimum amplitude of an excitation that can cause triggering is the amplitude at point-A. For this minimum amplitude excitation to be successful in triggering the system, however, the excitation has to be given in the right direction. For example, in the case of velocity-coupled

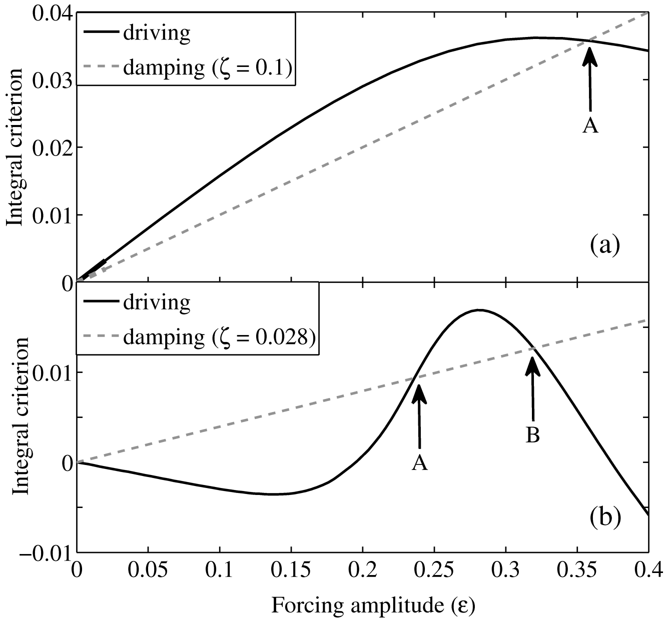

Figure 3.4: CIRCE for thermoacoustic systems with different fundamental frequencies (duct lengths), $K = 2.5$, $\phi = 1.06$, $\beta_f = 2.14$ a) Slice of Fig. 3.3(c) at $f^* = 0.4$, A - stable limit cycle, and b) Slice of Fig. 3.3(c) at $f^* = 1.0$, A - unstable limit cycle, B - stable limit cycle

oscillations of a premixed flame, the velocity excitation has to be given when the flame shape is most receptive to this excitation. In a system with several modes however, it has been shown that triggering can occur, due to non-normal transient growth, at amplitudes smaller than that of the unstable limit cycle [50]. The situation depicted in Fig. 3.4(b) corresponds to a bi-stable state. In terms of a control parameter such as βq_1, this corresponds to a subcritical bifurcation.

The systems shown in Figs. 3.5(a) and (b) have similar linear behaviour to those of Figs. 3.4(a) and (b), but have more complex nonlinear behaviour because the gain and phase, at high St, vary greatly as the amplitude increases. Using the same reasoning as before, Fig. 3.5(a) shows that the system has stable limit cycles at A and C and an unstable limit cycle at B. From the stable oscillating state at A, the system can be triggered into large amplitude oscillations with an excitation of amplitude greater than that of point-B. This situation corresponds to a bi-stable state. In terms of a control parameter such as βq_1, this corresponds

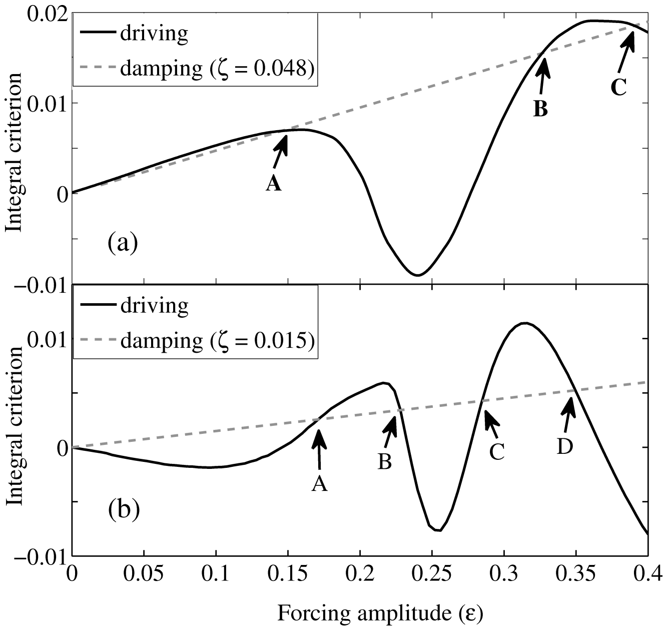

Figure 3.5: CIRCE for thermoacoustic systems with different fundamental frequencies (duct lengths), $K = 2.5$, $\phi = 1.06$, $\beta_f = 2.14$ a) Slice of Fig. 3.3(c) at $f^* = 1.2$, A and C - stable limit cycles, B - unstable limit cycle, and b) Slice of Fig. 3.3(c) at $f^* = 1.8$, A and C - unstable limit cycles, B and D - stable limit cycles.

to a supercritical bifurcation followed by two fold bifurcations. As mentioned in [38], a system must have either a subcritical bifurcation or a supercritical bifurcation followed by fold bifurcations in order to be susceptible to triggering.

Finally, Fig. 3.5(b) shows a system that is linearly stable, has two unstable limit cycles (A and C) and two stable limit cycles (B and D). An excitation with amplitude greater than that of A, but less than that of C, will eventually lead to stable oscillations at B. An excitation with amplitude greater than that of C, however, will lead to stable oscillations at D. As in Fig. 3.5(a), the system can be triggered from one stable limit cycle to another by a suitably large excitation. This situation corresponds to a tri-stable state. In terms of a control parameter such as βq_1, this corresponds to a subcritical bifurcation followed by three fold bifurcations.

This wide range of behaviour in figures 3.4 and 3.5 can be explained by

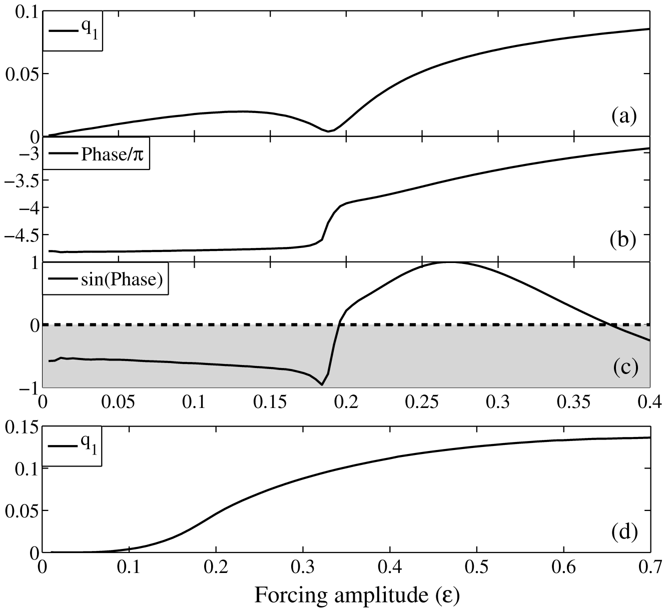

Figure 3.6: Amplitude-dependence of the fundamental of heat release rate oscillations and the phase between heat release rate and velocity perturbations, $K = 2.5$, $\phi = 1.06$, $\beta_f = 2.14$ (a) q_1 at St $= 1.0$, (b) $\Delta\varphi_1$ at St $= 1.0$, (c) $\sin(\Delta\varphi_1)$ at St $= 1.0$. The grey patch shows regions where driving is negative, while white shows where it is positive. (d) q_1 at St $= 0.8$

examining the amplitude-dependence of the gain and phase in Fig. 3.2. Firstly, the supercritical bifurcation seen in Fig. 3.4(a) at St $= 0.4$ is because the gain decreases as the forcing amplitude increases, while the phase remains fairly constant. This is the most commonly described route to a limit cycle in thermoacoustic systems. Secondly, the subcritical bifurcation seen in Fig. 3.4(b) at St $= 1.0$ is because the phase changes significantly as the amplitude increases. Fig. 3.6(a) shows the fundamental of heat release rate, q_1, (b) shows the phase difference between the fundamental of heat release rate and velocity, $\Delta\varphi_1$, and (c) shows $\sin(\Delta\varphi_1)$ at St $= 1.03$. Note that $\sin(\Delta\varphi_1)$ is negative at low amplitudes (patched grey) but changes sign at around $\epsilon = 0.2$. Since $\sin(\Delta\varphi_1)$ is a factor in the driving term, it is clear that the driving becomes positive at a finite amplitude, reaches a peak and then decreases at high amplitudes, as seen in Fig. 3.4(b). Depending on the value of the damping factor, ζ, an unstable and a stable limit cycle can exist between $\epsilon = 0.2$ and $\epsilon = 0.38$. A subcritical bifurcation is possible also when the amplitude-dependence of the gain is such that it increases as the forcing amplitude increases, followed by saturation at high amplitudes. This behaviour is most likely to be seen at a linear zero of the FDF, for example, at St = 0.8. Fig. 3.6(d) shows q_1 versus forcing amplitude at St = 0.8. For this frequency, the phase difference remains constant as amplitude increases. Hence this corresponds to a driving curve with an inflection point, which permits two limit cycles at finite amplitudes. The above two examples are special cases, where the amplitude-dependence of either the gain or the phase leads to a subcritical bifurcation. In most cases, however, it is the combined effect of the gain and the phase which results in the driving curve intersecting the damping line twice, which, for a linearly stable system, represents a subcritical bifurcation. Finally, at high frequencies, the changes in the gain are small, whereas changes in phase are large. Indeed, the dramatic changes seen in the driving term in Fig. 3.5(a) and (b) and the multiple intersections with the damping line are due to the large variation in phase, as amplitude increases, at high St.

3.6 Time Domain Simulations

The analyses in the previous sections were based on analytical results for a single-mode system with amplitude-dependent information derived from the FDF. It is useful to compare these results with time-domain calculations of self-excited oscillations to verify the accuracy of the frequency-domain predictions.

Fig. 3.7 shows time domain calculations of self-excited thermoacoustic systems with one Galerkin mode and twenty Galerkin modes. Both these systems have a non-dimensional fundamental frequency of $f^* = 0.87$, which for a duct of length, L_0, of 1.954m, and flame length, L_f, of 1×10^{-2}m, corresponds to a dimensional fundamental frequency of 87Hz. These systems are linearly unstable and have supercritical bifurcations. Fig. 3.7(a) shows that the two systems reach limit cycles of different amplitudes. Fig. 3.7(b) shows that the higher Galerkin modes contain approximately ten percent of the total energy of the system. The higher modes contribute to the increase in amplitude of limit cycle oscillations seen in Fig. 3.7(a).

Fig. 3.8(a) shows heat release rate oscillations, with one of the signals phase-

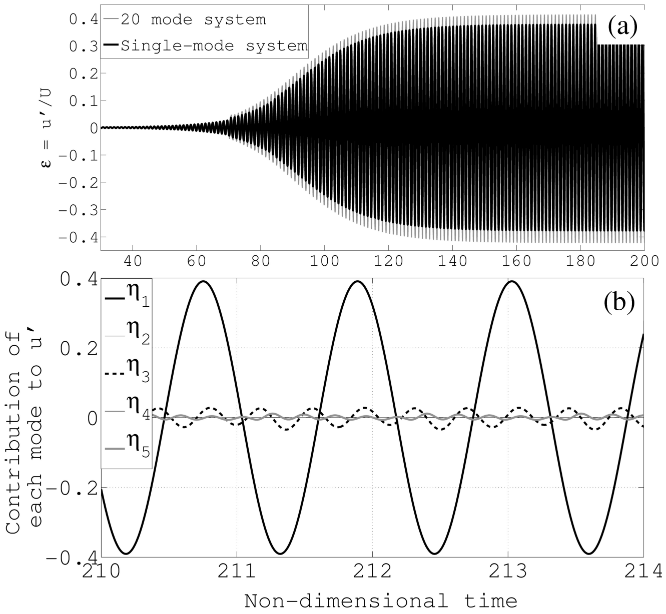

Figure 3.7: Time domain calculations for self-excited thermoacoustic systems with one mode and twenty modes, $f^* = 0.87$, $K = 1.5$, $\beta_f = 2.14, \phi = 1.06$, $\zeta = 0.05$ $(c_1 = 0.03, c_2 = 0.02)$ (a) Time trace of the acoustic velocity perturbations at the flame location, x_f (b) Time trace of the contributions of the first five Galerkin modes to the acoustic velocity at the flame location, x_f, of the 20-mode system.

shifted slightly in order to avoid overlap on the figure. The corresponding Fourier transforms are shown in Fig. 3.8(b). Note that the heat release rate signals are highly nonlinear, with the first harmonic having a magnitude more than forty percent that of the fundamental. In the single-mode system, however, the higher harmonics of the heat release rate cannot interact with the velocity perturbations, as shown in §3.3. On the other hand, in the twenty-mode system, the higher harmonics of the heat release rate contribute to the dynamics by interacting with the higher acoustic velocity modes. For this reason, the twenty-mode system extracts more energy from the flame and transfers it to the acoustics, than does the single-mode system. As a result, the single-mode system reaches a limit cycle with $\epsilon = 0.375$, while the twenty-mode system reaches a limit cycle with $\epsilon = 0.415$.

The amplitude of oscillation predicted by the CIRCE criterion with information from the FDF, shown in Fig. 3.9, is $\epsilon = 0.377$. Clearly, in spite of a fairly

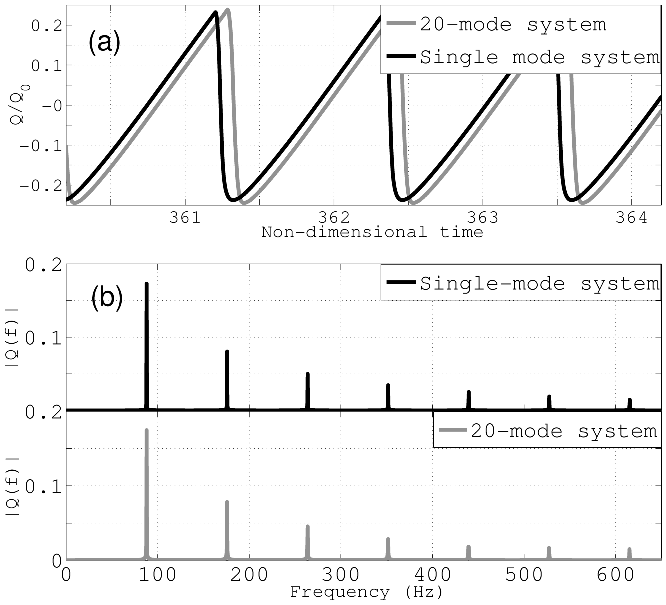

Figure 3.8: Nonlinear heat release rate oscillations in thermoacoustic systems with one mode and twenty modes, $f^* = 0.87$, $K = 1.5$, $\beta_f = 2.14, \phi = 1.06$, $\zeta = 0.05$ $(c_1 = 0.03, c_2 = 0.02)$ (a) Time trace of heat release rate (phase-shifted to avoid overlap of figures) and (b) Fourier transforms of heat release rate.

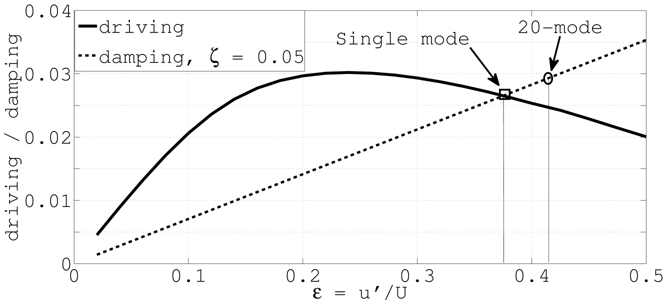

Figure 3.9: CIRCE diagram: Intersection of driving and damping curves represents the frequency domain prediction for limit cycle amplitude. Time-domain limit cycle locations are marked by symbols. $f^* = 0.87$, $K = 1.5$, $\beta_f = 2.14, \phi = 1.06$, $\zeta = 0.05$ $(c_1 = 0.03, c_2 = 0.02)$

high degree of nonlinearity in the heat release signal, very good agreement is obtained between the single-mode time domain and frequency domain results. An important point to note is that close agreement is to be expected when time-domain simulations of a single-mode system are compared against results from the criterion derived in §3.3, because only the fundamental modes of heat release rate and acoustic velocity can interact, as shown in §3.3. For the twenty-mode system, however, the effect of the higher modes on the system dynamics is not negligible and the twenty-mode system has a limit cycle amplitude that is larger than that of the single-mode system.

At the operating condition of the example discussed above, the difference in limit cycle amplitude between the single-mode and twenty-mode systems is about ten percent. There can, however, be operating conditions where large discrepancies exist between the single-mode and multi-mode systems. Such discrepancies would indicate that interactions between the higher modes play a crucial role in the system dynamics. A detailed analysis of this is beyond the scope of this chapter and will be the subject of future investigations.

3.7 Conclusions

This chapter examines nonlinear thermoacoustic phenomena of a simple premixed flame in a tube. The flame is modelled using a nonlinear kinematic model based on the G-equation, while the acoustics are governed by linearised momentum and energy equations. Assuming the existence of limit cycles, integral criteria are derived for a single mode thermoacoustic system to estimate the amplitudes of limit cycles and their stability. Using open-loop forced simulations, the sinusoidal flame describing function (FDF) is calculated. The FDF has zeros because of the interactions between the two types of flame front disturbances characteristic of anchored premixed flames with non-uniform velocity fields. The amplitude-dependence of the gain and phase of the FDF is shown to be related to the amplitude-dependence of the zeros of the FDF. The integral criteria are used with the amplitude-dependence of the gain and phase of the FDF to construct cyclic integral of rate of change of energy (CIRCE) diagrams that show precisely when a thermoacoustic system is mono-stable, bi-stable or tri-stable. These diagrams are also used to show the types of bifurcation seen in such systems and to find the minimum amplitude of excitation required to trigger a single-mode thermoacoustic system into limit cycle oscillations.

The choice of velocity model and the phase speed of convective disturbances are shown to be crucial for prediction of nonlinear dynamics of thermoacoustic systems. When K, the ratio of the mean velocity to the phase speed of convective disturbances, is assumed to be zero or one, which are the most commonly made assumptions, the system can have only one stable state. For other values of K, several limit cycles exist and the system has combinations of fold bifurcation and either supercritical or subcritical Hopf bifurcations, depending on the operating condition.

Previous studies have highlighted the influence of the amplitude dependence of the FDF gain [31] or phase [55] on nonlinear behaviour. In this chapter it is shown that there exist certain regions where either the gain or the phase is more influential, but the combined effect of the gain and phase has to be considered to accurately predict nonlinear behaviour.

Time domain simulations of the coupled thermoacoustic system are performed with a Galerkin discretization for acoustic pressure and velocity. Limit cycle calculations using a single mode, as well as twenty modes, are compared against predictions from the CIRCE diagram. For the single mode system, the time domain calculations agree well with the frequency domain predictions. The heat release rate is highly nonlinear but, because there is only a single acoustic mode, this does not affect the limit cycle amplitude. For the twenty-mode system, however, the higher harmonics of the heat release rate interact with those of the acoustic velocity, resulting in a larger limit cycle amplitude. Multi-mode simulations show that, in some situations, the contribution from higher harmonics to the nonlinear dynamics can be significant and must be considered for an accurate and comprehensive analysis of thermoacoustic systems. Although the thermoacoustic system under consideration in this chapter is a simple ducted premixed flame, the fundamental nonlinear behaviour observed here is relevant to more complex thermoacoustic systems because the main source of nonlinearity is captured well.

Chapter 4

Nonlinear thermoacoustics of ducted premixed flames: the influence of perturbation convection speed

Summary

When a premixed flame is placed within a duct, acoustic waves induce velocity perturbations at the flame's base. These travel down the flame, distorting its surface and modulating its heat release. This can induce self-sustained thermoacoustic oscillations. Although the phase speed of these perturbations is often assumed to equal the mean flow speed, experiments conducted in other studies and Direct Numerical Simulation (DNS) conducted in this study show that it varies with the acoustic frequency. In this chapter, we examine how these variations affect the nonlinear thermoacoustic behaviour by modelling the velocity perturbation on DNS results. As in chapter 3, we calculate the flame describing function (FDF) using harmonic forcing at several frequencies and amplitudes. Then we calculate thermoacoustic limit cycles and explain their existence and stability by examining the amplitude-dependence of the gain and phase of the FDF. We find that, when the phase speed equals the mean flow speed, the system has only one stable state.

When the phase speed does not equal the mean flow speed, however, the system supports multiple limit cycles because the phase of the FDF changes significantly with oscillation amplitude. This shows that the phase speed of velocity perturbations has a strong influence on the nonlinear thermoacoustic behaviour of ducted premixed flames.

Nomenclature

k	Wavenumber
c	Phase speed
K	Ratio of streamwise base flow velocity to streamwise phase speed, $\tilde{u}_0/c_x$
f_{exc}	Forcing frequency
i	The complex number $\sqrt{-1}$
ϵ	Velocity perturbation amplitude normalized by its steady value
$\Delta\phi$	Velocity perturbation phase
s_L	Laminar flame speed
s_{Lu}	Unstretched laminar flame speed
T_u	Unburned gas temperature
Y	Mass fraction
W	Molecular weight
L_u	Markstein length
ω_1	Fundamental acoustic frequency of the duct
ν	Viscosity
χ	Thermal conductivity
T	Acoustic time period of one cycle of oscillation at the fundamental frequency
φ	Phase of any quantity in a Fourier expansion

Modifiers

$\hat{(\cdot)}$	Fourier component at the Strouhal number of the forcing
$(\cdot)_x$	Streamwise quantity
$(\cdot)_y$	Transverse quantity
$(\cdot)'$	Perturbation about the steady value
$(\cdot)_0$	Steady base flow value
$\lvert\cdot\rvert$	Magnitude of perturbations or gain of a function
$\angle\cdot$	Phase of perturbations or a function
$\tilde{(\cdot)}$	Dimensional quantity
$(\cdot)^*$	Non-dimensional quantity
$\langle\cdot\rangle$	Time average of the quantity over a forcing cycle

4.1 Introduction

In general, a velocity field can be decomposed into a steady base flow and acoustic, vortical and entropy perturbations [16]. Acoustic waves induce velocity perturbations at the base of the flame by exciting a convectively unstable shear layer. These velocity perturbations then travel along the flame, distorting its surface and therefore causing flame area fluctuations that result in unsteady heat release rate oscillations. This chapter concerns the model for the perturbation velocity field used in the G-equation model for the flame surface dynamics.

Several studies have investigated in detail the receptivity of shear layers to acoustic forcing and the enhanced generation of vorticity in separated shear layers by acoustic forcing, but most of these studies were for non-reacting flows. These have been reviewed by Wu *et al.* [117]. Similar studies for reacting shear layers are fewer, but are receiving more attention in recent years [118; 119; 120]. While these studies have generated a wealth of information about the response of shear layers to acoustic forcing, measurements or calculations of the phase speed of shear layer disturbances are limited, especially in the reacting case.

Experiments on laminar premixed flames by Boyer and Quinard [121] show that the hydrodynamic feedback from the flame changes the flow upstream, makes the acoustic field non-uniform and in particular, alters the convective speed of vortices that distort the flame surface. Experiments on forced conical premixed flames by Baillot *et al.* show that the disturbance propagation speed depends on the frequency but is independent of spatial location [107]. Velocity field measurements of an oscillating bunsen flame by Ferguson *et al.* show that streamwise disturbances are transported at a speed different from the average flow velocity [122]. Birbaud *et al.* investigated flows in acoustically excited free jets and premixed conical flames and found different oscillatory regimes that depend on the forcing frequency [123; 124]. In the convective regime they found that the perturbation convection speed depends on the forcing frequency and the distance from the burner exit plane but is independent of the forcing amplitude [123]. This is the most detailed study of the upstream flow dynamics of an acoustically forced bunsen flame. Durox *et al.* in their study of the acoustic response of various configurations of laminar premixed flames point out that an accurate description of the oscillating flow field, including the fluid motion in the shear layer region, is crucial to capture the flame response [115; 125]. Kornilov *et al.* show using particle image velocimetry measurements in a multi-slit burner that travelling waves are generated just upstream of the burner exit plane due to acoustic forcing [126; 127]. Karimi *et al.* show clearly from measurements of the perturbed flame surface of a forced bunsen flame that the disturbance convection speed along the flame is not equal to the mean flow [29]. They use their measured perturbation convection speeds to make more accurate estimates of the phase of the flame describing function.

Experiments on a slot burner by Kartheekeyan and Chakravarthy and experiments on rod-stabilized flames and bluff-body stabilized flames by Shanbhogue *et al.* and Shin *et al.* show that the vortices that roll up in the acoustically excited shear layer convect along the flame at a speed not necessarily equal to the mean flow and usually slightly lower than the mean flow [99; 128; 129; 130]. O'Connor *et al.* study the hydrodynamics of transversely excited swirling flow fields, both non-reacting and reacting, and show that the amplification of acoustic disturbances by convectively unstable shear layers dominate the wrinkling and dynamics of the flame [131; 132; 133]. Due to the multi-dimensional disturbances in their configuration, however, it was too complicated to extract a single phase speed of perturbations.

It is clear from the above studies that the disturbance characteristics in acoustically excited shear layers have a significant impact on the flame response and in particular, the convection speed of perturbations depends on several parameters and is not equal to the mean flow velocity.

These velocity perturbations that distort the flame surface are usually assumed to take the form of a traveling wave $\exp{[\mathrm{i}(kx - \omega t)]}$, for which the streamwise phase speed, c_x, is equal to ω/k. The ratio of the mean velocity, u_0, to this phase speed, c_x, is denoted K. Most models assume that the phase speed is equal to the mean flow velocity, *i.e.* that $K = 1$ [30; 95; 109]. Preetham *et al.* investigate the influence of the parameter K on the gain and phase of the transfer function and they conclude that nonlinear effects are enhanced for $K > 1$ [31]. They, however, do not measure the dependence of K on frequency and amplitude of the acoustic perturbations in their analysis.

In chapter-3 we showed that, if $K = 1$, the system has at most one limit cycle and that this limit cycle must be stable. However, recent experiments on similar systems show that there can be several limit cycles and that some are unstable [55; 57; 134]. Our analysis in chapter-3 captured this behaviour when K was greater than 1, but we did not justify this. In this chapter we justify the values of K for the simple thermoacoustic system of a ducted premixed flame. The aims of this chapter are (i) to extract K from Direct Numerical Simulation (DNS) of a premixed flame in order to provide an improved velocity perturbation model for inclusion in the G-equation; (ii) to use the G-equation model to calculate the flame describing function (FDF) between acoustic forcing and heat release response; (iii) to calculate the nonlinear behavior of the coupled self-excited thermoacoustic system and to explain its origin using the FDF.

4.2 DNS of a laminar premixed flame

The configuration studied consists of a 2-D slot-stabilized premixed methane-air flame inside a tube (Fig. 4.1). DNS of the fully compressible Navier–Stokes

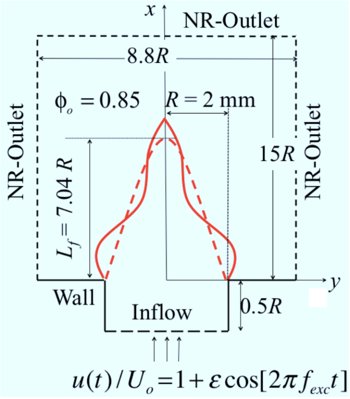

Figure 4.1: Schematic of the 2-D slot-stabilized premixed methane air flame. The dashed line represents the steady flame contour and the solid curve represents an instantaneous forced flame contour. NR stands for non-reflecting boundary conditions.

equations for reacting flows are performed using explicit eighth order central differences for spatial derivatives and a third order Runge-Kutta scheme for time integration. Tenth order spatial filtering is performed after every two timesteps to remove spurious numerical oscillations [135]. This DNS code has been recently used for premixed flames subjected to fuel-air ratio fluctuations [136]. The kinetic scheme is a single step irreversible global reaction used by Lacaze *et al.* [137] as follows. Chemical source terms are determined assuming a single step and irreversible global reaction: $\mathrm{CH_4} + 2\mathrm{O_2} \longrightarrow \mathrm{CO_2} + 2\mathrm{H_2O}$. The reaction rate, $\dot{\omega}$, is determined from the mass fractions of methane, $Y_{\mathrm{CH_4}}$ and oxygen, $Y_{\mathrm{O_2}}$, using the following expression (Lacaze *et al.* [137]):

$$\dot{\omega} = A\Big(\frac{\rho Y_{\mathrm{CH_4}}}{W_{\mathrm{CH_4}}}\Big)\Big(\frac{\rho Y_{\mathrm{O_2}}}{W_{\mathrm{O_2}}}\Big)\exp\Big(-\frac{E_a}{R_u T}\Big) \tag{4.1}$$

where, $A = 6.9 \times 10^{14}$ cm^{-3} mol^{-1} s^{-1}, $E_a = 132.1642$ kJ mol^{-1} and R_u is the universal gas constant. Figure 4.2 shows the variation of the unstretched laminar flame speed, s_{Lu}, as a function of ϕ computed using the above mechanism (see [136] for details).

The temperature-dependent thermodynamic properties, the viscosity, and the thermal conductivity for all species are determined from theoretically-derived

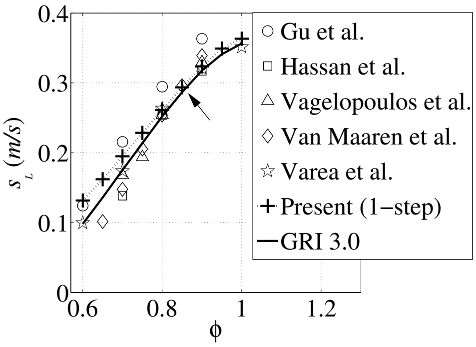

Figure 4.2: Variation of the laminar flame speed with the equivalence ratio (ϕ) for Methane-air flames. (T_u = 300 K, p_o = 1atm). The arrow shows the point corresponding to $\phi_o = 0.85$ at which forced computations are performed in this study. Figure reprinted from [136].

functions of temperature [138]. Mixture viscosity and thermal conductivity are determined from corresponding values for pure species using averaging rules [139; 140]. Mixture diffusivities of individual species are determined from their corresponding Lewis numbers (assumed constant).[1]

The domain is discretized using a structured mesh with nominal grid spacing of 40 μm. The reaction zone of the flame is always resolved over 10-15 grid points in these simulations. Grid independence has been checked by computing steady flames on successively refined grids up to a nominal grid size of 20 μm. The maximum change in computed solutions (across all flow variables and grid points) due to grid refinement, relative to the values on the nominal grid, is 8%.

A top-hat mean inlet velocity profile ($\tilde{u}_0$ = 2.52 ms^{-1}) is specified with an inlet boundary layer thickness of 0.2R and a constant temperature of 300 K. The wall temperature smoothly increases from 300 K at the inlet duct to 1200 K along the dump plane, across the 1 mm vertical section. The 2.4 mm horizontal section (labelled "wall" in Fig. 4.1) is at a constant temperature of 1200 K. This ensures that the flame remains attached to the slot lip. An adiabatic boundary condition was found to cause the flame to lift off. The wall temperature distribution was maintained constant at all times during the simulations.

We have chosen to anchor the base of the flame to a particular point in this

---

[1] Lewis Numbers: CH_4 = 0.97, O_2 = 1.11, CO_2 = 1.39, H_2O = 0.83.

study, in order to study only the influence of the perturbation convection speed. Motion of the flame base can have a significant influence on the overall system behaviour (see for example [31; 32; 126]). Experiments on forced premixed flames, however, show that flame base motion significantly affects the nonlinear flame response only at large forcing amplitudes [29]. We have also chosen to ignore flame lift-off. Recent experiments on a self-excited ducted premixed flame show that flame lift-off occurs at large velocity fluctuation amplitudes and can lead to complicated nonlinear behaviour such as intermittency, ultimately leading to flame blow-out [134; 141]. These results imply that our attached flame assumption will not be accurate for very large amplitude velocity fluctuations, however, they will be valid when the flame remains attached to the burner lip or when lift-off is prevented, for example by using a pilot flame.

These conditions yield a nominally steady flame with $\beta_f = {}^{L_f}/_{R} = 7.0$ (see Fig. 4.1). The inlet flow velocity is forced harmonically, ${}^{u(t)}/_{\tilde{u}_0} = 1+\varepsilon\cos[2\pi f_{exc}t]$, where the forcing frequency, f_{exc}, varies between 80 Hz and 460 Hz, and the forcing amplitudes, ε, are 0.05, 0.1 and 0.2. The global heat release response is found by integrating the volumetric heat release rate over the domain, 20 times per forcing cycle. The non-dimensional forcing frequency is represented by the Strouhal number, St (St$=f_{exc}L_f/\tilde{u}_0$) and varies between 0.44 (80 Hz) and 2.56 (460 Hz). The measured velocity fields are used to construct a reduced order velocity model, as described next.

4.2.1 Reduced order model for the velocity field

The streamwise perturbation velocity field, $u'(x, y, \varepsilon, \omega)$, is assumed to be of the form $\varepsilon\exp(\mathrm{i}(k_x x + k_y y - \omega t))$. The local wavenumbers in the x and y directions, k_x and k_y, depend on the frequency and amplitude of the forcing, and on the spatial location. By differentiating u' with respect to x and then to y the following relationships for the local wavenumbers are obtained:

$$\mathrm{i}k_x = \frac{1}{u'}\frac{\partial u'}{\partial x}; \quad \mathrm{i}k_y = \frac{1}{u'}\frac{\partial u'}{\partial y}. \tag{4.2}$$

The phase speeds in the x and y directions, c_x and c_y, are related to the forcing frequency, ω, and real components of k_x and k_y by $c_x = \omega/k_{x,r}$ and $c_y = \omega/k_{y,r}$.

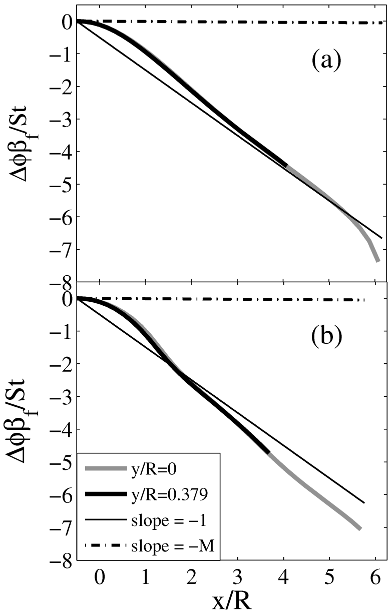

Figure 4.3: Variation of normalized velocity perturbation phase, $\Delta\phi\beta_f/\mathrm{St}$, along the streamwise coordinate, x/R, at different transverse coordinates, y/R, at $\phi = 0.85$ and $\varepsilon = 0.05$ for (a) $f_{exc} = 160Hz$ (St $= 0.88$) and (b) $f_{exc} = 320Hz$ (St $= 1.76$). The slope of the streamwise variation of the normalized phase is the non-dimensional phase speed of the velocity perturbations in the flow upstream of the flame. The normalized slope for an acoustic wave is shown by the dot-dashed line and for a convective wave with phase speed equal to the mean flow speed is shown by the thin solid black line.

Figures 4.3 (a) and (b) show the streamwise variation of the normalized velocity perturbation phase relative to the inlet, $\Delta\phi\beta_f/\mathrm{St}$ ($\Delta\phi = \angle\hat{u}' - \angle\hat{u}'_{inlet}$), at different transverse locations. The streamwise variation is shown up to the flame position at each transverse location, *i.e.* at points that are always upstream of the flame. The slopes of these curves give the non-dimensional phase speeds upstream of the flame. The slope for an acoustic wave is shown by the dot-dashed line (slope=$-$M=$-{}^{u_0}/_{\bar{c}_0}$) and that for a convective wave with phase speed equal to the mean flow speed ($K = 1$) is shown by a thin solid line (slope=-1).

Firstly, the phase is almost independent of the transverse coordinate, showing that the transverse wavenumber, k_y, is very small and the transverse phase speed, c_y, is very large, as seen in experiments by Birbaud *et al.* [123]. Secondly, the slope is uniform in the streamwise direction, except around the base and tip of the flame, showing that the streamwise wavenumber, k_x, and streamwise phase speed, c_x are mostly uniform. Close to the base, the slope is approximately $-\mathrm{M}$ because the acoustic perturbation components dominate in this inlet region and the wavelength is much larger than the flame length, as seen in experiments with conical flames by Birbaud *et al.* [123]. Most significantly, the overall slope is not exactly equal to -1, which means that the phase speed is not equal to the mean flow speed. This has important consequences for the nonlinear dynamics of these flames, as shown by Preetham *et al.* [31] and as seen in chapter 3.

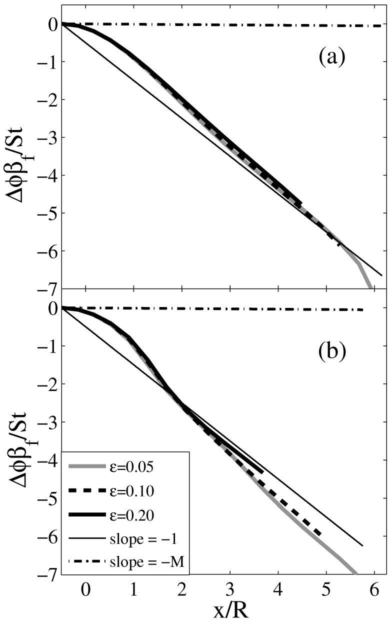

Figure 4.4: Variation of normalized velocity perturbation phase, $\Delta\phi\beta_f/\mathrm{St}$, along the centreline, $y/R = 0$, at different forcing amplitudes, $\varepsilon = 0.05, 0.10, 0.20$ for (a) $f_{exc} = 160Hz$ and (b) $f_{exc} = 320Hz$. The overlap of the plots shows clearly that the phase speed is independent of the forcing amplitude.

Figures 4.4 (a) and (b) show the normalized velocity perturbation phase, $\Delta\phi\beta_f/\mathrm{St}$ ($\Delta\phi = \angle\hat{u}' - \angle\hat{u}'_{inlet}$), along the centreline, $y/R = 0$, at three forcing amplitudes. The lines overlap, showing that the phase speed (and therefore the local wavenumber) is independent of the forcing amplitude, as noticed in experiments [123]. For the range of amplitudes examined in this study the phase speed was found to be independent of the amplitude, but we expect that this will not be true at very large forcing amplitudes. This shows that the perturbation travels in the streamwise direction with a nearly constant phase speed, which depends only on the forcing frequency. This allows us to simplify the model for u' to be of the form $\varepsilon \exp i(k_x x - \omega t)$, where k_x is a function of the forcing frequency alone. This can be written: $k_x = {}^{\omega}/_{c_x} = ({}^{\omega}/_{u_0}) * K$.

Figure 4.5 shows K as a function of the forcing frequency, St, for six forced DNS runs. The solid line is a least squares quadratic fit to these data, which is used for the G-equation model in this chapter. Although K is often assumed to equal 1 for G-equation models used in thermoacoustic systems [30; 95; 109], experiments have shown that this is not necessarily true [29; 99; 107; 115; 121; 123; 125; 128; 129; 130; 131; 132]. Figure 4.5 shows that this is not the case for the flame examined in this study. This figure shows that, for this particular flame, the perturbation phase speed is always lower than the mean flow velocity, except at St $\approx$ 1.5, when the perturbation phase speed is equal to the mean flow velocity. These values of K, however, cannot be generalised without performing detailed analysis into the hydrodynamic response of the flow field for different flame and flow configurations using either experiments or DNS.

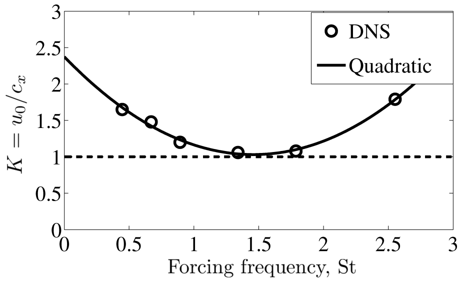

Figure 4.5: Ratio of the mean velocity to the disturbance phase speed, $K = u_0/c_x$, as a function of the forcing frequency, St, for $\phi = 0.85$. The solid line is a quadratic fit to the DNS data, which are shown as circles. The equation of the fit is $K = 0.631\text{St}^2 - 1.841\text{St} + 2.374$. Most models assume that $K = 1$ [30; 95; 109], shown by the horizontal dashed line.

The transverse perturbation velocity upstream of the flame, v', is determined using the incompressible continuity equation with $v' = 0$ at $y = 0$ [30]:

$$\frac{\partial u'}{\partial x} + \frac{\partial v'}{\partial y} = 0; \quad \frac{\partial \hat{v}'}{\partial y} = -ik_x\hat{u}'; \quad \hat{v}' = -ik_x\hat{u}'y. \tag{4.3}$$

Figure 4.6 shows the ratio of the transverse velocity perturbation, v', to the streamwise velocity perturbation, u', across the transverse coordinate, y/R. Points of v'/u' are plotted only for values where the temperature rise is less than 5% of the total temperature rise. These points are extracted from the forced DNS data at (a) St = 0.44 and (b) St = 1.78. The ratio of v'/u' is almost linear, except very close to the flame because of the sharp density gradient due to the temperature rise. This shows that the incompressible continuity equation (4.3) provides a very good approximation to v' upstream of the flame, which is the relevant region to consider for velocity perturbations in the G-equation model. In summary, the non-dimensional streamwise velocity field can be specified as a

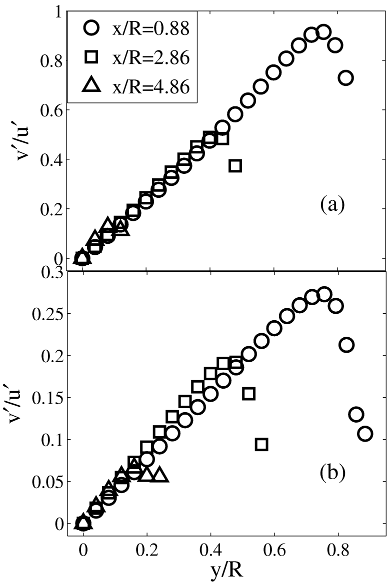

Figure 4.6: Ratio of transverse velocity to streamwise velocity perturbation, v'/u', across the transverse coordinate, y/R, derived from DNS at $\phi = 0.85$ and $\varepsilon = 0.05$ for (a) St = 0.44 and (b) St = 1.78. The transverse variation is shown up to the flame position at each streamwise location. In the unreacted stream, v'/u' is a linear function of y, in accordance with Eq. (4.3).

harmonically oscillating travelling wave, with the transverse velocity obtained by solving the incompressible continuity equation:

$$u = u(t)/\tilde{u}_0 = 1 + \varepsilon \cos(2\pi \mathrm{St}(Kx^* - t^*)), \tag{4.4}$$

$$v = v(t)/\tilde{u}_0 = \frac{2\pi\varepsilon \mathrm{St} K y^*}{\beta_f} \sin(2\pi \mathrm{St}(Kx^* - t^*)), \tag{4.5}$$

where K is obtained from the quadratic fit in Fig. 4.5.

This velocity model is combined with the G-equation model and used for a range of linear and nonlinear simulations of the forced flame response, in order to extract the FDF.

Figure 4.7 shows instantaneous flame images over one forcing cycle. The cusp formation and flame pinch-off found here have also been observed in several experiments [29; 98; 107; 121; 123; 125]. Note the differences in flame shape in this figure compared to Fig. 3.1: the flame wrinkles and cusps are more pronounced due to a more realistic velocity perturbation field.

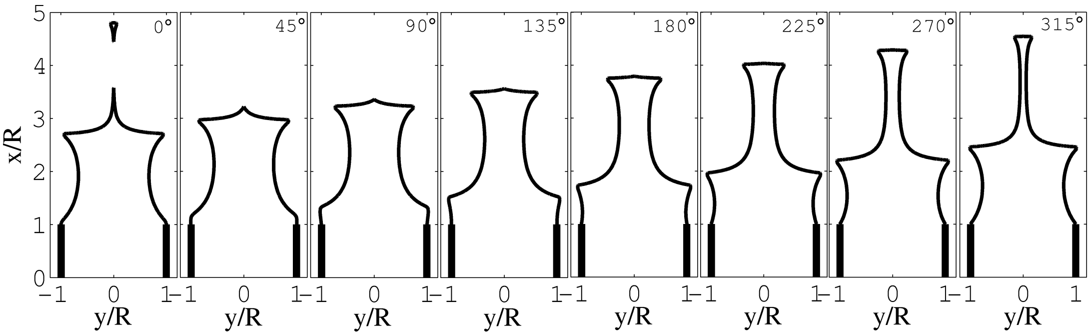

Figure 4.7: Instantaneous images of the flame during one forcing cycle, $\phi = 0.85$, $\beta_f = 5$, $\varepsilon = 0.4$, $\mathrm{St} = 2$, $K = 1.18$. Note the formation of sharp cusps towards the products and flame pinch-off, which are distinct characteristics of premixed flames seen in several experiments [29; 98; 107; 121; 123; 125]

4.3 Linear and nonlinear flame response: FDF

Figure 4.8 shows the gain and phase of the FDF of the heat release rate response to velocity perturbations for K obtained from the DNS (a and b) and for $K = 1$

(c and d). The forcing frequency, St, was varied from 0.04 to 2.5 in steps of 0.02. The forcing amplitude, ε, was varied from 0.02 to 0.6 in steps of 0.02. The amplitude of the streamwise velocity perturbation, ε, was used to define the FDF.

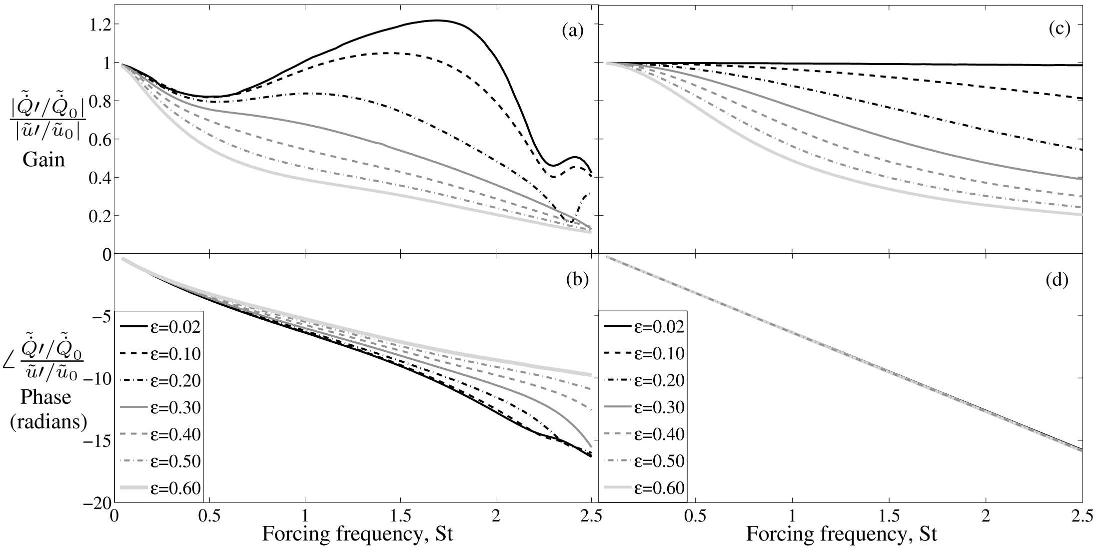

Figure 4.8: Flame Describing Function, $FDF(\omega, \varepsilon) = \frac{\tilde{\dot{Q}}'/\tilde{\dot{Q}}_0}{\tilde{u}'/\tilde{u}_0}$ a) Gain (K from DNS (varying)) and b) Phase (K from DNS (varying)). Note that as the forcing amplitude increases, the gain decreases monotonically and the phase changes significantly at high St. c) Gain (K = 1) and d) Phase (K = 1). Note that as the forcing amplitude increases, the gain decreases monotonically but the phase has negligible change. $\beta_f = 7$, $\phi = 0.85$

Figure 4.8(a) shows that at low forcing amplitudes, the gain exceeds 1 between St=1 and St=2 but drops quickly at higher St. As the forcing amplitude increases, the gain decreases monotonically everywhere, except at the highest St. Figure 4.8(b) shows that at low forcing amplitudes, the phase depends nearly linearly on St, which is characteristic of systems with a constant time delay. As the forcing amplitude increases, however, the phase changes significantly at a given St. At high St, where the change is particularly large, it is due to the reduction in the mean flame height and the movement of the location of peak heat release closer to the flame base. This has been seen in flame kinematic simulations [31], as well as in experiments [29; 142]. This differs from that of a model with $K = 1$ (Figure 4.8(d)) in which the FDF phase shows negligible dependence on the forcing amplitude (see Fig. 4.8(d)), also shown in previous studies [31; 100]. The amplitude-dependence of the phase of the FDF, however, has been shown to be highly influential on limit cycle behaviour as seen in chapter-3 and in previous studies [55; 115].

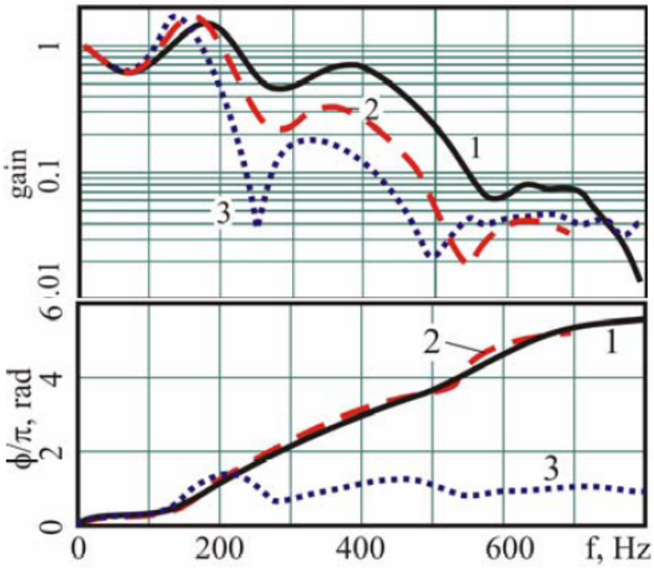

Figure 4.9: Figure reprinted with permission from V. N. Kornilov, “Experimental research of acoustically perturbed bunsen flames,” PhD Thesis, Eindhoven University of Technology (2006) [143]. Copyright ©Eindhoven University of Technology. The Flame Transfer Function, $FTF(\omega) = \frac{\tilde{\dot{Q}}'/\tilde{\dot{Q}}_0}{\tilde{u}'/\tilde{u}_0}$ of a multi-slit burner flame, $\phi = 0.9$, 1 - $\tilde{u}_0 = 1.2m/s$, 2 - $\tilde{u}_0 = 1.0m/s$, 3 - $\tilde{u}_0 = 0.8m/s$. The x axis scaling between Fig. 4.8 and the current figure is St = 1 is approximately $f_{exc} = 180Hz$. The phase plots have opposite signs because of the convention used in defining the phase (lag vs. lead). Note that at low frequencies, the gain decreases as the frequency increases, but rises to values above unity at intermediate frequencies before decreasing at high frequencies, as seen in Fig. 4.8. The phase is almost linear with frequency, except for the case with lowest mean flow velocity.

A quantitative comparison of FDFs from the G-equation and DNS is not possible because it is computationally too expensive and would deviate from the focus of this study. The qualitative behaviour of the FTF (flame transfer function, i.e. FDF at at the lowest forcing amplitude) resembles that measured by Kornilov in his PhD thesis (see Fig. 4.9 reprinted from [143]) but a quantitative comparison is not possible because the mean flow velocity in our numerical simulations (2.52 m/s) is much greater than in Kornilov's experiment (max 1.2 m/s), and as can be seen in Fig. 4.9, the mean flow velocity has a significant effect on the FTF.

A unique feature of the FTF of the 2-D slot-stabilized flame in this study is the initial decrease in gain at low St followed by an increase, with the gain exceeding unity for a range of St, and this compares well with experiments [143].

In §4.4, we show that the amplitude-dependence of the gain and the phase seen in Fig. 4.8(a) and (b) greatly affects the limit cycle behaviour of the coupled thermoacoustic system.

4.4 Nonlinear dynamics and limit cycle behaviour

The method used here is the same as that in §3.3. A single-mode assumption is used to calculate, analytically, limit cycle amplitudes and their stability.

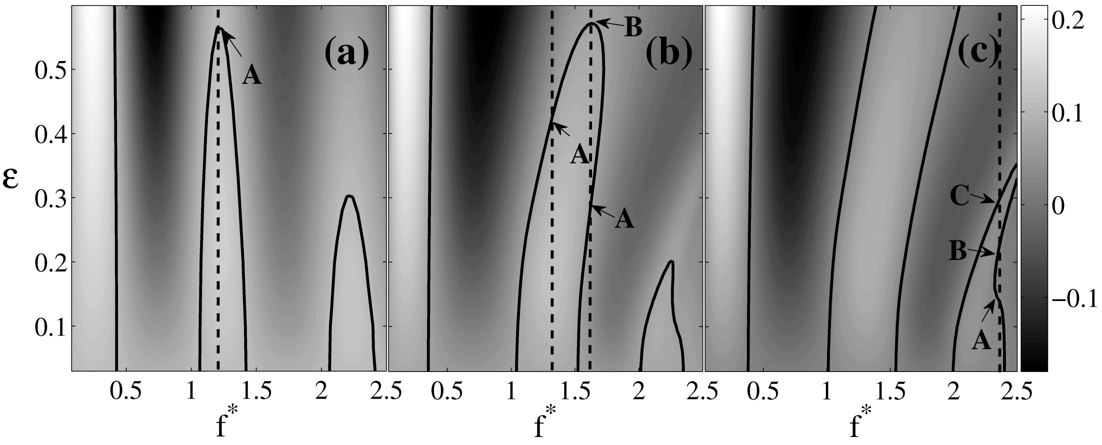

Figure 4.10: CIRCE diagram showing the net energy change over one cycle of oscillation, LHS of Eq. (3.11), as a function of velocity perturbation amplitude across thermoacoustic systems with different natural frequencies. (a) $K = 1$, $\zeta = 0.06$; (b) K from DNS (varying), $\zeta = 0.14$; and (c) K from DNS (varying), $\zeta = 0.06$. The grey-scale is such that regions where driving exceeds damping are light, while regions where damping exceeds driving are dark. The black boundaries between light and dark regions are limit cycles. The dashed lines in each frame represent the scenarios examined in Fig. 4.11.

Figure 4.10 shows the cyclic integral of rate of change of energy (CIRCE), the LHS of Eq. (3.11), as a function of velocity perturbation amplitude, ε, across thermoacoustic systems with different natural frequencies, f^*. Here $f^* = \tilde{c}_0 L_f / 2u_0 L_0$ and therefore, for a given flame, variation in f^* corresponds to varying duct lengths, or conversely, for a given duct, variation in f^* corresponds to varying flame height or varying Mach number. This figure shows the effect of the type of velocity model and strength of damping on limit cycle behaviour across a range of thermoacoustic systems. Figure 4.10(a) corresponds to systems with $K = 1$ and Fig. 4.10(b) and (c) correspond to systems with the K shown in Fig. 4.5. The damping factor, ζ, is 0.06, 0.14 and 0.06 for Fig. 4.10(a), (b) and (c) respectively. As described in §2.1, $\zeta = 0.06$ for a Rijke tube of length 70 cm, diameter 10 cm and average duct temperature of 350 K. The higher damping value of $\zeta = 0.14$ corresponds to a Rijke tube of length 50 cm, diameter 12 cm and average temperature 330 K. A lower damping value of $\zeta = 0.03$, as in Fig. 4.11(c), corresponds to a Rijke tube of length 100 cm, diameter 6 cm and average temperature 440 K. These numbers were chosen because they resemble laboratory-scale experiments. The grey-scale is such that regions where driving exceeds damping are light, while regions where damping exceeds driving are dark. The black boundaries between light and dark regions are limit cycles. Examining the behaviour along the x-axis at the lowest velocity perturbation amplitude, *i.e.* in the linear limit, shows that there exist bands of instability, as expected from linear stability analysis. For a particular system, the nonlinear behaviour is analyzed by examining the variation in CIRCE at a given f^* as a function of velocity perturbation amplitude. The dashed lines in each frame represent the scenarios examined in the Fig. 4.11, in terms of the number of limit cycles that exist and their stability.

In Fig. 4.11 the solid and dashed lines represent the driving and damping terms of Eq. (3.11). Figure 4.11(a) shows a system that is linearly unstable with a stable limit cycle at A, which corresponds to a supercritical bifurcation. On the other hand, Fig. 4.11(b) shows a system that is linearly stable with an unstable limit cycle at A and a stable limit cycle at B. If the system is given an excitation with amplitude greater than the amplitude of state-A, oscillations in the system will grow until the system reaches state-B. This phenomenon is called triggering [46; 47]. In a single-mode thermoacoustic system, the minimum

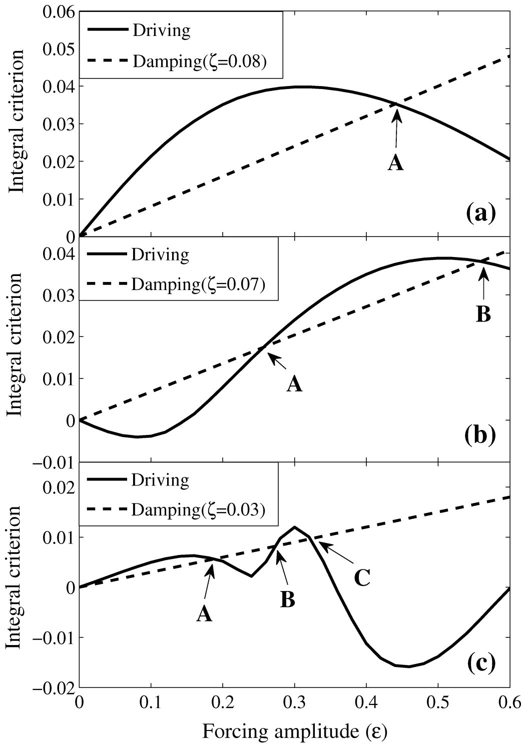

Figure 4.11: CIRCE for thermoacoustic systems with different fundamental frequencies (duct lengths), (a) Slice of Fig. 4.10(b) at $f^* = 1.4$, A - stable limit cycle, and (b) Slice of Fig. 4.10(b) at $f^* = 1.6$, A - unstable limit cycle, B - stable limit cycle (c) Slice of Fig. 4.10(c) at $f^* = 2.35$, A and C - stable limit cycles, B - unstable limit cycle

amplitude of an excitation that can cause triggering is the amplitude at point-A. This corresponds to a subcritical bifurcation. The system shown in Fig. 4.11(c) is linearly unstable, has stable limit cycles at A and C, and an unstable limit cycle at B. This corresponds to a supercritical bifurcation followed by two fold bifurcations.

The variations in the scenarios seen here are due to the amplitude-dependence of the gain and phase of the FDF [57] and their contributions to the driving term in Eq. 3.11. The supercritical bifurcation seen in Fig. 4.11(a) arises because the gain decreases as the forcing amplitude increases, while the phase remains fairly constant (see Fig. 4.8 (a) and (b)). The subcritical bifurcation seen in Fig. 4.11(b) arises because the phase changes significantly as the amplitude increases, as shown

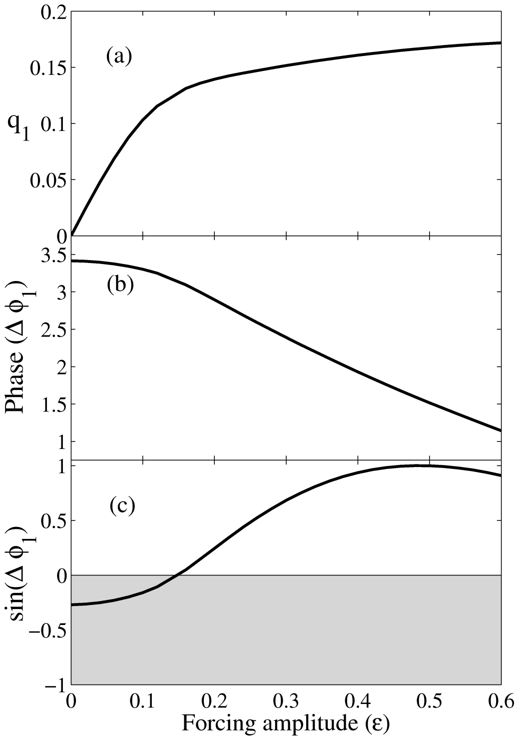

Figure 4.12: Amplitude dependence of the fundamental of heat release rate, q_1, phase, φ_1, and $\sin(\varphi_1)$, at $f^* = 1.6$. The subcritical behaviour of Fig. 4.11(b) is due to change in sign of $\sin(\phi)$ due to the large variation of the phase.

in Fig. 4.12(b). Crucially, this significant change in phase results in a change in sign of the $\sin(\varphi_1)$ factor in the driving term from negative at low amplitudes (grey patch) to positive at higher amplitudes (white patch) (Fig. 4.12(c)), which allows the existence of an unstable and a stable limit cycle. Physically, this means that the heat release changes from being stabilizing at small amplitudes to being destabilizing at large amplitudes, which implies that the system is linearly stable but susceptible to triggering and therefore must have a subcritical bifurcation. The supercritical bifurcation followed by two fold bifurcations seen in Fig. 4.11(c) is because the gain does not decrease monotonically but first decreases, then increases and then decreases again, as the forcing amplitude increases, i.e. it has two inflection points. Over this range of amplitudes, the heat release always remains destabilizing ($\sin(\phi)$ is positive) and therefore three limit cycles exist, one of which is unstable.

Preetham *et al.* in their study of the nonlinear dynamics of premixed flames defined the driving term, $H(\epsilon)$, to be equal to the gain of the FDF [31]. The phase was not included in calculating the driving term (see Fig. 22 in [31]). Based on this definition they concluded that the nature of limit cycles depended solely on the concavity of the FDF gain dependence upon the forcing amplitude. However, Eq. 3.11 can be satisfied only when $\sin(\phi)$ is positive, i.e. only for certain values of the FDF phase. Therefore both the gain and the phase, and their dependence on the forcing amplitude, determine the number of limit cycles that exist and their stabilities. Under certain conditions either the gain or the phase may dominate. When the phase variation is small and the heat release is destabilizing ($\sin(\phi) > 0$), then the amplitude dependence of the gain is more important. However, if the phase variation is large, then both the gain and phase are important, but the amplitude-dependence of the phase determines whether the heat release is stabilizing or destabilizing and when an abrupt switch from one to the other occurs.

Most importantly, when K is assumed to be unity, only supercritical bifurcations are possible (Fig. 4.10(a)). This is because a limit cycle is established solely due to the decrease in the gain of the FDF as the amplitude increases (see Fig. 4.8(c)) and the phase has no role to play because it does not vary with the forcing amplitude (see Fig. 4.8(d)). Figures 4.10 (b) and (c), which are seen only in simulations with the realistic velocity field, however, show clearly that when the phase speed is not equal to the mean flow velocity the nonlinear behaviour is more complex and different types of bifurcation are possible due to large variations in the gain and phase of the FDF.

4.5 Conclusions

This chapter examines the influence of the perturbation velocity field on the nonlinear thermoacoustic behaviour of a simple premixed flame in a tube. A reduced order model of the perturbation velocity field is obtained from forced Direct Numerical Simulation (DNS) of a 2-D premixed flame. The DNS show that the perturbation velocity can be simplified to a travelling wave with a frequency-dependent phase speed. The most important difference between this reduced order model and velocity models used currently is that the phase speed is not assumed to be equal to the mean streamwise flow velocity.

For thermoacoustic calculations, the flame is modelled using a nonlinear kinematic model based on the G-equation with the velocity model obtained from the DNS, while the acoustics are governed by linearised momentum and energy equations. Using open-loop forced simulations, the flame describing function (FDF) is calculated. The FDF phase has a strong amplitude-dependence, unlike that of past analyses which assumed the phase speed of velocity pertubations to be equal to the mean streamwise flow velocity.

The existence and stability of limit cycles is then explained using the amplitude-dependence of the gain and phase of the FDF. When the phase speed of velocity perturbations is assumed to equal the mean streamwise flow velocity, the system can have only one stable state. For the velocity model derived from DNS results, however, several limit cycles exist and the system has combinations of fold bifurcations and either supercritical or subcritical Hopf bifurcations, depending on the operating condition. We find that these multiple limit cycles are caused by the large variation in the gain and phase of the FDF as the oscillation amplitude increases. This variation arises because the velocity perturbations are not convected exactly at the mean streamwise flow velocity. This shows that the phase speed of velocity perturbations has a strong influence on the nonlinear thermoacoustic behaviour of ducted premixed flames.

Chapter 5

Nonlinear self-excited thermoacoustic oscillations of a ducted premixed flame: bifurcations and routes to chaos

Summary

In previous chapters we have examined simple limit cycle oscillations and their stability using the single-mode approximation. Recent experimental studies have shown that self-excited thermoacoustic oscillations are not always periodic. In this chapter we study the bifurcations and routes to chaos of a ducted slot-stabilized two-dimensional premixed flame using time domain simulations of the coupled nonlinear dynamical system. We examine the bifurcations of the system for three control parameters: i) the flame position in the duct, ii) the length of the duct, and iii) the mean flow velocity.

When a control parameter is varied, the system undergoes transition to period-1, period-2, quasi-periodic and chaotic oscillations via different bifurcations. For certain parameter ranges more than one stable state exists and the ultimate state reached depends on the initial conditions. Hence there is hysteresis and mode switching is possible.

The system is transiently attracted to and repelled from unstable states and this is shown to be an important step in switching from one attractor to another. Furthermore, two routes to chaos are established for this system: the period-doubling route and the Ruelle-Takens-Newhouse route and these are corroborated by analyses of the power spectra of the acoustic velocity. Instantaneous flame images reveal that the wrinkles on the flame surface and pinch off of flame pockets are regular for periodic oscillations, while they are irregular and have multiple time and length scales for quasiperiodic and aperiodic oscillations.

This study complements recent experiments by providing a reduced order model of a system with approximately 5000 degrees of freedom that captures much of the elaborate nonlinear behaviour of ducted premixed flames observed in the laboratory.

5.1 Introduction

Most studies of nonlinear thermoacoustics are in the frequency domain. These studies assume *a priori* that the oscillations are periodic with a dominant frequency and a fixed amplitude [27; 55; 144]. Recent experiments, however, reveal that even simple thermoacoustic systems exhibit nonlinear behaviour that can be far more elaborate than period-*1* limit cycle oscillations [56; 64; 65]. By varying a control parameter in their thermoacoustic system consisting of an axisymmetric laminar conical flame in a duct, Kabiraj *et al.* show that the system undergoes several bifurcations resulting in quasi-periodic, frequency-locked, and chaotic oscillations [56]. Experiments in large industrial-scale thermoacoustic systems by Gotoda *et al.* show that, as the equivalence ratio increases, the thermoacoustic behaviour undergoes a transition from stochastic fluctuations to periodic oscillations through low-dimensional chaotic oscillations, revealing similarly elaborate nonlinear behaviour [66; 67].

Few studies of nonlinear thermoacoustics are in the time domain. These studies do not assume *a priori* that the system reaches period-*1* oscillations [36; 40; 62; 63; 75; 145]. These studies show that the influence of harmonics, and the interaction between different modes can be found in the time domain approach. Most of these studies, however, are limited by the assumption that the unsteady heat release rate is a simple, often polynomial, function of the pressure or velocity fluctuations. This assumption is unrealistic because the heat release rate of flames depends not only on the instantaneous acoustic pressure or velocity, but also on the integrated effect of historical values [146]. Therefore, simple analytical descriptions of heat release rate that do not account for memory effects cannot capture the complexities of unsteady flame dynamics.

In this chapter, therefore, we do not assume *a priori* that the system reaches a period-*1* oscillation. We study the nonlinear behaviour using numerical simulations of the coupled nonlinear dynamical system in the time domain. The aims of this chapter are: 1) to use techniques and well-established results from dynamical systems theory and nonlinear time series analysis to characterize the nonlinear behaviour of this system, and 2) to use instantaneous flame images of the different types of oscillation to interpret the elaborate nonlinear behaviour of this system.

In §5.2 we describe the aspects of the model specific to this chapter. In §5.3 we identify the bifurcations of this system due to variation of: 1) the flame position in the duct, which changes the amplitude and the frequency content of the acoustic perturbations at the flame, 2) the length of the duct, which changes the acoustic frequencies of the system, and 3) the mean flow velocity, which changes the flame geometry. We also examine the influence that the number of coupled acoustic modes has on these bifurcations. In §5.4 we characterize the states of the system using power spectra, phase portraits, Poincaré sections and correlation dimensions. In §5.5 we highlight the role of unstable attractors in the trajectory of the system from its initial condition to its final stable state. In §5.6 we identify two routes to chaos seen in this system: the period-doubling route and the Ruelle-Takens-Newhouse route. We show the sequence of steps in these routes to chaos using Poincaré sections and power spectra and we find the maximal Lyapunov exponents of the final chaotic states. In §5.7 we show instantaneous flame images of different types of oscillation and examine the flame wrinkling and pinch off behaviour of each type of oscillation. In §5.8 we discuss the implications of this elaborate nonlinear behaviour for the prediction of thermoacoustic oscillations.

5.2 Models and methods

In chapter-4 it was shown that the phase speed of velocity perturbations is not equal to the mean flow. It is a function of the forcing frequency but is independent of the forcing amplitude. Furthermore, it is usually less than the mean flow in the range of frequencies relevant to thermoacoustic oscillations.

In general, the acoustic perturbations in thermoacoustic systems are non-harmonic and we cannot use a frequency-dependent phase speed in time-domain simulations because these frequencies are not known *a priori*. For this reason we assume a constant phase speed, for which the non-dimensional streamwise perturbation velocity field is found by solving the 1-D advection equation,

$$\frac{\partial u}{\partial t} + \frac{U_c}{U_0}\frac{\partial u}{\partial x} = 0. \tag{5.1}$$

The phase speed of velocity perturbations, U_c, is equal to $0.9U_0$. In chapters 3 and 4 we have shown that U_c has a strong effect on the nonlinear behaviour of the thermoacoustic system and that subcritical bifurcations are more likely to exist for $U_0 > U_c$ than for $U_0 = U_c$. The boundary condition is that the perturbation at the burner lip equals the acoustic velocity at the flame position, $u(x_{burner}, t) = u_{acoustic}(x_f, t)$. Therefore the axial velocity at any point in the flame domain is the delayed acoustic velocity at the burner lip, with a delay equal to the time taken for the travelling wave to propagate from the burner to that point. As in chapter-4, we solve the continuity equation within the flame domain to find the transverse velocity.

5.2.1 Terminology in nonlinear dynamics

Here we briefly summarize some terms from nonlinear dynamics [34; 61; 147; 148; 149].

As time tends to infinity, any unforced dissipative dynamical system converges to a point, line, surface or higher dimensional manifold in phase space. This is called an attractor. The states that converge to each attractor comprise its basin of attraction. The boundary of this nonzero volume is called the basin boundary. Some points, lines, surfaces, or higher dimensional manifolds repel all trajectories.

These are called repellors. Other manifolds attract trajectories in some directions and repel them in other directions. These are called unstable attractors [150].

The behaviour of dynamical systems can change as parameters are varied; fixed points, saddle nodes and limit cycles can be created or destroyed, or their stability can change. These qualitative or topological changes are called bifurcations, and the parameter values at which they occur are called bifurcation points.

A trajectory of a dynamical system traces out its evolution over time in a phase space. Ensembles of trajectories fill the phase space to form a phase portrait, which shows the structure of the attractors and basins of the dynamical system.

A slice through the phase portrait of an n-dimensional dynamical system which generates an *(n-1)*-dimensional section is called a Poincaré section. It provides a means to visualize attractors. A Poincaré map takes a point on the surface of the Poincaré section to its image upon first return to the section. The Poincaré map has the same stability properties as the dynamical system.

5.2.2 Nonlinear time series analysis

Here we briefly describe some methods to analyze nonlinear time series [151; 152].

In most systems not all the state variables are known or can be measured. Takens' embedding theorem [153] shows how a time series of a single observable can be used to reconstruct a phase space with sufficient number of dimensions such that trajectories do not cross each other in finite time, *i.e.* all the active degrees of freedom of the dynamical system can be captured [151]. The state vectors are constructed using delayed vectors formed from the time series. The number of dimensions required is called the embedding dimension.

Several methods have been developed to find the optimal delay and the minimum embedding dimension that yield a faithful representation of the state space [151]. In this study we use the first zero-crossing of the auto-correlation function to determine the optimal delay, i.e. the delay which can reconstruct independent vectors from the time-series [154]. Sometimes the average mutual information is preferred because it is a nonlinear measure, while the auto-correlation function is linear [155]. We have compared delays obtained by using the first zero-crossing of the auto-correlation function and the first minimum of the average mutual information and they are almost identical for most of our simulations. Therefore we choose to use the auto-correlation method for speed. There is no rigorous way of determining the optimal delay and, in fact, the actual value of the delay has no relevance in the mathematical framework of dynamical systems [151]. The delay affects only the quality of the phase space reconstruction.

Calculating the minimum embedding dimension is crucial to avoid false neighbours in the reconstructed phase space, i.e. points that appear to be neighbours because they have been projected on to a lower dimensional space but are actually far apart in the true state space. The minimum embedding dimension depends on the number of active degrees of freedom in the system [153] and can be found by the method of false nearest neighbours proposed by Kennel *et al.* [156]. Using this method we find that the percentage of false nearest neighbours for time series from most of our simulations is less than 8% for an embedding dimension of 3 and less than 2% for an embedding dimension of 4. Therefore we use 3 embedding dimensions to construct phase portraits.

The correlation dimension measures the number of active degrees of freedom in a dynamical system and can be used to determine the nature of an attractor. For example, limit cycles have a correlation dimension of one, quasi-periodic attractors (2-tori) have a correlation dimension of two and chaotic attractors have fractional correlation dimension. We use the algorithm of Grassberger & Procaccia [157] with up to 7 embedding dimensions for reliable convergence in our calculations of correlation dimensions.

Lyapunov exponents measure the rate of divergence of neighbouring trajectories [151]. A positive maximal Lyapunov exponent is a signature of chaos and can be computed from well-resolved measurements using an algorithm developed by Kantz [158]. For reliable convergence we use up to 8 embedding dimensions to find the maximal Lyapunov exponent of the chaotic cases in §5.6.

5.3 Bifurcation analyses

A bifurcation diagram shows the changes in the nature of solutions to the governing equations as a single control parameter changes. The governing equations of the coupled nonlinear dynamical system are marched forward in time starting from the steady unperturbed state until the system reaches its stable state. At a particular value of the control parameter, the points on these bifurcation diagrams are the peaks and troughs of the time series of acoustic velocity at the flame position, *i.e.* $u_f = u(x_f)$, after the system reaches its stable state. Therefore, a period-*1* oscillation has two points (one peak and one trough), a period-*2* oscillation has four points, a period-k oscillation has $2k$ points, and quasiperiodic and chaotic oscillations have an infinite number of points bounded within a range of u_f. In practice, the number of points for quasiperiodic and chaotic oscillations depends on the length of the time series. In the diagrams that follow we show only the stable states. The unstable states are shown separately later. We choose u_f, the acoustic velocity at x_f, as the relevant physical quantity on these diagrams for two reasons: (i) it is the perturbation velocity at the burner exit and is often measured in experiments [125], and (ii) it pertubs the base of the flame creating flame wrinkles that travel along the flame, which play an important role in the behaviour of the unsteady heat release rate.

5.3.1 Control parameter: flame position, x_f

Figure 5.1 shows the bifurcation diagram with the flame position, x_f, as the control parameter. The flame position influences how the flame affects the acoustics, and how the acoustics affects the flame. This is because the contribution of each mode to the acoustic velocity is $\eta_j \cos(j\pi x_f)$, and the contribution of the heat release to each mode is $\beta\dot{Q}\sin(j\pi x_f)$, where η_j is the velocity amplitude of the jth mode and β encapsulates all relevant information about the steady flame, base velocity and ambient conditions.

The initial condition for the simulation at a new flame position is the final stable state of the previous flame position. This diagram is constructed using two sets of time-marching simulations, one by increasing x_f and the other by decreasing x_f, in order to find hysteresis in the system. This diagram shows the combined results from both sets of simulations. The different colours represent the most dominant acoustic mode in the power spectra: mode-1 is shown in red, mode-2 in blue, mode-3 in black and mode-4 in green. This chart shows that the system can have a stable fixed point (labelled FP), stable period-*1* oscillations

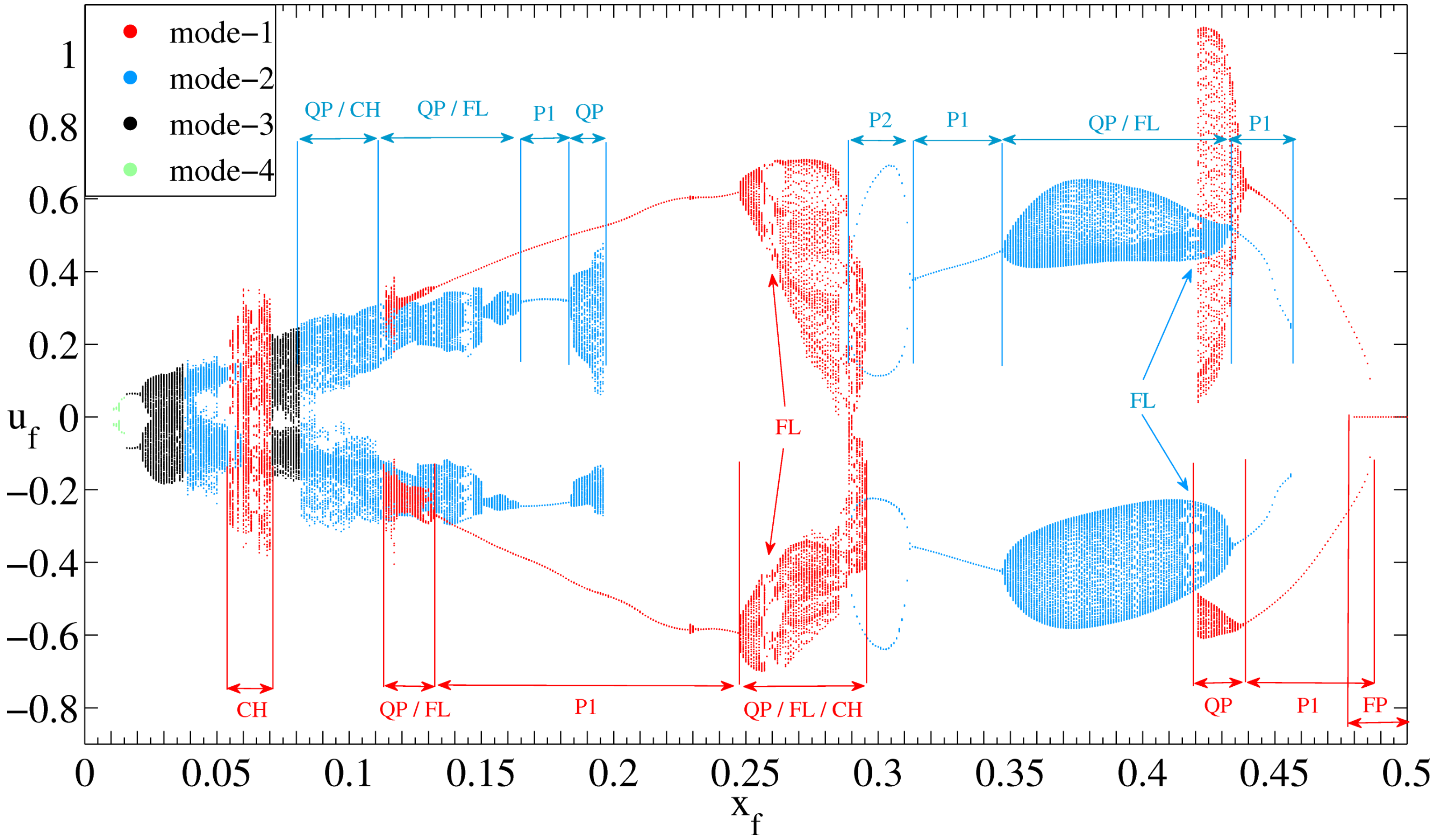

Figure 5.1: Bifurcation diagram with flame position, x_f. $\phi_{mean} = 0.85$, $\beta_f = {}^{L_f}/_{R} = 7$, ratio of combustion to acoustic time scales $= {}^{L_f}/_{ML_0} = 2.2$.

(labelled P1), period-*2* oscillations (labelled P2), frequency-locked or period-k oscillations (labelled FL), quasi-periodic oscillations (labelled QP) and chaotic oscillations (labelled CH) depending on the x_f and initial conditions.

The sequence of bifurcations from right to left (decreasing x_f) are: a subcritical Hopf from a stable fixed point to an unstable period-*1* oscillation at $x_f = 0.48$, a fold from an unstable to a stable period-*1* oscillation (mode-1) at $x_f = 0.487$, a supercritical Neimark-Sacker to quasi-periodic oscillations at $x_f = 0.438$. This branch of states (mode-1) loses stability at $x_f = 0.42$. A second stable branch with a dominant frequency near that of mode-2 begins at a fold bifurcation to period-*1* oscillation at $x_f = 0.456$. This branch has a supercritical Neimark-Sacker bifurcation to quasi-periodic oscillations at $x_f = 0.434$. In the narrow band of $0.415 < x_f < 0.422$ on the mode-2 branch the system has period-k states, seen as just a few points on the diagram, as against many points in the quasi-periodic case. For $0.347 < x_f < 0.415$ the system has quasi-periodic oscillations and this branch goes to a period-*1* oscillation via a supercritical Neimark-Sacker bifurcation at $x_f = 0.347$. The system undergoes a subcritical period-doubling bifurcation followed by a fold bifurcation at $x_f = 0.311$ to period-*2* oscillations, which lose stability at $x_f = 0.289$ where the period-*2* branch ends abruptly.

Similar features are noticed for lower values of x_f. Between $x_f = 0.03$ and $x_f = 0.1$ and between $x_f = 0.27$ and $x_f = 0.295$ there exist bands of chaos. For sizeable intervals of x_f at least two stable attractors co-exist and the final state reached by the system therefore depends on the initial conditions. Hence the system shows hysteresis and mode-switching is possible in these bi-stable regions.

5.3.2 Dependence on the number of modes used in the discretization

The number of Galerkin modes, N_g, used in the discretization of the acoustic equations affects the solutions to the governing equations of the coupled system. When there is more than one Galerkin mode, the heat release rate excites all the modes and each mode in turn affects the heat release rate via the velocity perturbation field. This couples the individual ODEs for each mode, resulting in a non-harmonic acoustic waveform and more complex behaviour than that in the

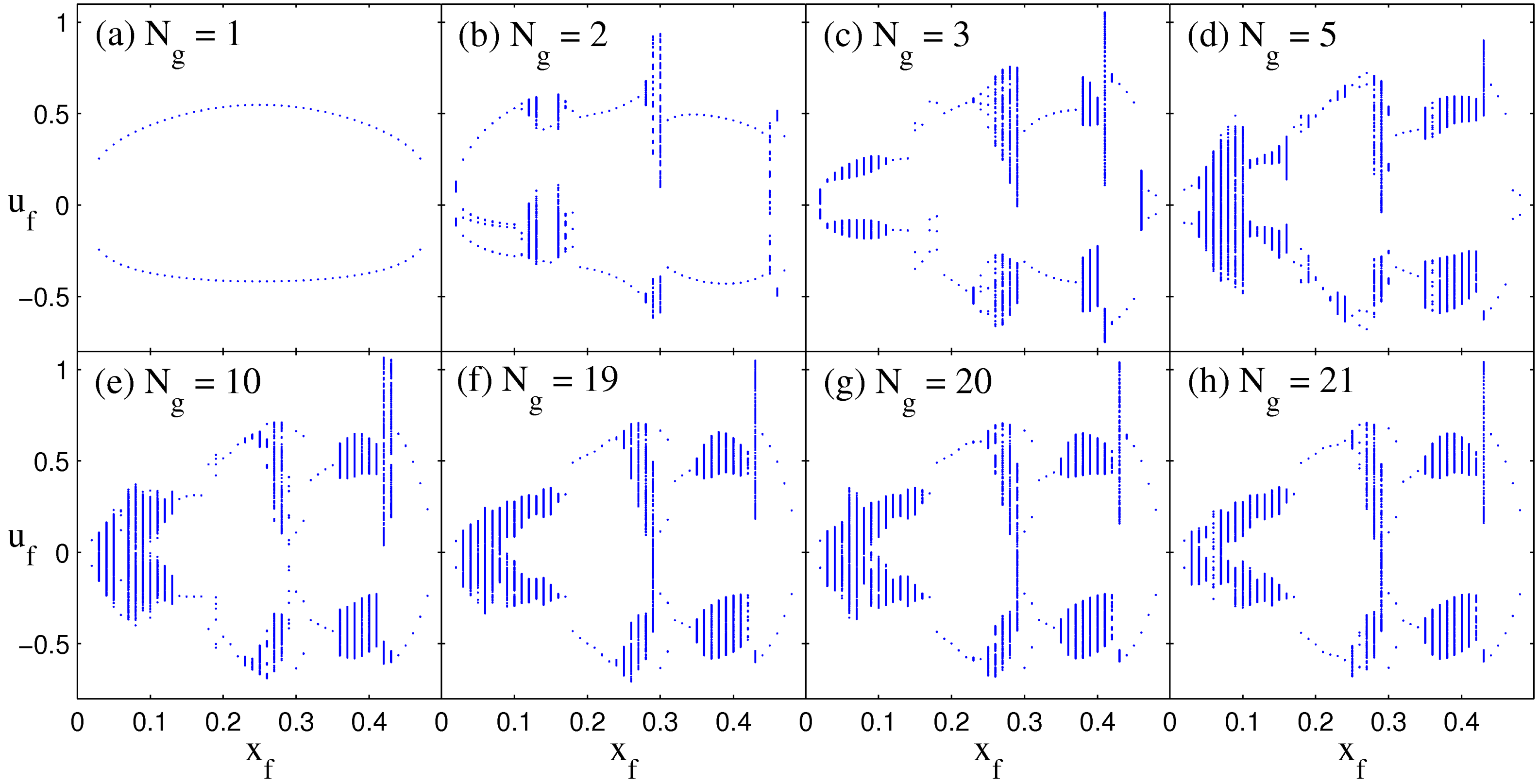

Figure 5.2: Bifurcation diagrams with flame position, x_f, as control parameter with different numbers of modes, N_g, in the discretization: (a)$N_g = 1$, (b)$N_g = 2$, (c)$N_g = 3$, (d)$N_g = 5$, (e)$N_g = 10$, (f)$N_g = 19$, (g)$N_g = 20$ and (h)$N_g = 21$.

single-mode case.

Figure 5.2 shows bifurcation diagrams with flame position, x_f, as control parameter using different numbers of modes, N_g. Figure 5.2(a) shows that when there is just 1 mode, the system is either stable or reaches a period-*1* limit cycle. The maximum oscillation amplitude occurs at $x_f = 0.25$ and is about one half of the mean flow. In chapter-3 we have shown that period-*1* limit cycles obtained in the frequency domain using a flame describing function (FDF) approach are the same as those obtained in the time domain using a single mode in the discretization. This is because the FDF approach ignores the influence of the higher harmonics of the heat release rate on the acoustic velocity and pressure, as is the case when only one mode is used for the discretization. Therefore figure 5.2(a) is the result obtained when the FDF approach is used to find limit cycles around the fundamental mode of the system. Note that the FDF can be used to find limit cycles at any frequency, not just around the fundamental. This can also be done in the single-mode analysis described in §3.3 by using the appropriate harmonic in the series expansion for the acoustic velocity, pressure and heat release rate perturbations.

Figures 5.2(b) to (h) show that as the number of modes is increased, period-*2*, quasi-periodic and chaotic oscillations appear. Furthermore, the peak amplitudes of oscillations are significantly higher than the single-mode case. This shows that even though the amplitudes of oscillations in the higher modes are smaller than in the first mode they have a strong effect on the amplitude of heat release rate oscillations, and therefore on the nature of solutions of the governing equations.

Subfigures (f), (g) and (h), at $N_g = 19$, 20 and 21, show that the solutions are nearly independent of the discretization when N_g is sufficiently large. Therefore we use 20 modes for this study.

In the time domain, only 3 to 5 modes are necessary to capture most of the elaborate features seen in the case with 20 modes (figure 5.2(g)). In the frequency domain, however, it is difficult to extend the FDF approach to include the effect of interactions between modes. This requires many multi-input multi-output describing functions, which can only be calculated by forcing the flame at many different combinations of frequencies and amplitudes simultaneously [159]. This becomes prohibitively expensive even for a small number of modes.

5.3.3 Control parameter: flame geometry, (L_f/R)

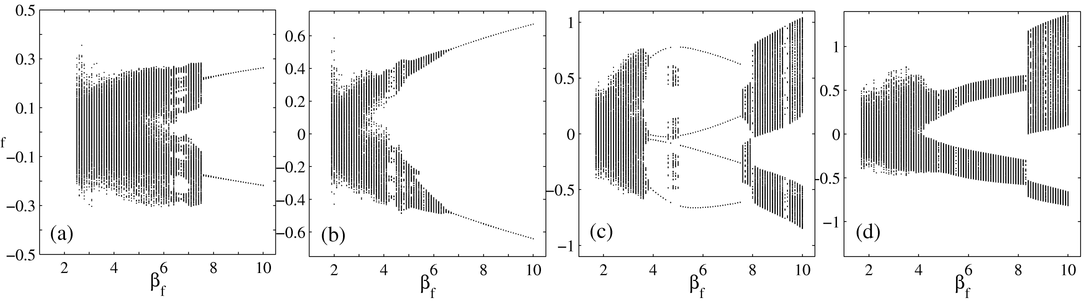

Figure 5.3: Bifurcation diagrams with flame aspect ratio, $\beta_f = {}^{L_f}/_{R}$, as control parameter at (a) $x_f = 0.1$, (b) $x_f = 0.2$, (c) $x_f = 0.3$, and (d) $x_f = 0.4$.

Figure 5.3 shows the bifurcation diagram with the flame aspect ratio (the ratio of the flame height to the flame radius, $\beta_f = {}^{L_f}/_{R}$) as the control parameter at four flame positions, (a) $x_f = 0.1$, (b) $x_f = 0.2$, (c) $x_f = 0.3$ and (d) $x_f = 0.4$. The range of β_f is 1 to 10, which corresponds to mean flow velocities in the range of 0.5 to 3.5 ms^{-1}. This range is realistic because laminar premixed flames with $\phi_{mean} = 0.85$ tend to either flashback or blow off for mean flow velocities outside this range. In all cases the initial condition is the steady unperturbed flame. β_f is varied by changing the mean flow velocity U_0 keeping the equivalence ratio and flame speed constant.

In Fig 5.3 (a), (b) and (c), the system transitions to quasi-periodic oscillations via Neimark-Sacker bifurcations. In (c) and (d) the system moves from the basin of one quasi-periodic attractor to another at $\beta_f \approx 8$. In all cases, when β_f is decreased below 3, the system has chaotic oscillations. The route to chaos here is the Ruelle-Takens-Newhouse route and is described in detail in §5.6. The system tends to chaos at low flame aspect ratios because cusps form on the flame surface at much lower oscillation amplitudes for short flames than for long flames. Since cusp formation and subsequent destruction by kinematic restoration (the propagation of the flame normal to itself) are among the main sources of nonlinearity in premixed flame dynamics, short flames have stronger nonlinearities than long flames. Therefore flame geometry plays a crucial role in the nonlinear dynamics of premixed flames, as shown by Lieuwen, using the analytical expression for the heat release rate in the flame tracking equation, which is derived from the *G*-equation [100]. Lieuwen showed that this expression can be simplified to a linear function of velocity for long flames, but is a nonlinear function for short flames.

5.3.4 Control parameter: duct length, L_0

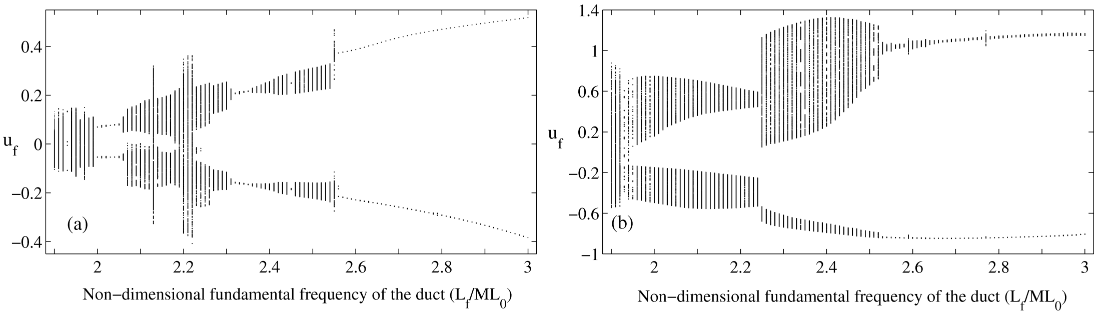

Figure 5.4: Bifurcation diagrams with non-dimensional fundamental frequency of the duct as control parameter at $x_f = 0.07$ in (a) and $x_f = 0.4$ in (b).

Figure 5.4 shows the bifurcation diagram with the nondimensional fundamental frequency of the duct, L_f/ML_0, as control parameter at two flame positions, (a) $x_f = 0.07$ and (b) $x_f = 0.4$. In all the simulations the initial condition is the steady unperturbed flame. The fundamental frequency of the duct is varied by changing its length, L_0, keeping all other parameters constant. Note that the ratio of combustion to acoustic time scales, L_f/ML_0, varies when L_0 changes.

In both Fig 5.4(a) and (b), the system has period-*1* oscillations when the duct is short, *i.e.* its fundamental acoustic frequency is high, but has more elaborate oscillatory behaviour when the duct is long, *i.e.* its fundamental acoustic frequency is low. In this range of frequencies the flame response remains fairly constant (see Fig 4.8(a) and (b)). The damping due to acoustic radiation scales as the square of the frequency, therefore, higher modes in short ducts are more heavily damped than those in long ducts. Hence systems with short ducts, *i.e.* high L_f/ML_0, tend to behave like single-mode systems.

5.4 Nonlinear time series analyses

In this section we apply the techniques described in §5.2.2 to analyse the time series obtained from simulating the self-excited system.

5.4.1 Nonlinear time series

Figure 5.5 shows the time series of the acoustic velocity at the flame position normalised by the mean flow velocity, U_0, and the heat release rate normalised by the mean heat release, $\dot{Q}_0$, for 5 flame positions in figure 5.1: (a) $x_f = 0.45$, (b) $x_f = 0.3$, (c) $x_f = 0.4$, (d) $x_f = 0.286$ and (e) $x_f = 0.046$. These are obtained by timemarching from the steady unperturbed flame. In all cases the system, is linearly unstable so perturbations grow exponentially before nonlinear effects dominate.

In figure 5.5(a) the system is first attracted towards an unstable period-*1* oscillatory state before being repelled from it and is then attracted to a period-*1* attractor. The velocity and heat release rate oscillations are periodic but not harmonic. In figure 5.5(b) the system is first attracted towards an unstable quasi-periodic state before being repelled from it and is then attracted to a period-*2* attractor. In figure 5.5(c) the system tends towards a quasi-periodic attractor. In figure 5.5(d) the system is first attracted towards an unstable quasi-periodic oscillatory state before being repelled from it and finally tending towards a period-*5* attractor. In figure 5.5(e) the system tends towards a chaotic attractor. The different attractors are characterised more precisely in subsequent sections.

5.4.2 Power Spectra

Power spectra of the different time series in figure 5.5 are obtained using MATLAB's pwelch command, which computes the power spectral density of a time series using Welch's overlapped segment averaging spectral estimation algorithm. This is applied on 300 nondimensional time units after the system has reached its stable state.

Figure 5.6 shows power spectra of the velocity at the flame position on the left (a1 to e1) and heat release rate on the right (a2 to e2). Figure 5.6(a) shows

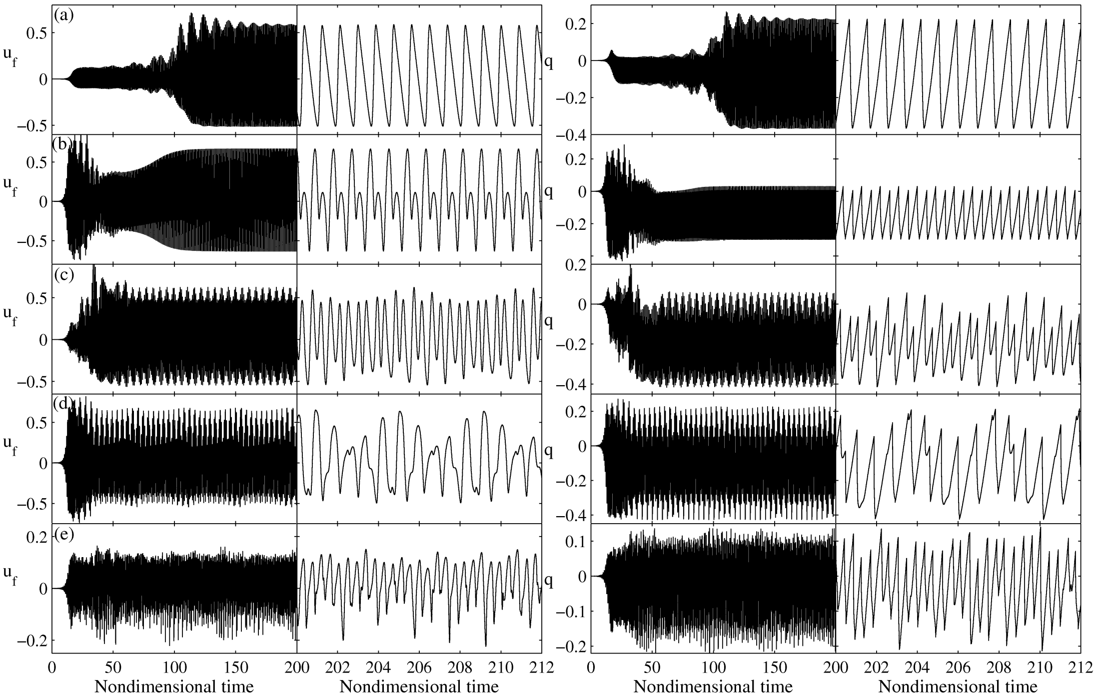

Figure 5.5: Time series of velocity and heat release rate for the different types of oscillation corresponding to different flame positions of figure 5.1: (a) period-*1* oscillation at $x_f = 0.45$, (b) period-*2* oscillation at $x_f = 0.3$, (c) quasi-periodic oscillation at $x_f = 0.4$, (d) frequency-locked oscillation at $x_f = 0.286$ and (e) chaotic oscillation at $x_f = 0.046$.

that spectra of period-*1* oscillations have a dominant frequency and its higher harmonics because the signal is not sinusoidal. Figure 5.6(b) shows that spectra of period-*2* oscillations have a dominant peak and a second peak at exactly half the frequency, and their higher harmonics. Figure 5.6(c) shows that spectra of quasi-periodic oscillations have several frequencies. In these spectra only two frequencies, however, are independent and incommensurate with each other while all the others are linear combinations of the two independent frequencies. These combinations arise due to nonlinear interactions between the two independent frequencies. Figure 5.6(d) shows the spectra of period-*5* oscillations, which resemble Figure 5.6(c). The two independent frequencies in this case, however, are commensurate with each other. As in Figure 5.6(c), combinations of the

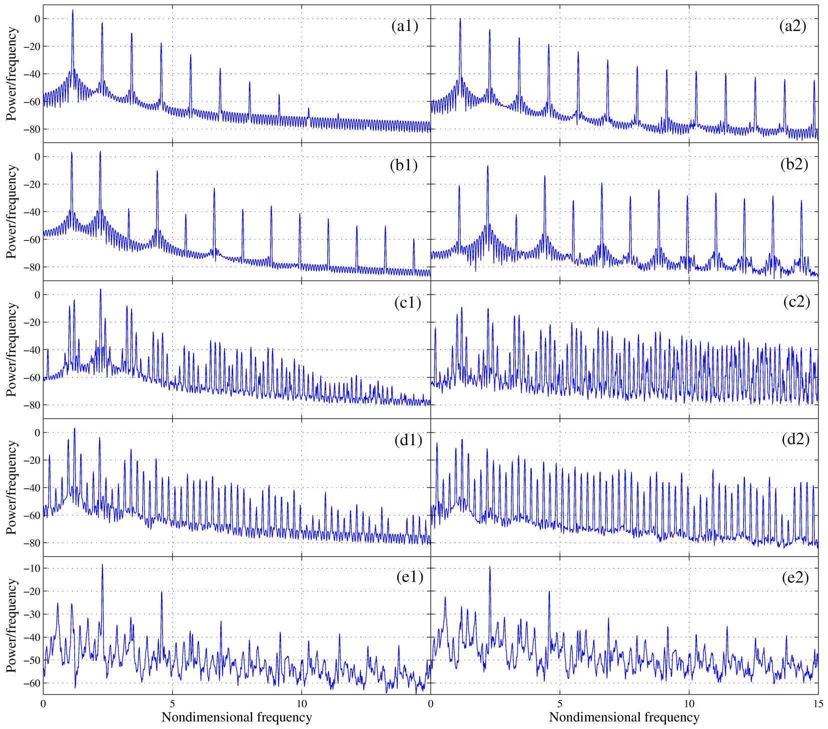

Figure 5.6: Power spectra of velocity (labelled 1) and heat release rate (labelled 2) for the different types of oscillation corresponding to different flame positions of figure 5.1: (a) period-*1* oscillation at $x_f = 0.45$, (b) period-*2* oscillation at $x_f = 0.3$, (c) quasi-periodic oscillation at $x_f = 0.4$, (d) period-*5* oscillation at $x_f = 0.286$ and (e) chaotic oscillation at $x_f = 0.046$.

two frequencies arise due to nonlinear interactions between the two independent frequencies. Figure 5.6(e) shows that spectra of chaotic oscillations are generally broadband with peaks at frequencies that are close to some of the acoustic frequencies of the duct.

5.4.3 Phase space reconstruction and Poincaré sections

A phase space diagram is reconstructed from the time series using the methods described in §5.2.2. As mentioned in §5.2.2, the first zero-crossing of the auto-correlation function was used to find an optimal time delay and Taken's embedding theorem was used to to reconstruct the phase space. Three embedding dimensions were sufficient to represent the dynamics of the system. Figure 5.7

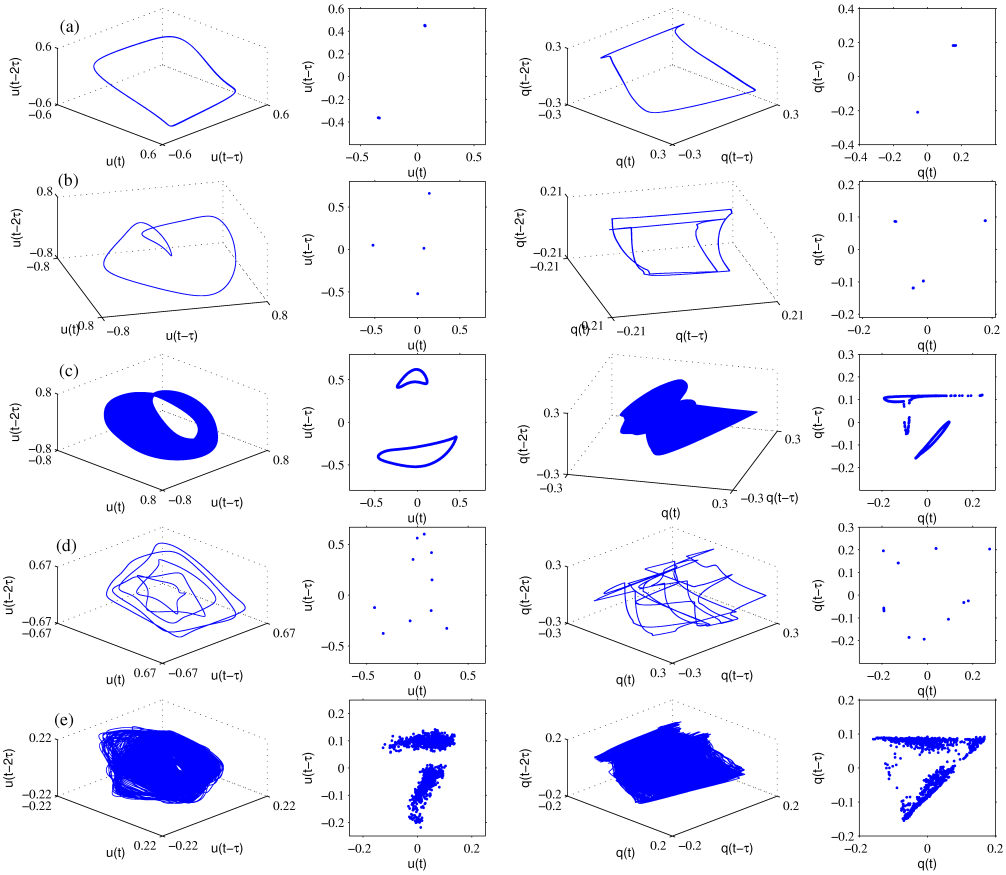

Figure 5.7: Phase portraits and Poincaré sections of velocity and heat release rate for the different types of oscillation corresponding to different flame positions of figure 5.1: (a) period-*1* limit cycle oscillation at $x_f = 0.45$, (b) period-*2* oscillation at $x_f = 0.3$, (c) quasi-periodic oscillation at $x_f = 0.4$, (d) frequency-locked oscillation at $x_f = 0.286$ and (e) chaotic oscillation at $x_f = 0.046$.

shows the phase portraits and Poincaré sections of the velocity (on the left) and heat release rate (on the right) for the oscillations in figures 5.5 and 5.6.

Figure 5.7 shows that periodic oscillations (or limit cycles), *i.e.* subfigures (a), (b) and (d), are closed loops in phase space. A period-*1* oscillation, subfigure (a), is a single loop, a period-*2* oscillation, subfigure (b), is a double loop and a period-k oscillation, subfigure (d), is a k-loop where k is the least common integer multiple of the two commensurate frequencies that characterise the oscillation. Their corresponding Poincaré sections, which are planes perpendicular to the attractors in phase space, have two points, four points or $2k$ points. Figure 5.7(c) shows that quasi-periodic oscillations are tori in phase space: in this case 2-tori because the oscillations have two incommensurate frequencies. On a quasi-periodic attractor, the torus is ergodic. Figure 5.7(e) shows that chaotic oscillations fill an entire volume in phase space and an area in the Poincaré section, because the corresponding strange attractors are highly folded fractal structures. This type of oscillation is characterized more precisely using correlation dimensions, which are described next.

Phase portraits and Poincaré sections represent the different types of oscillation distinctly. They are more useful than simply examining time series or power spectra because the well-defined topological structure of attractors can be used to obtain quantitative information about the nonlinear behaviour of the system, even in the case of noisy experimental data [65].

5.4.4 Correlation dimensions

As mentioned in §5.2.2, the correlation dimension measures the number of active degrees of freedom in a dynamical system and is used to determine the nature of an attractor. We use the algorithm of Grassberger & Procaccia [157] implemented in the online package TISEAN by Hegger *et al.* [152], with up to 7 embedding dimensions. Figure 5.8 shows the correlation sum (left column) and its local slope (middle column) as functions of the Euclidean distance in phase space. On the right column is the correlation dimension defined as the average slope over the range of radii where the slope remains approximately constant, as a function of the embedding dimension. For periodic oscillations (a, b and d), the correlation dimension and hence the number of active degrees of freedom is 1. For quasi-periodic oscillations (c) it is 2 and for chaotic oscillations (e) it is not an integer, in this case 1.7 ± 0.15.

The self-similar scaling region over which the correlation dimension is determined may be small when the correlation sum is a strong function of the magnification, as in case (e) where the average is found over $0.1 < {}^{R}\!/_{R_{max}} < 0.6$ [88]. In figures 5.8 (a) through (d), however, self-similar scaling regions exist over almost two orders of magnitude and these ranges are used to determine the

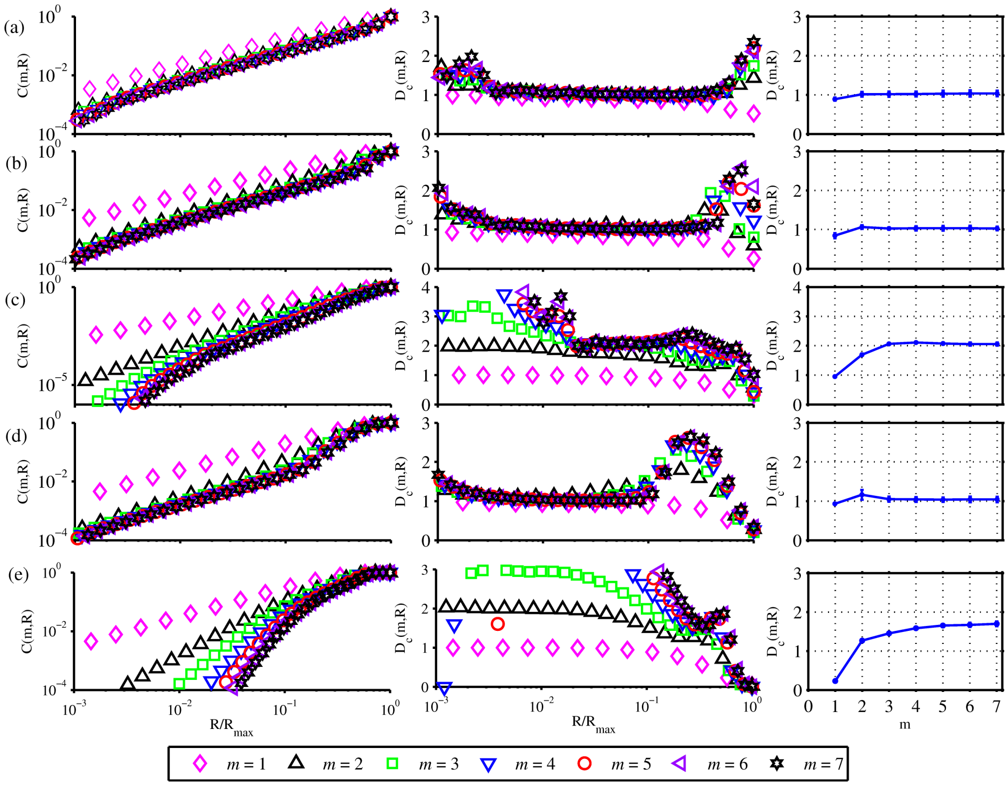

Figure 5.8: This figure shows the correlation sum, $C(m, R)$ (left column), and its local slope, $D_c(m, R) = \partial \text{log} C(m, R)/\partial \text{log} R$ (middle column), as functions of the Euclidean distance, R/R_{max}, for an embedding dimension up to $m = 7$. Shown in the right column is the correlation dimension defined as the average slope $(\overline{D_c(m, R)} = \overline{\partial \text{log} C(m, R)/\partial \text{log} R})$, over the range of radii where the slope remains fairly constant, as a function of the embedding dimension, m. (a) through (e) correspond to period-*1*, period-*2*, quasi-periodic, frequency-locked and chaotic oscillations of figure 5.5.

correlation dimensions. The local slope of the correlation sum does not converge at very small or very large scales, indicating an absence of self-similarity at these scales. This is because, at very small scales, the dynamics are dominated by noise and, at very large scales, the self-similarity is disrupted by the finite scale of the attractor, which acts as a macroscopic cutoff filter [151].

5.5 The role of unstable attractors

Trajectories in the neighbourhood of unstable attractors are attracted towards them in some directions but repelled in others [150]. Unstable solutions divide the phase space into basins of attraction. Identifying the unstable attractors of a dynamical system helps predict the mechanisms or pathways for a system to transition from one attractor to another. They are especially useful in noise-induced transition mechanisms such as triggering, as shown by Waugh *et al.* [58].

The advantage of this numerical approach is that we can see how the system passes in the vicinity of unstable attractors as it moves towards a stable attractor. This has been shown in thermoacoustics only for an unstable period-*1* attractor [50]. It has not been shown, however, for more elaborate unstable attractors. It is, however, well known in hydrodynamics [160]. Figures 5.9 and 5.10 show the time series, phase portraits and Poincaré sections, starting from the steady base state evolving to the ultimate stable state, via intermediate states. These intermediate states lie in the neighbourhood of the unstable attractors of the system.

The phase portraits and Poincaré sections are used to identify these unstable attractors. In figure 5.9(a), the system is first attracted towards an unstable period-*1* limit cycle (red) and then repelled from it towards a stable period-*1* limit cycle of larger amplitude (blue). In (b) the system is attracted towards an unstable period-*1* limit cycle on the same branch of unstable limit cycles as in (a), then it is repelled from it and attracted towards a second unstable quasi-periodic period state, then it is repelled from this state and ultimately it tends towards another stable quasi-periodic state. In (c) the system is strongly attracted from its steady base state towards a quasi-periodic state (red) and then repelled from it and finally tends towards a stable period-*1* limit cycle. In (d) the system is attracted towards an unstable period-*1* limit cycle (red) of large amplitude before it is repelled from it towards its ultimate quasi-periodic state.

In figure 5.10(a) there exist 2 intermediate unstable states. The first one is quasi-periodic (red), the second one is a period-*1* limit cycle (green), and the third state is a period-*2* limit cycle (blue). In (b) through (d) some of the intermediate states are chaotic.

These figures show clearly that the system has several unstable attractors.

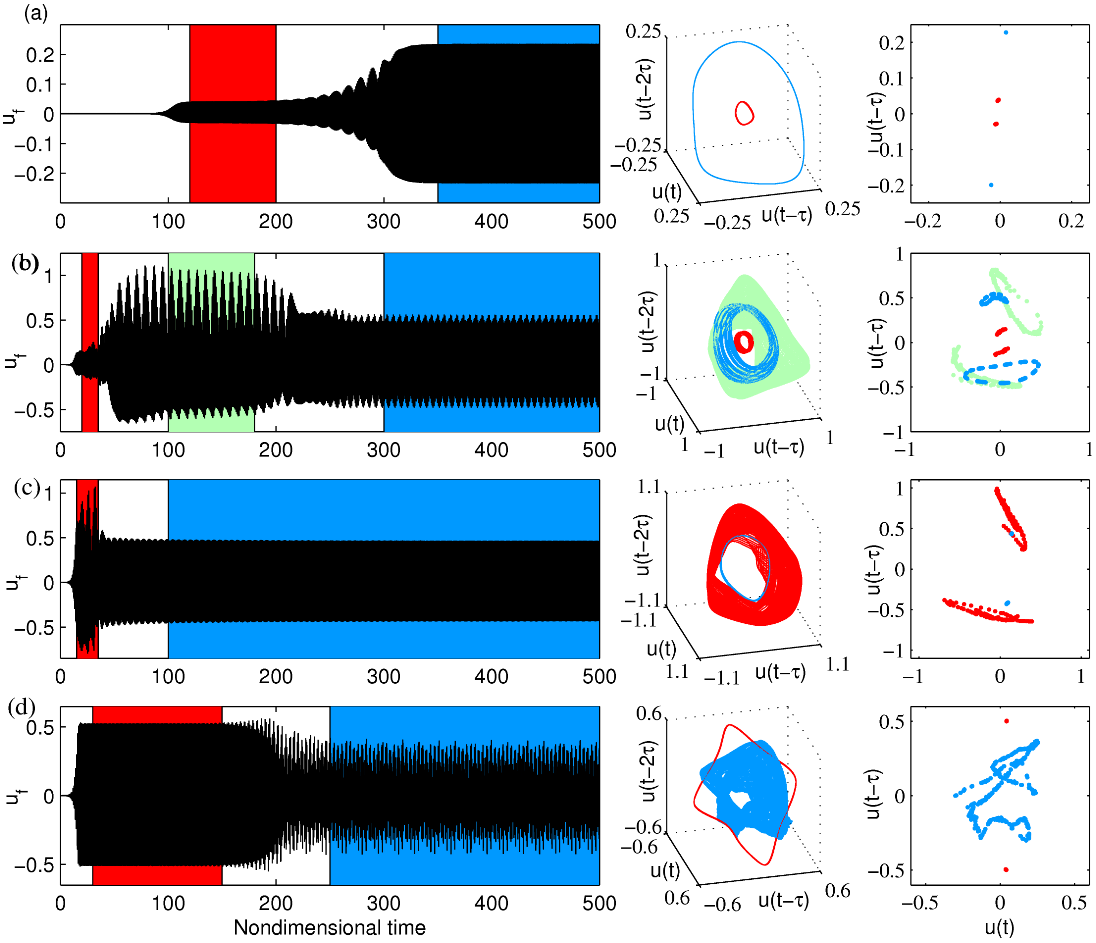

Figure 5.9: The time series, phase portraits and Poincaré sections of trajectories starting from the steady base state to the ultimate stable state with one or more intermediate states: (a) $x_f = 0.480$, (b) $x_f = 0.420$, (c) $x_f = 0.347$ and (d) $x_f = 0.2651$. For (a) to (c) $L_f/ML_0 = 2.2$ and for (e) $L_f/ML_0 = 2.0$. The windows of the time series that are used to extract the phase portraits are shown as coloured patches. Intermediate states are shown in red and green, and the final stable state is shown in blue.

This makes the trajectory of the system elaborate. Such elaborate behaviour has recently been observed in plane Couette flow [161]. Gibson *et al.* (2009) mention that once a system's invariant solutions have been determined, the next step is to determine how the system dynamics interconnects the neighbourhoods of these invariant solutions. The unstable attractors of a system play a pivotal role in

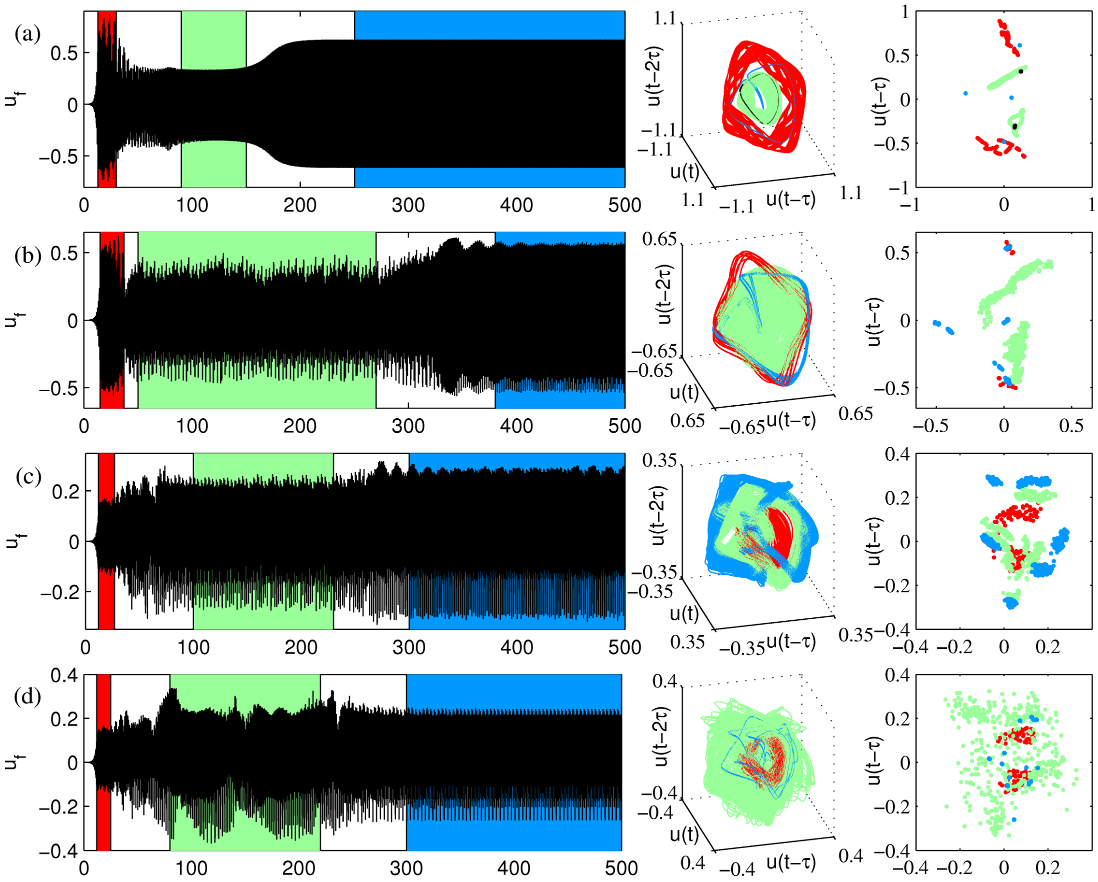

Figure 5.10: A continuation of the previous figure, this figure also shows the intermediate states in the time evolution of the self-excited system: (a) $x_f = 0.295$, $L_f/ML_0 = 2.2$, (b) $x_f = 0.2862$, $L_f/ML_0 = 2.0$, (c) $x_f = 0.066$, $L_f/ML_0 = 2.2$, and (d) $x_f = 0.063$, $L_f/ML_0 = 2.2$.

these interconnections.

5.6 Routes to Chaos

If a nonlinear system exhibits chaotic dynamics it is natural to ask how this chaotic behaviour emerges as a parameter is varied. By the early 1980s three routes to chaos in nonlinear dynamical systems had been discovered: period doubling, Ruelle-Takens-Newhouse and intermittency [162]. Since then several more routes have been discovered [163]. We have identified two routes to chaos in this study: the period-doubling and the Ruelle-Takens-Newhouse routes.

5.6.1 Period-doubling

Feigenbaum in 1978 discovered a route to chaos via a cascade of period doubling bifurcations and identified a self-similar structure of the bifurcation diagram [164]. Period doubling transitions have been observed in electrical circuits, population dynamics and convective flows, for example in experiments on Rayleigh-Bénard convection [165; 166].

Figure 5.11 shows the period doubling cascade as the flame position is changed. On the left is the bifurcation diagram and on the right are the power spectra at the flame location just after each period doubling bifurcation. The first period doubling bifurcation from period-1 to period-2 oscillations is subcritical (the unstable branch is not shown here). The arrows at $x_f = 0.308$ show that the transition to period-*2* oscillations is abrupt. The subsequent bifurcations occur at $x_f = 0.301$ (period 2 to 4) and $x_f = 0.296$ (period 4 to 8) and are supercritical. The power spectra on the right show the introduction of the first subharmonic of the lowest frequency at each period-doubling bifurcation, ultimately leading to chaotic oscillations with a broadband spectrum and a few peaks at $x_f = 0.2861$. The length of the time series used to obtain these spectra is 300 nondimensional units, therefore the subharmonics below $^f/_8$ were not well-resolved. Furthermore, the lengths along the parameter axis (x-axis) between subsequent period-doubling bifurcations decreases rapidly, and this makes resolving higher period-2^k bifurcations difficult. The characteristics of the strange attractor at $x_f = 0.2861$ will be

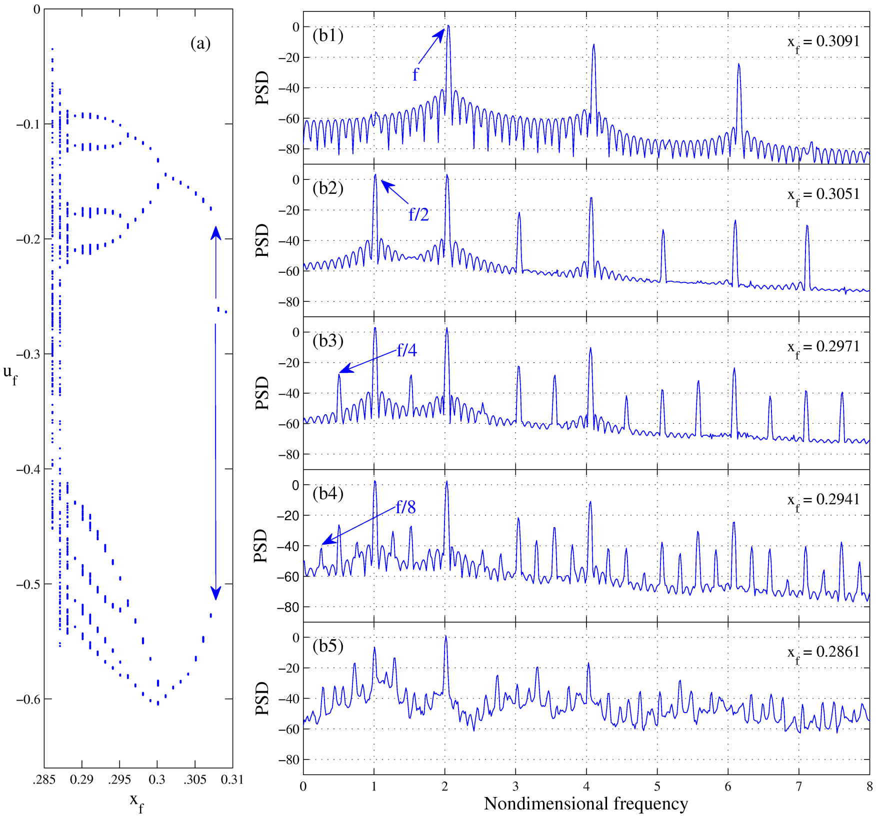

Figure 5.11: The period doubling route to chaos observed in the x_f range of 0.285 to 0.31 ($^{L_f}/_{ML_0} = 2.0$) (a) Bifurcation diagram constructed using the troughs of the time series of velocity perturbations at the flame position, u_f. A series of period doubling bifurcations occur at $x_f = 0.307$ (period 1 to 2), $x_f = 0.301$ (period 2 to 4) and $x_f = 0.296$ (period 4 to 8). (b) Power spectra of velocity at the flame showing the emergence of subharmonics ($^{f}/_{2}$ (figure (b2)), $^{f}/_{4}$ (figure (b3)), $^{f}/_{8}$ (figure (b4))) at the above mentioned values of x_f, finally leading to chaotic oscillations at $x_f = 0.288$ (figure (b5)).

discussed in §5.6.3.

5.6.2 Ruelle-Takens-Newhouse

Ruelle and Takens proposed a theory in 1971 that challenged the mechanism of turbulence generation proposed by Landau, which required an infinite number of Hopf bifurcations [167]. This mechanism was improved and came to be known as the Ruelle-Takens-Newhouse route to chaos [149; 168]. They proved that three successive Hopf bifurcations, producing three independent frequencies, generates a 3-torus that can become unstable and be replaced by a strange attractor [162]. The time-dependent behaviour is not quasi-periodic with three frequencies, but is distinctly chaotic. They, however, did not predict how and when the strange attractor close to the 3-torus comes into being. Sometimes the 3-torus can lead to a frequency-locked periodic state before the transition to chaos. The exact sequence of steps in this route is still debated [61]. The Ruelle-Takens-Newhouse route, however, is similar to but not the same as another route to chaos directly from a 2-torus to a frequency-locked state to chaos, without a third frequency, called the phase-locked transition [149].

The Ruelle-Takens-Newhouse route to chaos has been observed in hydrodynamic systems: Rayleigh-Bénard convection [165; 169], circular Couette flow [170; 171] and direct numerical simulations of converging-diverging channel flow [172; 173]. Recently this has also been observed in experiments in thermoacoustics by Kabiraj *et al.* [64].

Figure 5.12 shows the Ruelle-Takens-Newhouse route as the natural acoustic frequency of the duct, ${}^{L_f}/_{ML_0}$, is changed by varying the length of duct, L_0. The Poincaré sections show that the quasi-periodic state (2-torus) in figure 5.12(a) develops corrugations on its surface (figures 5.12(c), (d), (e) and (f)) as it undergoes a secondary Hopf bifurcation to a 3-torus. The wrinkling of the surface of the attractor followed by the breakdown of the torus (figures 5.12(g), (h) and (i)) is characteristic of the two-fold operation of stretching and folding that ultimately leads to a strange attractor [149]. The states shown in Fig 5.12 (k) and (l) are chaotic. The power spectra of acoustic velocity at the flame position in figure 5.13 show the emergence of a third frequency (figures 5.13(f), (g) and (h)) that is

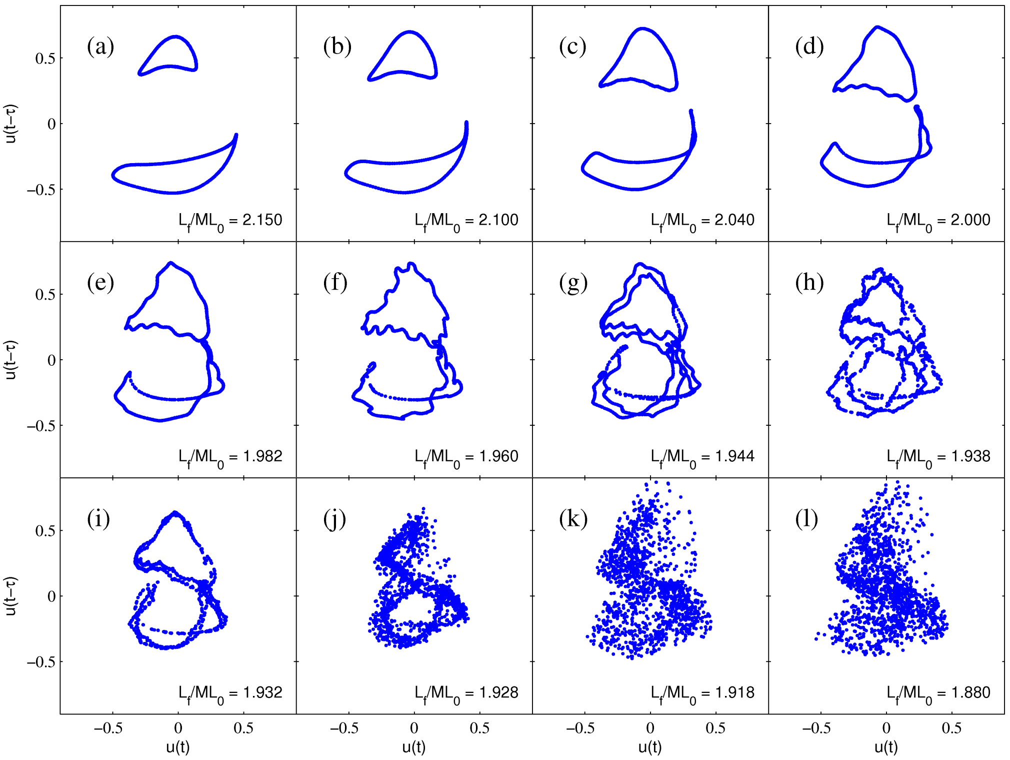

Figure 5.12: The Ruelle-Takens-Newhouse route to chaos observed in the $^{L_f}/_{ML_0}$ range of 1.88 to 2.15 ($x_f = 0.4$). (a) through (l) show the Poincaré sections of phase portraits of the final state of the system at each operating point (varying $^{L_f}/_{ML_0}$). The stable quasi-periodic state (2-torus) in (a) develops corrugations on its surface due to stretching and folding (see sub-figures (c), (d), (e) and (f)). This is followed by torus breakdown (see sub-figures (g), (h) and (i)) to chaos (sub-figures (j), (k), (l)).

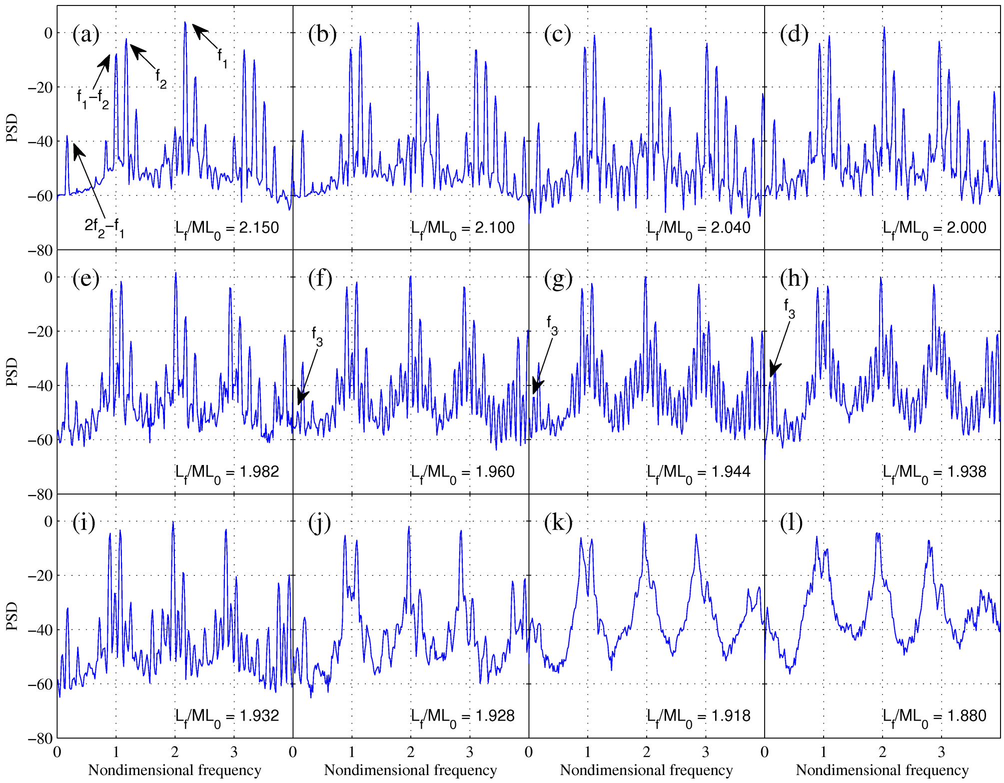

Figure 5.13: The Ruelle-Takens-Newhouse route to chaos observed in the $^{L_f}/_{ML_0}$ range of 1.88 to 2.15 ($x_f = 0.4$). (a) through (l) show the power spectra of the velocity at the flame position for these states (corresponding to the same subfigures in figure 5.12. This route to chaos is characterised by the emergence of a third frequency (marked f_3 in (f), (g) and (h)) that is incommensurate with the two frequencies of the quasi-periodic state (marked f_1 and f_2 in (a)).

incommensurate with the two frequencies of the quasi-periodic state (marked f_1 and f_2 in figure 5.13(a)). This is a characteristic of the Ruelle-Takens-Newhouse route to chaos. Note that the emergence of f_3 is simultaneously accompanied by the emergence of linear combinations of f_1, f_2 and f_3 (for example, note the new peak at nondimensional frequency unity in (e), (f), (g) and (h), which is absent in (a), (b), (c) and (d)). Without sufficient evidence the 'true' f_3 cannot be determined. Further investigation into the physics of the problem may shed light on this aspect.

5.6.3 Characterizing chaos

As mentioned in §5.2.2, chaotic oscillations are characterized by non-integer correlation dimensions and positive maximal Lyapunov exponents.

Figure 5.14 shows the correlation sum and its local slope as functions of the Euclidean distance, and the correlation dimension as a function of embedding dimension, for chaotic oscillations: (a) at the end of the period-doubling cascade (figure 5.11(b5)) and (b) at the end of Ruelle-Takens-Newhouse route to chaos (figure 5.12(l)). The correlation dimension in (a) is 2.7 ± 0.2 and in (b) is 3.6 ± 0.15, which are not integers. Therefore the oscillations are chaotic. Non-integer dimensions represent geometrical objects that show structure on all scales and quantifies the self-similarity of strange attractors [151].

Figure 5.15 shows the average divergence of trajectories of neighbouring points in phase space as a function of temporal separation. This is found using the algorithm by Kantz [158] and available online in the TISEAN package [152]. For reliable convergence we use up to 8 embedding dimensions. In both figures 5.15 (a) and (b) a linear trend is seen at temporal separation between 1 and 7, and the dashed line shows a linear fit to this trend. The slope of the linear fit gives the maximal Lyapunov exponent, which is 0.078 ± 0.03 in (a) and 0.15 ± 0.01 in (b). Note that these values are small because the non-dimensional temporal separation is used in the calculation. For a system with fundamental acoustic frequency at $100Hz$ the corresponding dimensionalised values for the Lyapunov exponents are $2.57{\pm}0.97\ sec^{-1}$ in (a) and $4.95{\pm}0.33\ sec^{-1}$ in (b). The exponent is positive in both cases confirming that the oscillations are chaotic. All motions on

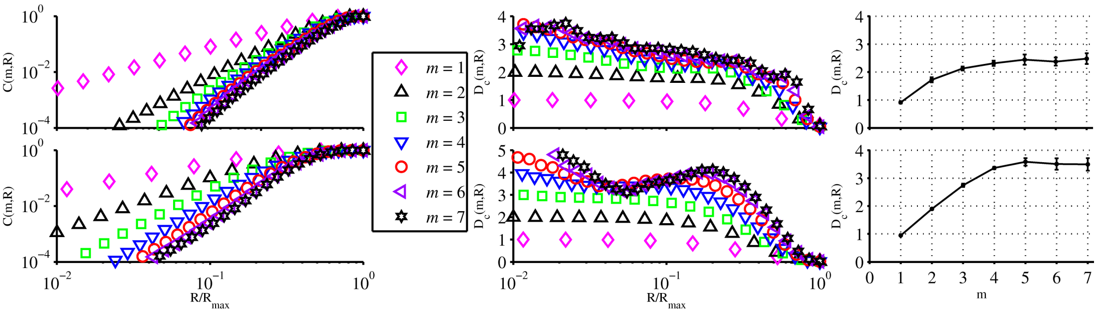

Figure 5.14: This figure shows the correlation sum, $C(m, R)$ (left column), and its local slope, $D_c(m, R) = \partial \log C(m, R)/\partial \log R$ (middle column), as functions of the Euclidean distance, R/R_{max}, for an embedding dimension up to $m = 7$. Shown in the right column is the correlation dimension defined as the average slope $(\overline{D_c(m, R)} = \overline{\partial \log C(m, R)/\partial \log R})$, over the range of radii where the slope remains fairly constant, as a function of the embedding dimension, m. (a) chaotic oscillations in the period-doubling route to chaos, figure 5.11(b5) (b) chaotic oscillations in the Ruelle-Takens-Newhouse route to chaos, figure 5.12(l).

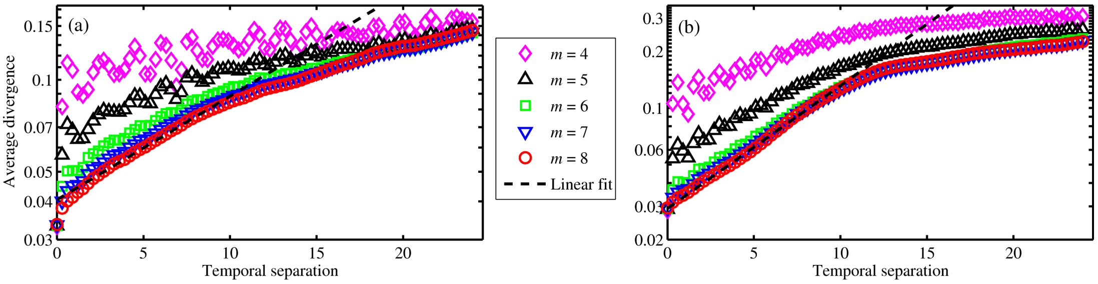

Figure 5.15: This figure shows the average divergence of trajectories, $S(\Delta n)$ as a function of temporal separation for an embedding dimension up to $m = 8$ for the chaotic oscillations in (a) the period-doubling route to chaos, figure 5.11(b5) and (b) the Ruelle-Takens-Newhouse route to chaos, figure 5.12(l). The local slope of the linear region gives the maximal Lyapunov exponent and this is shown as a dashed line

a strange attractor are unstable. The maximal Lyapunov exponent measures the instability of chaotic solutions, *i.e.* rate of divergence of neigbouring trajectories in the strange attractor [151]. Hence it measures the 'strength of chaos'.

5.7 Instantaneous flame images

Figure 5.16 shows images of the flame during different types of oscillation: (a) period-*1*, (b) period-*2* (c) quasiperiodic (d) frequency-locked and (e) chaotic. 15 temporally equispaced images are shown for each case, spanning 3 cycles of the dominant frequency. In (a) the snapshots 1-5, 6-10 and 11-15 are identical, showing that the oscillation is period-*1*. In (b) the snapshots 1-5 and 6-10 differ. In the first cycle cusps are sharper and the pocket that pinches off is larger than in the second. But 11-15 are the same as 1-5 because these oscillations are period-*2*. In (c) each cycle is similar but not identical and a gradual shift in flame shapes can be seen across 1-5, 6-10 and 11-15, which shows a low frequency modulation of the dominant mode of oscillation. In (d) the behaviour is similar to the quasiperiodic case in (c), but the low frequency modulation is at exactly one-fifth of the dominant frequency, therefore the cycle repeats itself after every 25 snapshots (not shown here). In (e) the oscillations are chaotic and the cycles never repeat themselves; the cusps on the flame surface are of different shapes and sizes and pinch off does not occur at regular intervals. However, the flame shapes have the same features as in the previous cases, namely, cusp formation and pinch-off. These images show that while the basic flame dynamics, such as cusp formation, advection of wrinkles along the flame and pinch-off at the tip, remain the same in all cases, clear differences exist in the shape of the cusps and the instants when they are formed at the base of the flame. This is because the acoustic velocity at the flame position, which creates wrinkles by perturbing the base of the flame, are subtly different for different types of oscillation due to the higher modes. For example, in the period-*2* case, the acoustic velocity perturbation in one cycle has a smaller amplitude than in the other, therefore the cusp formed on the flame surface and the pocket that pinches off in the first cycle is smaller than the corresponding features in the second cycle. This shows that the nonlinear behaviour of the flame depends very sensitively on the way

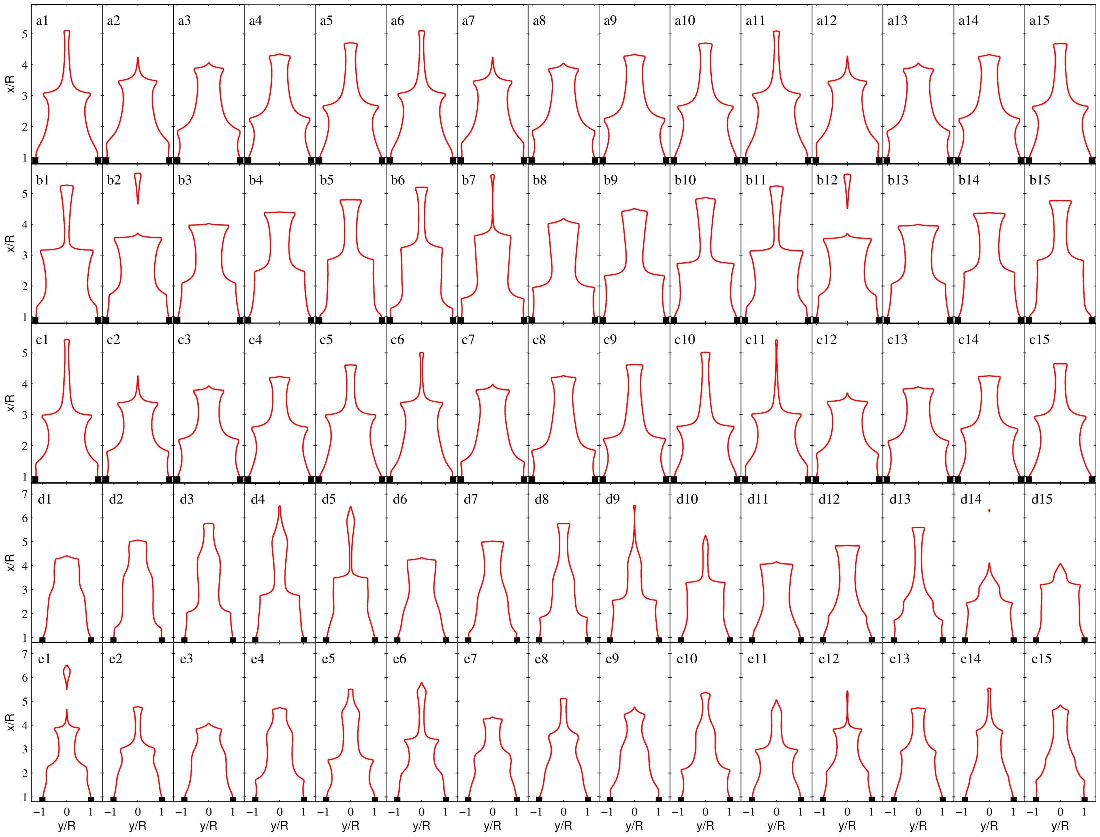

Figure 5.16: Instantaneous flame images of the self-excited flame for different types of oscillation: (a) period-*1* oscillation at $x_f = 0.435$ (mode-2 branch) (b) period-*2* oscillation at $x_f = 0.3$, (c) quasi-periodic oscillation at $x_f = 0.4$, (d) frequency-locked oscillation at $x_f = 0.286$ and (e) chaotic oscillation at $x_f = 0.4$. For (a) through (d) all other parameters are the same as in figure 5.5, while (e) has the same parameters as figure 5.8(e). 15 images are shown for each case spanning 3 cycles of the dominant frequency.

the flame surface deforms (because the flame surface deformation greatly affects the heat release rate), which in turn depends very sensitively on the velocity perturbation at the inlet plane.

These flame images are similar to those seen in experiments, but lack the rounding off due to flame curvature and stretch effects [65]. The effect of flame curvature has been included in recent work by Waugh [60]. In their experiments, Kabiraj *et al.* have observed intermittency due to repeated flame lift-off and reattachment [65]. Such behaviour cannot be captured in this model because our flame remains attached to the burner at all times. We leave incorporating flame lift-off into our model for future work.

5.8 Conclusions

In this study a reduced order model of a ducted premixed flame is simulated and analysed using techniques from nonlinear time series analysis and dynamical systems theory.

The bifurcations of this system for three control parameters are examined: (i) the flame position in the duct, (ii) the flame aspect ratio, and (iii) the length of duct. Depending on the flame position in the duct, the system has not only period-*1* oscillations but also period-*2*, period-k, quasi-periodic and chaotic oscillations. The transitions to these types of oscillation are via Hopf, Neimark-Sacker and period-doubling bifurcations. Some of these bifurcations are subcritical, so the state that the system reaches changes abruptly even with a smooth change in the control parameter. In certain regions of control parameter space, more than one stable state exists and the state reached depends on the initial conditions. Therefore there is hysteresis and mode switching is possible. Varying the flame aspect ratio shows that chaotic oscillations are more likely in systems with short flames than with long flames because they have sharper cusps at lower amplitudes of oscillation. Varying the duct length shows that quasiperiodic and chaotic oscillations are more likely in systems with long ducts, whereas period-*1* limit cycles are more likely in systems with short ducts. This is because short ducts have high natural acoustic frequencies and their higher acoustic modes are strongly damped. This shows that parameters that affect either the flame or the acoustics can influence the system's nonlinear behaviour.

The influence of the number of coupled acoustic modes on the bifurcations and nonlinear behaviour of the system is analysed. It is shown that when there is only one mode in the acoustics, which is equivalent to the flame describing function approach in the frequency domain, the system is either stable or has period-*1* oscillations. Furthermore, the oscillation amplitude is underpredicted in large regions of parameter space and the bifurcations and multi-stability seen in the multi-modal case are not captured. The heat release rate is highly nonlinear but, because the acoustic velocity and pressure are assumed to be harmonic, the higher and sub-harmonics of the heat release rate cannot interact with acoustics. The multi-modal simulations show rich behaviour because (i) the highly nonlinear unsteady heat release rate can excite several modes simultaneously, which results in nonharmonic velocity perturbations that, in turn, cause elaborate flame wrinkling and (ii) more than one mode may be linearly unstable and the energy transfer between them due to nonlinear interactions affects the transient and steady state behaviour of the system.

The transient and steady state behaviours of the system are analysed using power spectra of time series, phase portraits reconstructed from time series, Poincaré sections of phase portraits and by calculating correlation dimensions of the different attractors of the system. They show that the trajectory of the system from the steady base state to its ultimate oscillatory state is elaborate and involves transient attraction and repulsion by one or more unstable attractors before the system tends towards a stable state. Therefore the unstable attractors strongly influence the system's pathways.

Bifurcation diagrams and Poincaré sections are used to establish two routes to chaos in this system: the period-doubling route and the Ruelle-Takens-Newhouse route and these are corroborated by analyses of the power spectra of the acoustic velocity. The system tends towards strange attractors via these routes and these attractors are characterised by computing their correlation dimensions and maximal Lyapunov exponents. These routes to chaos have been observed in experiments on a similar thermoacoustic system [64].

Instantaneous flame images reveal that the wrinkles on the flame surface and pinch off of flame pockets are regular for periodic oscillations, while they are irregular and have multiple time and length scales for aperiodic oscillations. This is because the magnitude and shape of the acoustic velocity at the flame position, which creates wrinkles by perturbing the flame surface, are different for different types of oscillation. For example, in the period-*2* case, the acoustic velocity perturbation in one cycle has a smaller amplitude than in the other, therefore the cusp formed on the flame surface and the pocket that pinches off in the first cycle is smaller than the corresponding features in the second cycle. The source of nonlinearity is the flame, but such nonharmonic velocity waveforms are possible because the acoustics responds at several frequencies.

Our model captures this behaviour because it consists of several coupled nonlinear oscillators that are simultaneously excited by a highly nonlinear unsteady heat release rate from a realistic flame model. This study complements recent experiments on a ducted laminar premixed flame through the detailed analysis of a reduced order model of a similar system, with approximately 5000 degrees of freedom, that behaves qualitatively similarly.

The methods from dynamical systems theory illustrated in this study are superior to both frequency domain approaches commonly used in nonlinear thermoacoustics, and time domain approaches with simple flame models used in previous studies. This system behaves similarly to low-dimensional chaotic dynamical systems and several techniques from nonlinear time series analyses and dynamical systems theory have proved useful in characterizing and interpreting its behaviour. Time series analysis is computationally expensive because it requires simulations that contain many cycles. It is a powerful way, however, to obtain quantitative information about aperiodic oscillations. Applying continuation analysis is a fast and efficient way to find periodic oscillations and their bifurcations over a large parameter space relatively quickly. This has been shown to be successful for this system in recent work by Waugh [60].

Chapter 6

Nonlinear oscillations in a self-excited thermoacoustic system: the influence of external forcing

Summary

In this chapter we examine the response of a self-excited ducted premixed flame to imposed acoustic velocity forcing. The phenomenon of synchronization is well known as a universal concept in nonlinear science but has received little attention in the field of thermoacoustics. This study aims to identify synchronization phenomena in thermoacoustics within the framework of nonlinear dynamics. Open-loop control of oscillations in nonlinear systems using weak periodic perturbations has been proven to be successful. This study aims to explore the possibility of similar applications in thermoacoustics.

In chapter-5 we have shown that a ducted premixed flame exhibits elaborate nonlinear behaviour. We examine the response of this system to harmonic forcing for three types of self-excited oscillation: (i) periodic, (ii) quasi-periodic and (iii) chaotic. Acoustic velocity forcing is applied at the lip of the burner (from a loudspeaker, for example) and the response of the system is measured in the pressure *fluctuations at a particular location in the duct.*

When the self-excited system oscillating periodically is forced, we find that: (i) at low forcing amplitudes, the system responds at both the natural and forced frequencies and linear combinations of these frequencies, indicating quasiperiodicity and nonlinear interactions between the forced and self-excited modes; (ii) above a critical forcing amplitude, the system locks-in to the external forcing, irrespective of the forcing frequency; (iii) the bifurcations leading up to lock-in and the critical forcing amplitude required for lock-in depend on the proximity of the forcing frequency to the natural unforced frequency; (iv) the amplitude of self-excited oscillations at lock-in may be higher or lower than the unforced state, depending on the forcing frequency; and (v) beyond lock-in, if the system is forced at increasingly larger amplitudes, the periodic oscillation in the system can become unstable and transition to chaos, or repeatedly switch between different stable attractors.

When the self-excited system oscillating quasi-periodically is forced, we find that (i) if the forcing frequency is the same as one of the two characteristic frequencies of the torus attractor, then lock-in occurs at a critical amplitude via a saddle-node bifurcation; (ii) if the forcing frequency is not equal to either of the two characteristic frequencies of the torus attractor, then the torus breaks down and more elaborate behaviour is noticed.

When the self-excited system oscillating chaotically is forced close to the most dominant frequency in its spectrum, we find that it is possible to destroy chaos and establish a stable periodic oscillation.

Finally, we find that in some cases low-amplitude forcing can achieve lock-in and the amplitude of oscillations in the system are decreased by up to 80% of the unforced amplitude. Therefore, low-amplitude acoustic forcing at carefully-chosen frequencies may be an effective way for suppression of self-excited thermoacoustic systems.

6.1 Introduction

Self-excited nonlinear systems exhibit synchronization, the phenomenon in which a system changes its frequency due to external forcing or by interacting with another nonlinear oscillator. Synchronization has been observed and investigated in several natural and man-made systems including pendulum clocks, chemical reactions, radio waves, neurons and organ pipes [89; 174; 175; 176]. Lock-in or entrainment by an external force is a well-known type of synchronization and has been studied extensively [177]. The dynamics of low-dimensional dynamical systems under external forcing such as the forced van der Pol oscillator is well-understood [178] and has been used as a canonical model for various forced nonlinear systems including hydrodynamically self-excited flows [88; 179] and circadian oscillations [180]. Suppressing spontaneous nonlinear oscillations by applying external forcing has been studied extensively because of its applicability in wide-ranging fields from control of flow oscillations to control of oscillations in neural systems [181]. These studies have led to the development of strategies for open-loop control of periodic and chaotic oscillations in various nonlinear systems using weak external forcing [90; 182].

Passive control, feedback control, model-based control and adaptive control of thermoacoustics has been studied extensively [1; 5]. For example, harmonic forcing of the fuel flow rate at the same frequency as the self-excited mode, but out of phase with it, has been employed as a strategy for feedback control of thermoacoustic oscillations [183]. Recently, more sophisticated strategies have been developed using model-based control [7; 184] and adaptive feedback control of thermoacoustic oscillations [185].

Open-loop control strategies, however, have not been studied extensively. Bellows *et al.* experimentally investigated the effectiveness of open-loop harmonic forcing as a means of suppression of thermoacoustic oscillations [43]. Bellows *et al.* also examined some aspects of the nonlinear interactions between acoustic forcing and self-excited thermoacoustic oscillations in the same study. They found that the self-excited oscillations of their lean, premixed swirl-stabilized combustor are entrained by external acoustic forcing of sufficiently large amplitude. They also found that the overall acoustic power was substantially reduced due to the external forcing at some operating points. However, they did not notice an appreciable effect on the behaviour of the system for low amplitude forcing ($^{u'}/_{U_0} < 10\%$), most likely because of two reasons: (i) the significant noise levels in their large-scale turbulent combustor, and (ii) their choice of forcing frequencies that were far away from the natural frequency of the system. Furthermore, they mention that the hydrodynamic instabilities excited by external forcing complicate the response of their system to forcing. Therefore, due to the complexity of their system, only few conclusions were drawn.

Studies in nonlinear dynamics and synchronization [89] and recent experiments in a self-excited hydrodynamic system [88] have shown that nonlinear systems exhibit rich nonlinear behaviour before lock-in and beyond lock-in. This rich dynamics and the specific bifurcations leading up to lock-in have not been investigated in thermoacoustics.

Many thermoacoustic systems tend to have self-excited oscillations at discrete frequencies [10]. Recent studies have shown, however, that this is not always the case and even a simple thermoacoustic system of a ducted premixed flame exhibits elaborate nonlinear dynamical behaviour including quasi-periodicity, intermittency, chaos and multi-stability [56; 64; 65]. In chapter-5 we have shown that our numerical model also exhibits similar behaviour. The effect of external acoustic forcing on such elaborate nonlinear behaviour in thermoacoustic systems has not been studied. Dynamical systems theory, however, has been used extensively to study synchronization in nonlinear systems and provides a suitable framework to investigate this problem in thermoacoustics.

Intrigued by the rich dynamical behaviour in the synchronization of nonlinear systems and motivated by the success of open-loop forcing in suppressing self-excited oscillations, we explore the influence of external (open-loop) acoustic forcing on a simple thermoacoustic system. We use the coupled dynamical model described in previous chapters because (i) this system captures the elaborate nonlinear behaviour seen in experiments, (ii) this 5000 degree of freedom system is significantly smaller than CFD, and therefore can be simulated relatively quickly, and (iii) it is a relatively simple model of a few coupled nonlinear oscillators, for which there exist low-dimensional chaotic analogues in the literature of synchronization [89].

The aims of this study are: (i) to investigate the influence of external harmonic forcing on self-excited periodic, quasi-periodic and chaotic thermoacoustic oscillations; (ii) to characterize the dynamics leading up to lock-in; and (ii) to explore the possibility of using weak periodic perturbations for suppression of thermoacoustic oscillations. In §6.3 we briefly discuss the dynamics of the unforced self-excited system. In §6.4 we discuss the influence of forcing above and below the natural self-excited frequency of a limit cycle oscillations, at various amplitudes. In §6.4.2 we construct a lock-in diagram, examine its asymmetries and discuss its implications for the suppression of period-*1* oscillations in thermoacoustic systems. In §6.7 we discuss the influence of forcing on self-excited aperiodic oscillations. Finally, we draw some conclusions in §6.8.

6.2 Models and methods

The model used in this chapter is the same as that in chapter-5. The external acoustic forcing is modelled as a harmonic velocity perturbation applied at the burner lip. Hence the total velocity perturbation at this position is a sum of the self-excited oscillations and the external forcing. The self-excited and forced perturbations may simply be added together because the acoustics behave linearly. The net perturbations propagate along the flame surface and are governed by the advection equation, Eq. (5.1). Therefore the flame experiences the combined effect of the forced perturbation and the self-excited oscillation.

The frequency of forcing, $^{f_f}/_{f_n}$, is varied from 0.85 to 1.15 in steps of 0.01 with a high-resolution of 0.001 for $0.98 < {}^{f_f}/_{f_n} < 1.02$. Here f_n is defined as (i) the frequency of the limit cycle of a periodic oscillation; or (ii) one of the two characteristic frequencies of the 2-torus of a quasi-periodic oscillation; or (iii) the most dominant frequency in the spectrum of a chaotic oscillation. The amplitude of forcing, $^{u'}/_{U_0}$, is varied from 0.01 to 0.60 in steps of 0.01. We find that this range of amplitudes is sufficient to achieve lock-in in all cases.

A full description of the synchronization properties of this system requires the determination of the Arnold tongues [89]. In this study, however, we restrict our analysis to the vicinity of the 1:1 Arnold tongue, *i.e.* $f_f \approx f_n$. Therefore we do not study the phenomena of sub- and super-harmonic synchronization.

The response of the system is measured in the pressure fluctuation at a fixed position in the duct ($x = 0.375$). We choose this location because it is sufficiently far away from the pressure nodes of the most dominant acoustic modes. We use time series lasting 400 cycles of the fundamental acoustic mode, which allows us to capture very low-frequency modulations of the dominant mode when the system is close to the synchronization boundary.

The instantaneous amplitude and phase of the pressure is found using the Hilbert transform [186]. The advantage of the Hilbert transform is that it can be applied to nonlinear and nonstationary data. Its usefulness in the study of nonlinear dynamics and synchronization has been described by Pikovsky [89]. We use the MATLAB function *Hilbert* to calculate the Hilbert transform in the time domain, which uses an algorithm by Little and Shure [187].

There are different types of synchronization: frequency-locking, phase-locking, generalized synchronization and complete synchronization [89]. In this study we use the terms *entrainment* and *lock-in* interchangeably to refer to the phenomenon of phase-locking, which occurs when a self-excited system forced externally has a constant phase lag (or lead) with respect to the forcing at all instants of time. This implies that its natural frequency is quenched and it oscillates only at the forced frequency. Frequency-locking is the phenomenon of zero *average* frequency difference between the forcing and response of the system. Therefore the phase difference can vary from one instant to another.

The dynamics of self-excited thermoacoustic systems and the phenomenon of synchronization are governed by nonlinear processes and cannot be described with linear approaches. We use methods from nonlinear dynamical systems theory and nonlinear time series analysis to analyse the behaviour of our system. Some of these techniques were described in §5.2.2 and are explained in detail in texts in nonlinear dynamics [34; 61; 149; 151].

6.3 The (unforced) self-excited system

The dynamics of the unforced self-excited system were described in chapter-5. We choose a set of cases at the following flame locations from Fig. 5.1 to examine the forced response in this study: (i) $x_f = 0.166$, a period-*1* oscillation originating from a supercritical Hopf bifurcation; (ii) $x_f = 0.480$, a period-*1* oscillation originating from a subcritical Hopf bifurcation followed by a fold bifurcation; (iii) $x_f = 0.400$, a quasi-periodic oscillation and (iv) $x_f = 0.067$, a chaotic oscillation. In chapter-5 the time series, power spectra, phase portraits, Poincaré sections, correlation dimensions and instantaneous flame images of these self-excited states were shown and are not reproduced here. These cases are chosen because (i) they are representative of the different types of oscillation in this thermoacoustic system, (ii) they include limit cycles due to both subcritical and supercritical Hopf bifurcations, and (iii) their amplitudes are small enough that lock-in may be achieved with low to moderate forcing amplitudes, so that the attachment boundary condition used for the flame remains justified.

The nondimensional natural frequency for case (i) is $f_n = 2.304$ and for case (ii) is $f_n = 1.125$. The characterisitic frequencies of the 2-torus corresponding to the quasi-periodic oscillation of case (iii) are $f_1 = 2.22$ and $f_2 = 0.17$. The most dominant frequency in the spectrum of case (iv) is $f_n = 1.16$. The frequency of the fundamental acoustic mode in the absence of heat release and damping is used for the non-dimensionalisation.

6.4 Forced response of the system during a period-*1* oscillation

In this section we examine the dynamics of the system during a period-*1* oscillation leading up to lock-in for forcing frequencies above and below the natural frequency, both close to and far away from it. We also examine the response of the system when the forcing is increased beyond lock-in.

6.4.1 Dynamics before lock-in: bifurcations, frequency shifts and system response

Figure 6.1 shows the response of the system when it is forced at a frequency different from the natural frequency of its unforced period-*1* oscillation (f_n), in this case $^{f_f}/_{f_n} = 0.98$ (case (i) described in §6.3, $f_n = 2.304$). The time series and Poincaré sections are shown for increasing forcing amplitudes: (a) $\epsilon \equiv {}^{u'_{forced}}/_{U_0} = 0.03$, (b) $\epsilon = 0.06$, (c) $\epsilon = 0.09$, (d) $\epsilon = 0.11$, (e) $\epsilon = 0.12$, (f) $\epsilon = 0.125$, and (g) $\epsilon = 0.13$.

When forced, the system responds at both its natural frequency and the forcing frequency but the natural frequency (f'_n) is no longer the same as the unforced

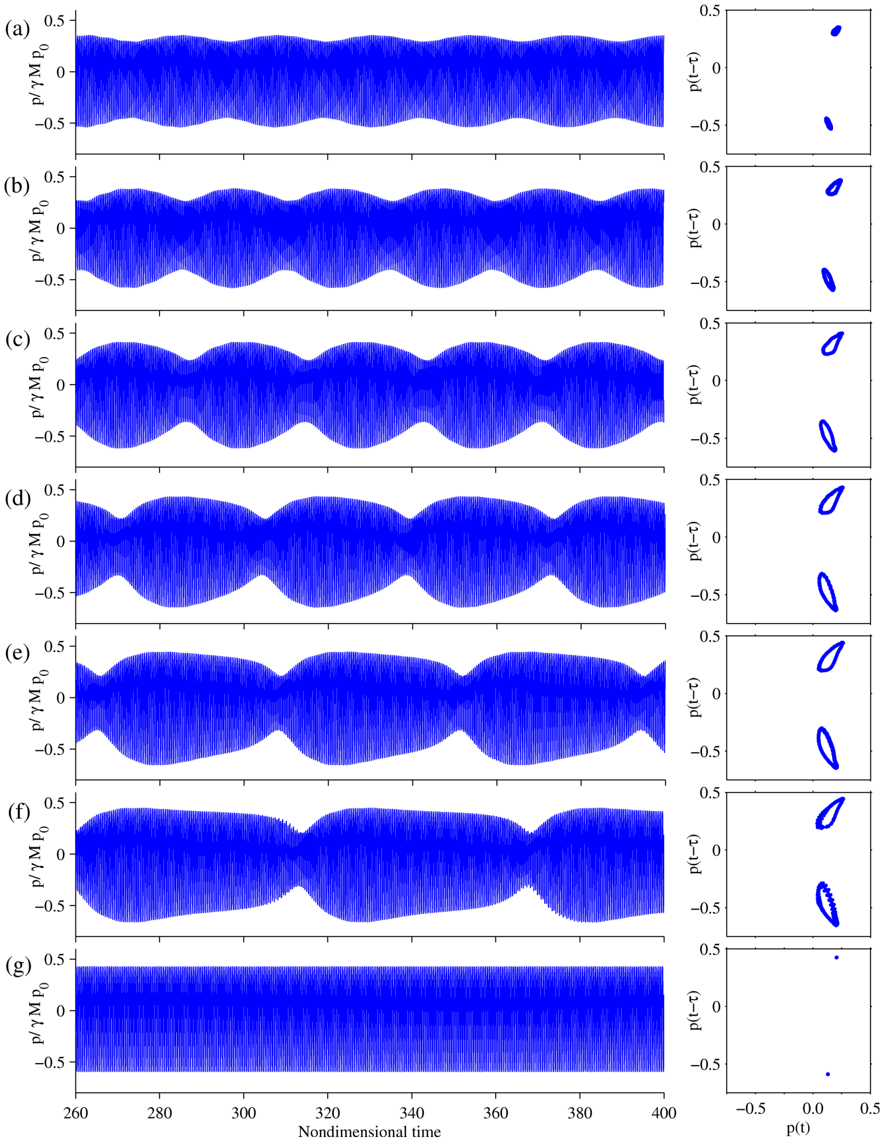

Figure 6.1: Forced response of the system when it is forced at a frequency different from the natural frequency of its unforced period-*1* oscillation (f_n): $^{f_f}/_{f_n} = 0.98$, $f_n = 2.304$. Time series and Poincaré sections are shown for increasing forcing amplitudes: (a) $\epsilon = {}^{u'_{forced}}/_{U_0} = 0.03$, (b) $\epsilon = 0.06$, (c) $\epsilon = 0.09$, (d) $\epsilon = 0.11$, (e) $\epsilon = 0.12$, (f) $\epsilon = 0.125$, and (g) $\epsilon = 0.13$.

case (f_n). These oscillations (a–f) are quasi-periodic and arise due to a Neimark-Sacker (also known as torus birth) bifurcation of the unforced period-*1* oscillation [188]. The power spectrum (not shown here but similar to Fig. 6 in [88]) contains peaks at linear combinations of the natural and forced frequencies due to nonlinear interactions between the forced and natural modes. The Poincaré maps show rings that indicate that the trajectory in phase space is not closed but spans the surface of a stable ergodic 2-torus.

At a critical amplitude (frame g, $\epsilon = 0.13$) the system locks into the forcing and oscillates at the forcing frequency. The Poincaré section has only two points indicating a closed period-*1* trajectory in phase space. The transition from a quasi-periodic oscillation to a period-*1* oscillation is abrupt, which suggests that it occurs via a saddle-node bifurcation [188]. This will be confirmed in subsequent discussions. The period-*1* oscillation at lock-in is a stable periodic orbit on the surface of the 2-torus that exists just before the saddle-node bifurcation [188].

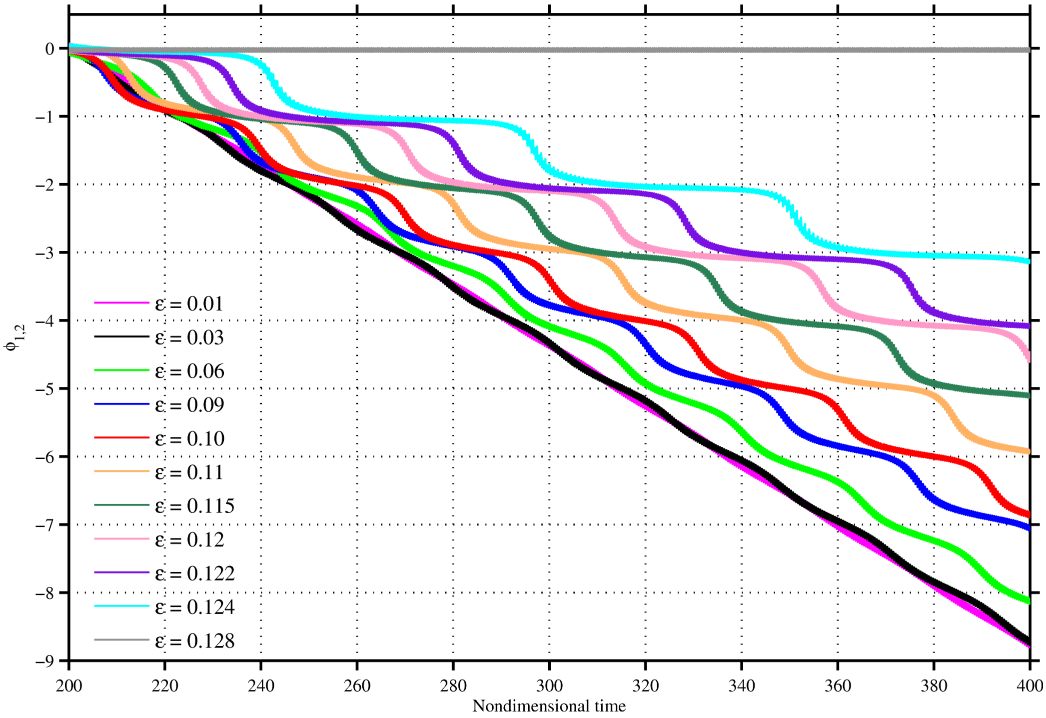

Figure 6.2: The phase difference (normalized by 2π) between the response of the system and the forcing for the conditions of the previous figure, *i.e.* when it is forced at a frequency different from the natural frequency of its unforced period-*1* oscillation, $f_f/f_n = 0.98$, at increasing forcing amplitudes.

Figure 6.2 shows the phase difference between the response of the system and the forcing for the conditions of the previous figure, *i.e.* when it is forced at a frequency different from the natural frequency of its unforced period-*1* oscillation, $f_f/f_n = 0.98$, at increasing forcing amplitudes. The phase is obtained using the Hilbert transform, as described in §6.2 and the phase difference, $\phi_{1,2}$, has been normalized by 2π.

In this figure the average slope of each curve is the beating frequency, $f = f'_n - f_f$, at that forcing amplitude. This shows that in all cases except at the highest forcing amplitude ($\epsilon = 0.128$), the oscillations are quasi-periodic and the natural frequency of the system is not equal to the forcing frequency.

At the lowest forcing amplitude ($\epsilon = 0.01$) the phase difference is almost linear. At intermediate forcing amplitudes the phase difference grows in a wavy pattern with alternating periods of close to synchronized behaviour (small slope) and relatively short periods of rapid phase increase, called phase slips [89]. Importantly, the magnitude of the average slope of each curve decreases, indicating that the natural frequency, f'_n, approaches the forcing frequency, f_f, as the forcing amplitude increases. This is characteristic of lock-in via a saddle-node bifurcation and is called frequency-pulling [188]. At large forcing amplitudes ($\epsilon > 0.12$) there are periods when the phase difference is nearly constant, indicating almost synchronous behaviour, with phase slips that occur relatively rapidly. The phase slips are equal to -2π because they correspond to the system making one additional cycle with respect to the forcing. The rapidity of the phase slip depends on the amplitude of forcing. For weak forcing the slip occurs within several periods of the forcing signal but, for strong forcing, the slip occurs over a very short time interval [89]. Finally, as the forcing amplitude increases, the time intervals between slips also increase, ultimately leading to infinitely long intervals of constant phase difference, *i.e.* lock-in.

The behaviour described in figures 6.1 and 6.2 is also observed for $f_f > f_n$ as long as f_f is close to f_n. The sequence of bifurcations: torus birth bifurcation to quasi-periodicity and saddle-node bifurcation to lock-in, remains unchanged. When $f_f > f_n$, however, the phase slips occur in the opposite direction ($+2\pi$) because in this case the system loses one cycle with respect to the forcing when it slips.

Figure 6.3 shows the response of the system when it is forced at $f_f/f_n = 1.02$. The unforced case is case (ii) described in §6.3 and is shown in frame (a). The

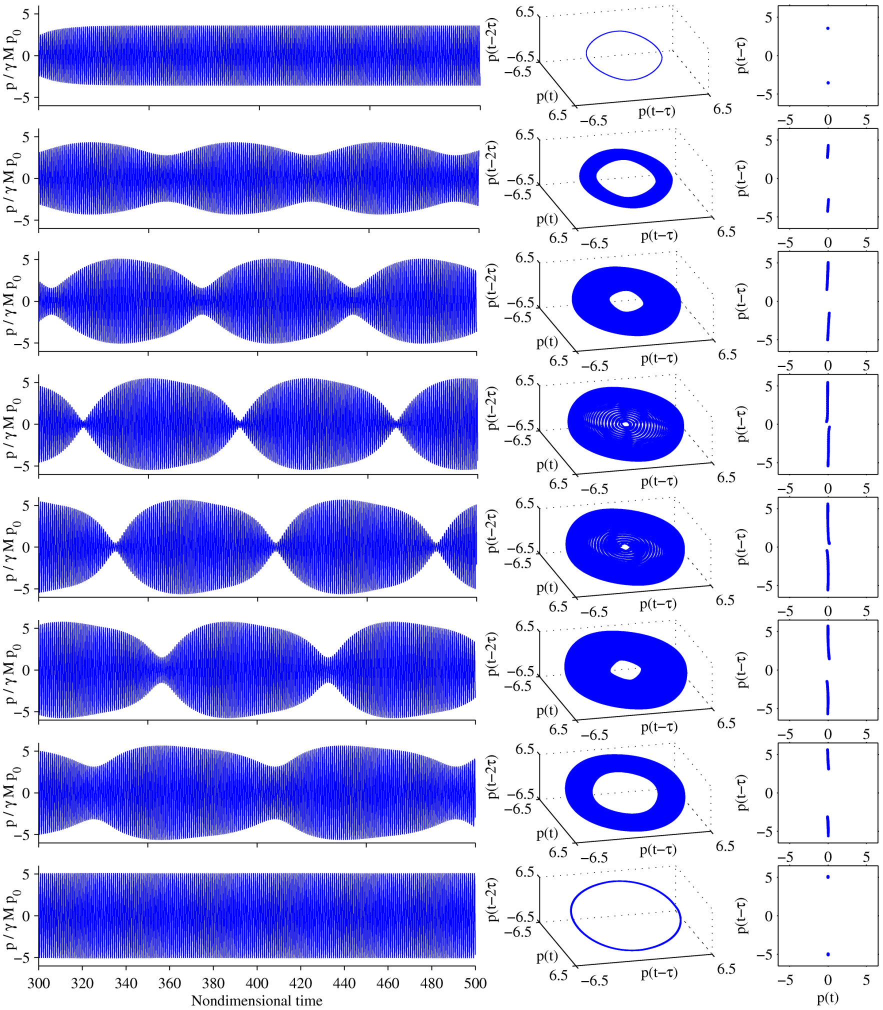

Figure 6.3: Forced response of the system when it is forced at ${}^{f_f}/_{f_n} = 1.02$, $f_n = 1.125$. The unforced case is case (ii) described in §6.3 and is shown in frame (a). The time series, phase portraits and Poincaré sections are shown for increasing forcing amplitudes: (b) $\epsilon = {}^{u'_{forced}}/_{U_0} = 0.03$, (c) $\epsilon = 0.05$, (d) $\epsilon = 0.0715$, (e) $\epsilon = 0.0725$, (f) $\epsilon = 0.075$, (g) $\epsilon = 0.0775$, and (h) $\epsilon = 0.08$.

time series, phase portraits and Poincaré sections are shown for various forcing amplitudes mentioned in the caption. The phase portraits are computed after the system reaches a steady state.

As in case (i), when forced the system responds at both its natural frequency and the forcing frequency. The oscillations (a–f) are quasi-periodic and arise due to a torus-birth bifurcation. Also, as in case (i), the spectrum contains peaks at linear combinations of the natural and forced frequencies, the Poincaré maps are rings and the time series shows beating. The crucial difference, however, is that the natural frequency of the system (f'_n) remains unchanged from its unforced value (f_n) and there is no frequency pulling. This suggests that the type of bifurcation that leads to lock-in is not a saddle-node bifurcation, as in the previous case.

At a critical amplitude (frame h, $\epsilon = 0.14$) the system locks into the forcing and oscillates at the forcing frequency. The Poincaré section has only two points indicating a closed period-*1* trajectory in phase space. Importantly, the transition from a quasi-periodic oscillation to a period-*1* oscillation is gradual, unlike in the previous case, and suggests that it occurs via an inverse Neimark-Sacker (also known as torus death) bifurcation [188]. Finally, in this case (figure 6.3) the amplitude of oscillations at lock-in is about 30% greater than that of the unforced case.

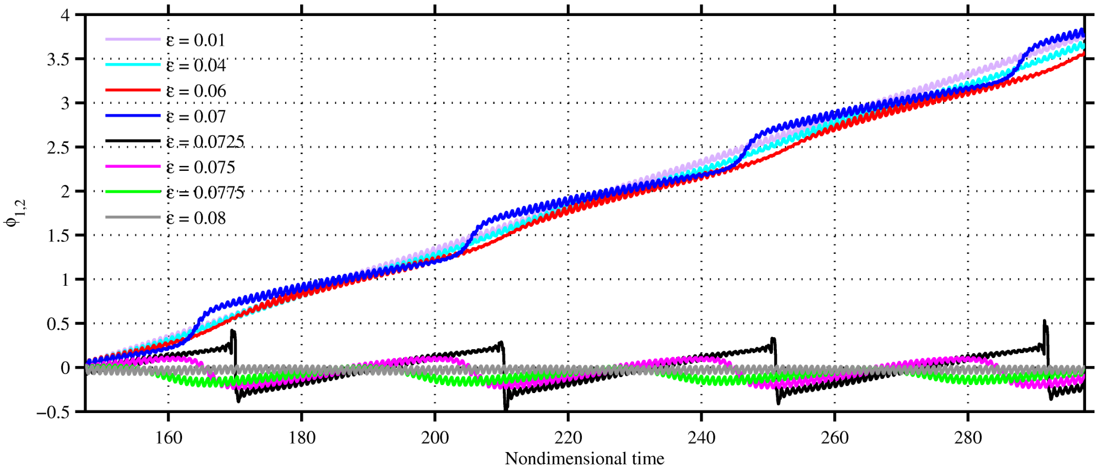

Figure 6.4: The phase difference (normalized by 2π) between the response of the system and the forcing for the conditions of figure 6.3, *i.e.* $f_f/f_n = 1.02$, at increasing forcing amplitudes.

Figure 6.4 shows the phase difference (normalized by 2π) between the response of the system and the forcing for the conditions in figure 6.3, *i.e.* when case (ii) described in §6.3 is forced at $f_f/f_n = 1.02$, at increasing forcing amplitudes. In this figure the curves either have an average slope equal to the beating frequency,

$f = f_f - f'_n = f_f - f_n$, at low forcing amplitudes ($0 < \epsilon < 0.07$), or zero, beyond a critical forcing amplitude ($\epsilon > 0.07$). This indicates that there is no frequency pulling, but an abrupt switch occurs at a critical point. The switch occurs when the strength of the forced mode overtakes that of the natural mode (not shown here but similar to Figs. 10 and 11 in [88]) and lies between frames (d) and (e) in figure 6.3. Both before and after the switch occurs, the phase difference increases over long time intervals interrupted by phase slips over relatively short time intervals. The intervals between adjacent phase slips remains fixed, however, indicating that the beating frequency remains constant. After the switch occurs, these phase slips keep the phase difference bounded within a 2π band around zero and is called phase trapping [89]. Importantly, these oscillations are still quasi-periodic and frequency-locked, but not phase-locked [89]. They only become phase-locked at lock-in, when the natural frequency is quenched completely ($\epsilon = 0.08$). The same behaviour is observed for $f_f < f_n$ within a range of values (not shown here for brevity).

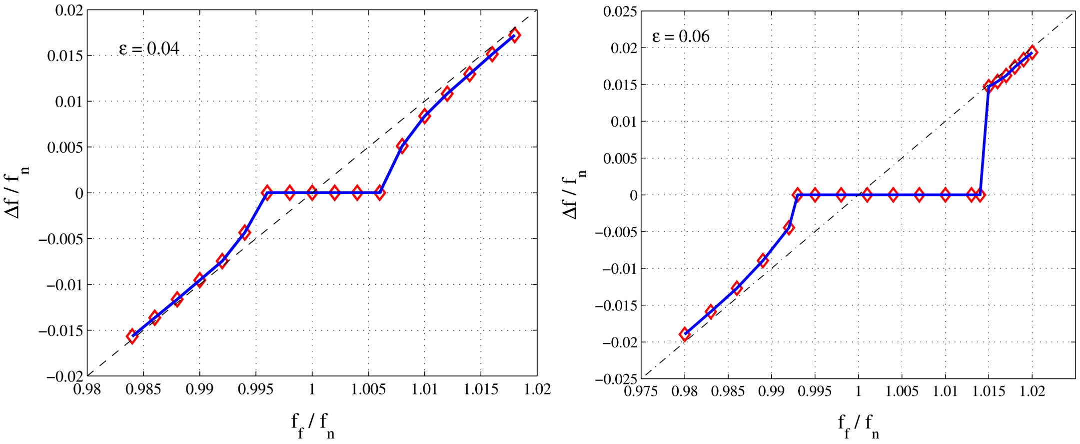

Figure 6.5: The dependence of the beating frequency, $\Delta f = f_f - f'_n$, on the forcing frequency, f_f, both normalized by the unforced natural frequency, f_n, at a fixed forcing amplitude. (a) At a low forcing amplitude ($\epsilon = 0.04$), the transitions are via saddle-node bifurcations for both $f_f < f_n$ and $f_f > f_n$. (b) At an intermediate forcing amplitude ($\epsilon = 0.06$), the transition is via a saddle-node bifurcations for $f_f < f_n$, but is via a torus death bifurcation for $f_f > f_n$.

Figure 6.5 shows the dependence of the beating frequency, $\Delta f = f_f - f'_n$, on the forcing frequency, f_f, both normalized by the unforced natural frequency, f_n, at a fixed forcing amplitude. In (a) the forcing amplitude is low ($\epsilon = 0.04$). The beating frequency around $f_f/f_n = 1$ is zero, which indicates lock-in. For higher or lower forcing forcing frequencies, the magnitude of the beating frequency has a nonlinear increase close to the lock-in boundary, but is nearly linear further away from the lock-in boundary. This implies that close to the lock-in boundary there is frequency pulling, but the system does not experience frequency pulling when f_f and f_n are far apart. The dependence described here has been derived analytically for saddle-node bifurcations and is well known in the literature of nonlinear dynamics [89]. The beating frequency has a square-root dependence on the frequency detuning close to the saddle-node bifurcation. Figure 6.5(a) shows similar behaviour (square-root dependence) on both sides of f_n.

Figure 6.5(b) shows the dependence of the beating frequency on frequency detuning at an intermediate forcing amplitude ($\epsilon = 0.06$). As in frame (a), the beating frequency around $f_f/f_n = 1$ is zero indicating lock-in. For f_f above f_n, however, the behaviour is not the same as in (a). The beating frequency has an abrupt increase close to the lock-in boundary, and is nearly linear further away from the lock-in boundary. This implies that close to the lock-in boundary there is no frequency pulling, but the natural frequency of the system, f_n', shifts abruptly from f_f to f_n. This suggests a torus death bifurcation, as mentioned in the discussion of figure 6.4. We will show in figure 6.8(a) that this is indeed the case.

Figure 6.6 shows the response of the system when it is forced at $f_f/f_n = 0.89$, *i.e.* far away from the unforced natural frequency. The unforced state is case (ii) and is shown in frame (a). The power spectra show a steady decrease in power of the natural mode and increase in power of the forced mode, with the natural mode being completely quenched at lock-in (frame h). This is similar to the behaviour in figure 6.3, however, they is an important difference: the overall amplitude of oscillations decreases gradually as the forcing is increased until lock-in, where the amplitude of oscillations is about 70% smaller than that of the unforced case. This means that suppression of self-excited oscillations is possible by open-loop forcing.

Figure 6.7 shows the phase difference (normalized by 2π) between the response of the system and the forcing for the conditions of figure 6.6. At low amplitudes

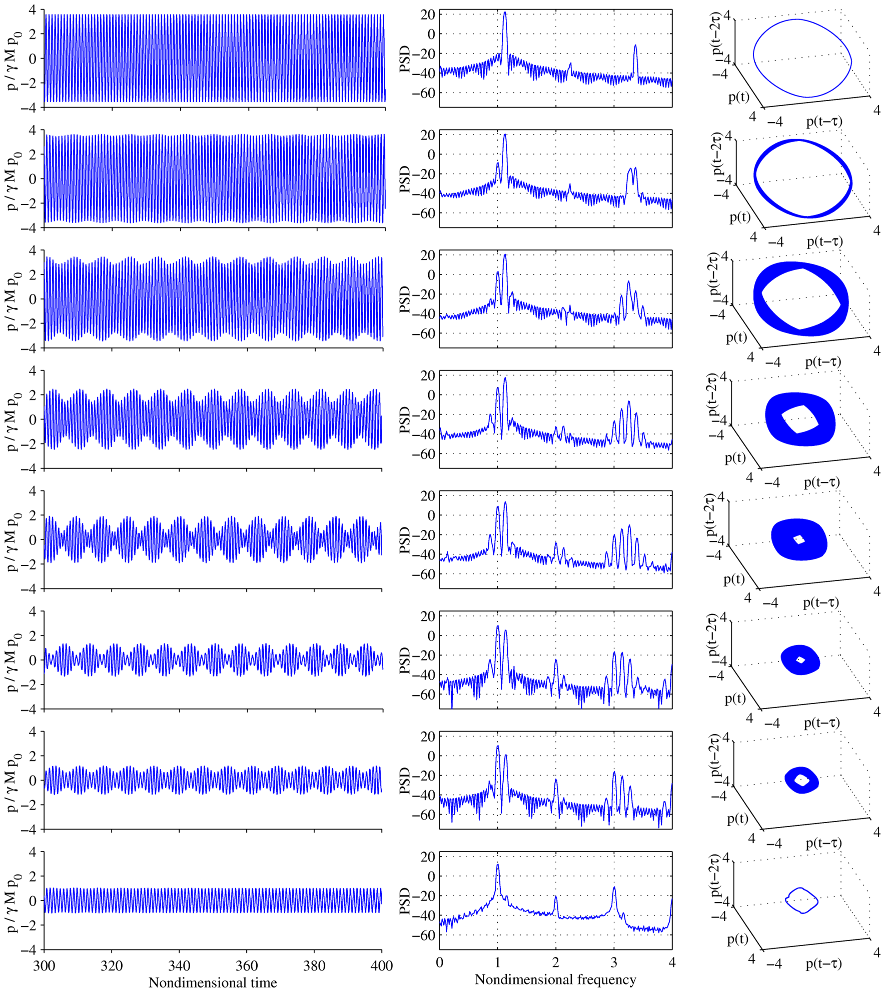

Figure 6.6: Forced response of the system when it is forced at ${}^{f_f}\!/_{f_n} = 0.89$, $f_n = 1.125$. The unforced case is case (ii) described in §6.3 and is shown in frame (a). Time series, power spectra and phase portraits are shown for increasing forcing amplitudes: (b) $\epsilon = {}^{u'_{forced}}\!/_{U_0} = 0.02$, (c) $\epsilon = 0.08$, (d) $\epsilon = 0.14$, (e) $\epsilon = 0.16$, (f) $\epsilon = 0.18$, (g) $\epsilon = 0.2$, and (h) $\epsilon = 0.23$.

$(0 < \epsilon < 0.08)$, the phase difference has an average slope equal to the beating frequency, $f = f_f - f'_n = f_f - f_n$. At intermediate amplitudes $(0.08 < \epsilon < 0.18)$, the magnitude of the average slope increases due to large phase slips greater than 2π, indicating frequency pushing, *i.e.* the natural frequency, f'_n, moves away from the forcing frequency. When the forcing amplitude is increased further $(0.18 < \epsilon < 0.218)$ the natural frequency, f'_n, is pulled back towards the forcing

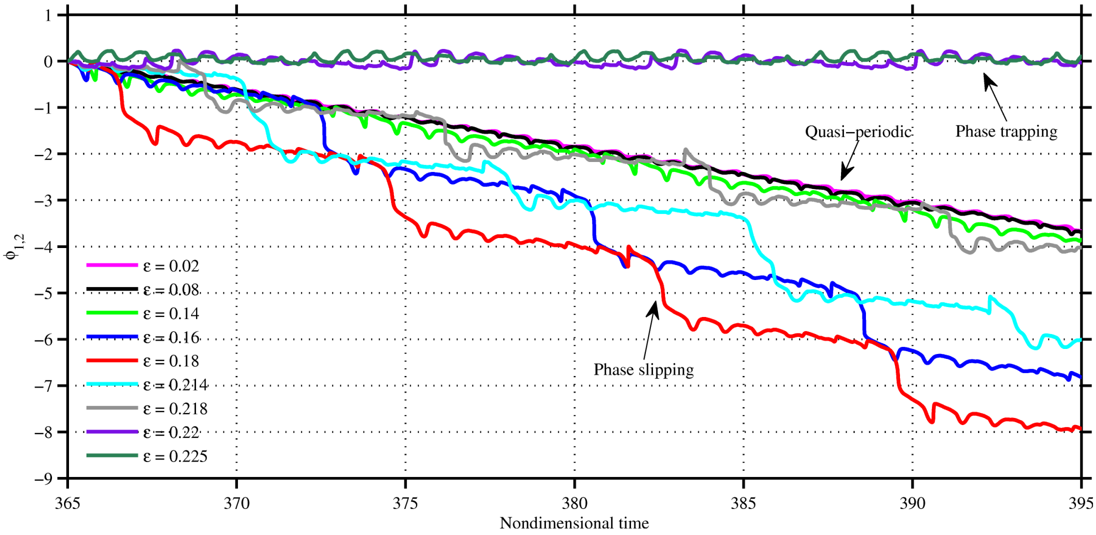

Figure 6.7: The phase difference (normalized by 2π) between the response of the system and the forcing for the conditions of figure 6.6, *i.e.* $^{f_f}/_{f_n} = 0.89$, at increasing forcing amplitudes.

frequency. Beyond a critical forcing amplitude and before lock-in ($0.22 < \epsilon < 0.24$), the phase difference is trapped around zero. This switch to phase trapping occurs when the strength of the forced mode overtakes that of the natural mode, and occurs between frames (e) and (f) in figure 6.6. Ultimately, lock-in occurs at $\epsilon = 0.24$ and the phase difference is constant.

The phenomenon of frequency pushing was noticed in experiments by Bellows *et al.* on a lean premixed gas turbine combustor for similar conditions, *i.e.* f_f less than f_n and far away from it. They mention that this shift in the natural frequency could not be explained simply. Frequency pushing is well known, however, in oscillations of magnetrons and has been modelled successfully by a cubic term in the van der Pol equation [189]. In magnetrons, it occurs due to highly nonlinear electron-wave interactions that change the mean field significantly [190]. Given the similarities between this thermoacoustic system and generalized nonlinear oscillators, we speculate that frequency pushing in thermoacoustics could be modelled by a cubic term, but confirming this speculation is beyond the scope of this study.

In summary, we see that this self-excited thermoacoustic system responds to forcing in different ways, depending on the proximity of the forcing frequency, f_f, to the natural frequency, f_n, and whether f_f is above or below f_n. When the amplitude of forcing is increased from zero, the system first undergoes a torus birth bifurcation to quasi-periodic oscillations. At a critical amplitude of forcing, the system locks into the forcing. If the forcing frequency is close to the natural frequency, lock in occurs via a saddle-node bifurcation with frequency pulling. If the forcing frequency is not close to the natural frequency, lock in occurs via a torus death bifurcation without frequency pulling, but with frequency pushing if the forcing frequency and natural frequency are far apart. Two important features of this behaviour are: (i) it is not symmetric about $^{f_f}/_{f_n} = 1.0$, and (ii) the amplitude of oscillations at lock-in may be higher or lower than the unforced case, and these are discussed next.

6.4.2 Lock-in: the 1:1 Arnold tongue and system response amplitudes

In this section the behaviour at lock-in is examined. Figure 6.8 shows that the minimum forcing amplitude required to achieve lock-in, (ϵ_{lock}), depends on the frequency detuning, *i.e.* the difference between the forcing frequency and natural frequency, f_f-f_n. The diamond markers represent saddle-node bifurcations and circular markers represent torus death bifurcations. The dashed lines are linear fits to the saddle-node bifurcations on either side of $^{f_f}/_{f_n} = 1.0$. The bifurcations to lock-in depend on the proximity of the forcing and natural frequencies and is asymmetric about $^{f_f}/_{f_n} = 1.0$.

In Figure 6.8(a), on both sides of the natural frequency, the critical amplitude for lock-in, ϵ_{lock}, increases linearly in the regime of saddle-node bifurcations, *i.e.* when f_f is close to f_n. This is similar to the characteristic 'V'-shaped curve seen in experiments by Bellows *et al.* [25] on a self-excited lean premixed gas turbine combustor and those by Li and Juniper [179] on a hydrodynamically self-excited jet diffusion flame. The lines are asymmetric about $^{f_f}/_{f_n} = 1.0$; lock-in occurs more readily for $^{f_f}/_{f_n} > 1.0$ than for $^{f_f}/_{f_n} < 1.0$. This was also noticed in experiments on a self-excited jet diffusion flame [179]. The boundary between the saddle-node and torus death bifurcations is lower for $^{f_f}/_{f_n} > 1.0$ than for

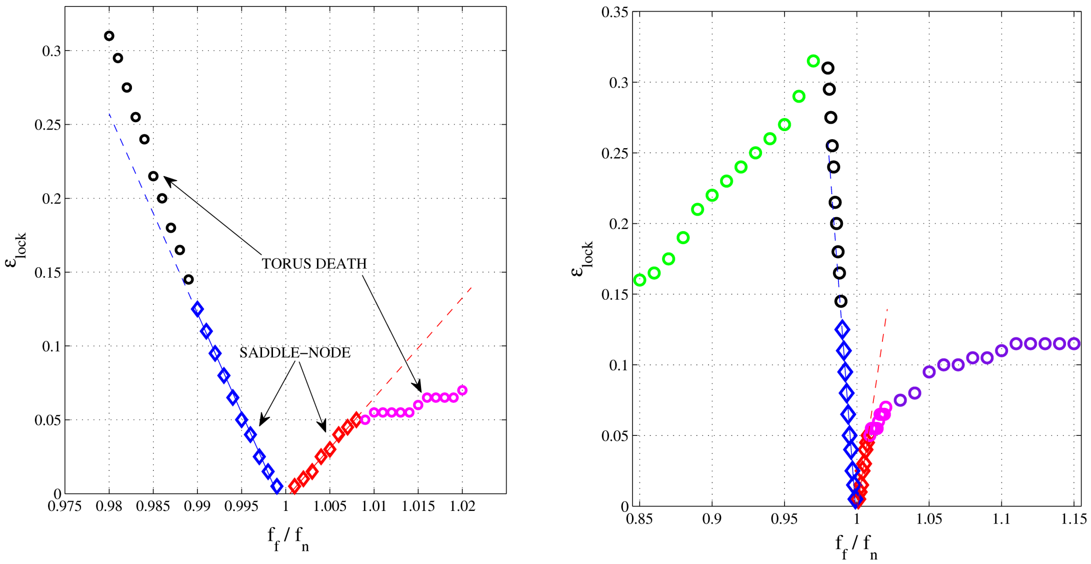

Figure 6.8: The 1:1 Arnold tongue, *i.e.* minimum forcing amplitude required to achieve lock-in. The diamond markers represent saddle-node bifurcations and circular markers represent torus death bifurcations. The dashed lines are linear fits to the saddle-node bifurcations on either side of $f_f/f_n = 1.0$. The different colours show different regimes. (a) small range of frequency detuning ($0.98 < f_f/f_n < 1.02$) and (b) large range of frequency detuning ($0.85 < f_f/f_n < 1.15$).

$f_f/f_n < 1.0$. Beyond this boundary, the locus of torus death bifurcations are not linear. This has been proved analytically for a van der Pol oscillator and the shape of Arnold tongues is extensively researched in the literature of synchronization [89].

Importantly, the loci of the torus death bifurcations on either side of f_n, *i.e.* the left and right branches of the Arnold tongue, are strikingly different: ϵ_{lock} seems to saturate for $f_f/f_n > 1.0$ but grows with large gradient for $f_f/f_n < 1.0$. Figure 6.8(b) shows the Arnold tongue over a wider range of frequency detuning. Whereas for $f_f > f_n$ the curve plateaus at around $\epsilon_{lock} = 0.12$, for $f_f < f_n$, there is a maximum at $f^* = f_f/f_n = 0.97$ followed by a decrease in the minimum amplitude for lock-in as the frequency detuning increases. The behaviour of the left branch (sharp increase with a maximum for $f_f < f_n$) is the same as that noticed in experiments on a self-excited jet diffusion flame [179]. It is, however, unclear why this happens.

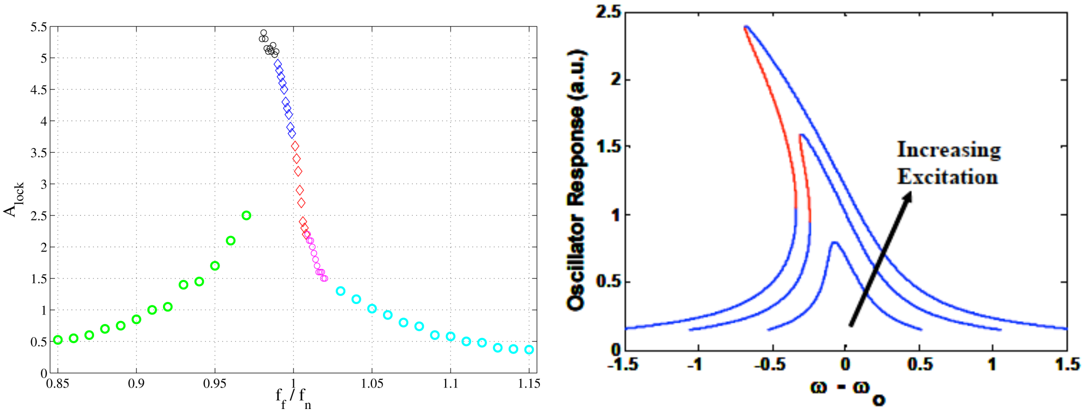

Figure 6.9: (a) The system response at lock-in, *i.e.* at the critical forcing amplitude, ϵ_{lock}. The response is measured in the nondimensiaonl amplitude of pressure oscillations, $p'/\gamma M p_0 = A_{lock}$. The diamond markers represent saddle-node bifurcations and circular markers represent torus death bifurcations. The colours denote the different regimes in the discussion of figure 6.8. (b) Figure reproduced from Bellows' thesis [25]. The response of a single second-order nonlinear damped oscillator of the form: $\ddot{x} + 2\zeta\omega_0\dot{x} + \omega_0^2 x = \alpha x^3 + A\cos(\omega t)$, where the x^3 term on the right hand side represents the nonlinear 'stiffness'.

Figure 6.9(a) shows the response of the system at lock-in, *i.e.* at the critical forcing amplitude, ϵ_{lock}. The response is measured in the nondimensiaonl amplitude of pressure oscillations, $p'/\gamma M p_0 = A_{lock}$. The maximum at a frequency below f_n and the sharp decrease on either side has been noticed in experiments by Li on a self-excited jet diffusion flame [179] and in experiments on a self-excited premixed combustor [25]. Furthermore, similar behaviour is seen in a forced nonlinear oscillator with a cubic nonlinearity [191] (frame (b)), including the abrupt decrease just below the peak response. Note, however, that ϵ_{lock} is not the same at all forcing frequencies. The abrupt change at $f_f/f_n = 0.97$ suggests that the left branch of the Arnold tongue becomes unstable due to a subcrtical bifurcation but is re-stabilized at a lower value, probably due to a fold bifurcation. This is true of the simple oscillator shown in figure 6.9(b) (the unstable branch is marked in red). Bellows also measured hysteresis in his experiments on a premixed combustor in this range of frequencies, indicating a region of bi-stability [25].

In summary, lock-in occurs most readily when f_f is close to f_n but the behaviour depends strongly on whether f_f is above or below f_n. When forced below f_n and close to it, large forcing amplitudes are required for lock-in. When forced above f_n, lock-in occurs at lower forcing amplitudes. For f_f below f_n, however, both the forcing amplitude required for lock-in and the system response at lock-in are not monotonic – they reach a maximum at a frequency close to f_n and decrease for lower frequencies. Finally, when f_f is gradually decreased from f_n, the response at lock-in increases sharply until the response reaches a maximum and drops abruptly for lower f_f. Whereas, when f_f is gradually increased from f_n, the response at lock-in decreases sharply to as low as 10% of the unforced case. This implies that lock-in can be an effective means of suppressing nonlinear thermoacoustic oscillations, provided the forcing frequency is chosen carefully.

6.5 Elaborate routes to lock-in: lock-in via intermittency

We have shown in previous sections that the transition to lock-in can be via a torus birth bifurcation followed by either a saddle-node or a torus death bifurcation. This is true for many periodic oscillations. In some cases, however, the transition to lock-in may involve other bifurcations, including transition to chaos [89]. This may occur due to large amplitudes of forcing, forcing frequencies far away from the natural frequency, or because the self-excited oscillations are highly resistant to external forces.

Figure 6.10 shows the transition to lock-in when the system is forced at a $^{f_f}/_{f_n} = 0.97$. The unforced case is case-1 described in §6.3. As in previous cases, the first transition to quasi-periodic oscillations via a torus birth bifurcation. When the amplitude of forcing is increased, the torus becomes intermittently unstable, *i.e.* trajectories in a neighbourhood on the surface of the torus start to diverge. This is seen as mildly chaotic oscillations between the ‘quiet’ quasi-periodic intervals in the time series. Complete breakdown of the torus to fully chaotic oscillations, however, does not occur. At a different operating point, however, complete breakdown to chaos occurs and resembles the Ruelle-Takens-Newhouse route presented in Chapter 5 (figures 5.12 and 5.13). The chaotic

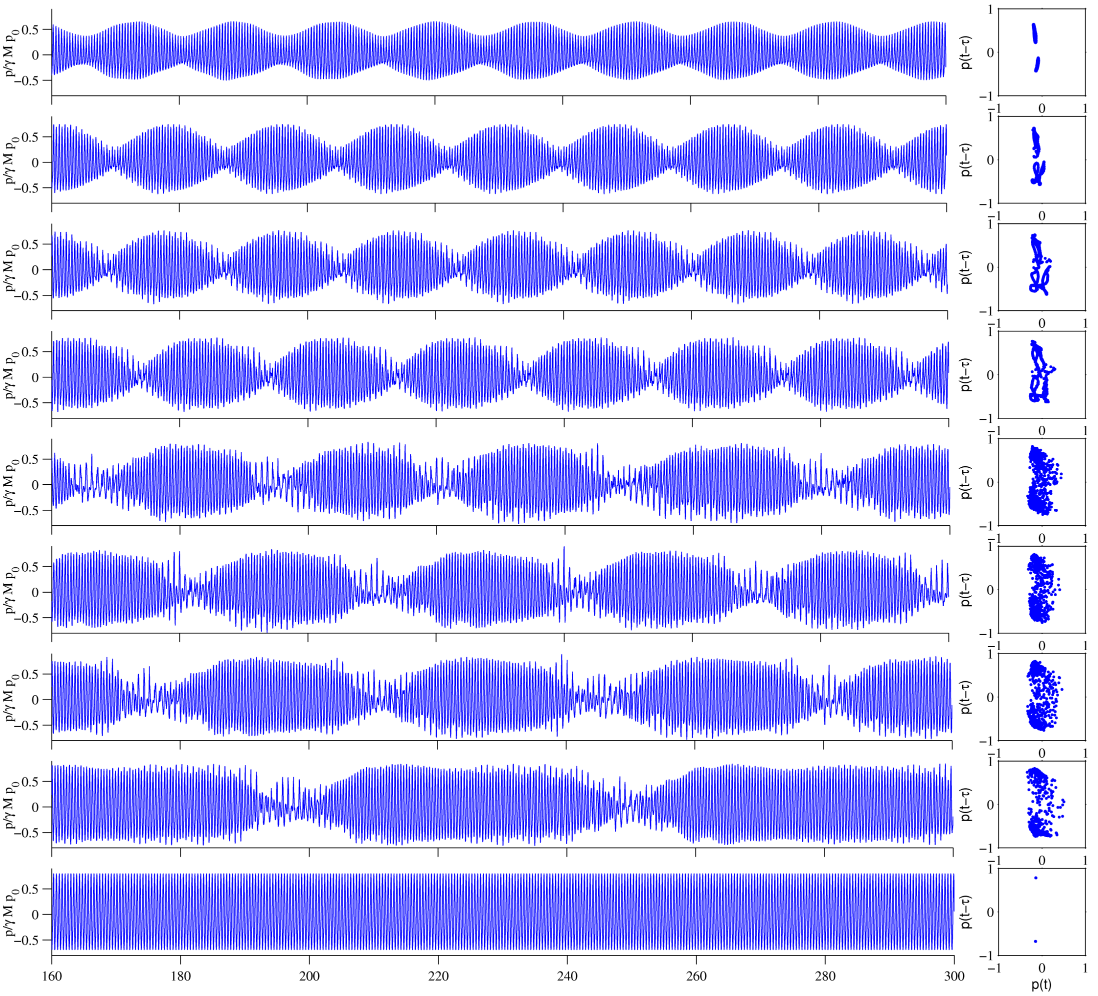

Figure 6.10: Forced response of the system when it is forced at a ${}^{f_f}/_{f_n} = 0.97$. The unforced case is case-1 described in §6.3. Time series and Poincaré sections are shown for increasing forcing amplitudes: (a) $\epsilon = 0.06$, (b) $\epsilon = 0.12$, (c) $\epsilon = 0.16$, (d) $\epsilon = 0.18$, (e) $\epsilon = 0.20$, (f) $\epsilon = 0.21$, (g) $\epsilon = 0.22$, (h) $\epsilon = 0.23$ and (i) $\epsilon = 0.24$.

oscillations lock-in to the forcing when the forcing amplitude is increased further.

Figure 6.11 shows the phase difference between the response of the system and the forcing for the same case as Fig 6.10. At low forcing amplitudes, when the amplitude of forcing increases, the magnitude of the slope of the phase difference decreases, indicating frequency pulling. For higher amplitudes of forcing ($\epsilon > 0.15$) large phase slips occur between periods of quasi-periodicity. The arrows show that the phase slips are not always 2π but can be significantly larger. Impor-

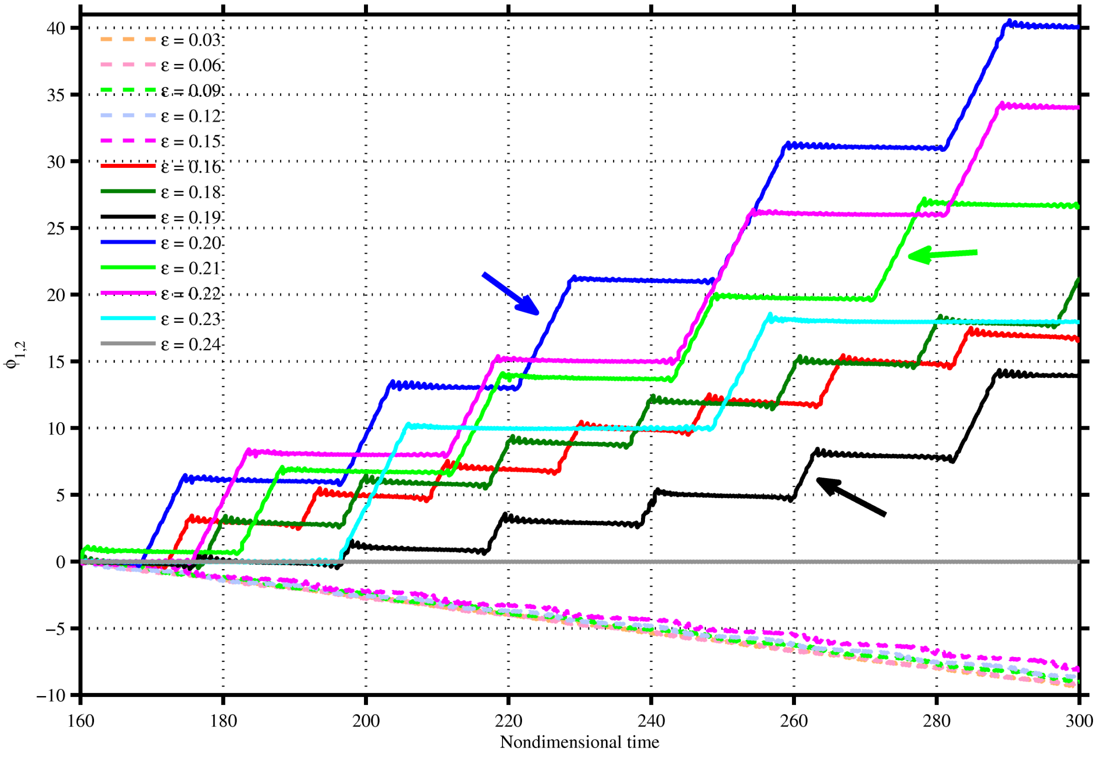

Figure 6.11: The phase difference (normalized by 2π) between the response of the system and the forcing for the conditions of figure 6.10 at various forcing amplitudes marked in the figure.

tantly, they are not the same even for a fixed amplitude of forcing. Furthermore, the time intervals between adjacent phase slips is not constant at each forcing amplitude. Examining figures 6.10 and 6.11 together shows that the phase slips coincide with the intervals of intermittent 'spikes' in the time series (which also coincide with the intermittent instability (of trajectories) phase space). When the forcing amplitude is increased further ($0.22 < \epsilon < 0.24$), the phase slips become more infrequent and at $\epsilon = 0.24$, the slope of the phase difference is zero, indicating lock-in.

Such behaviour is well-known in synchronization and has been studied extensively in many systems, from simple one-dimensional maps such as the circle map to more complex systems of coupled chaotic oscillators [192; 193]. The reasons behind the various transitions and the bifurcations causing them has been studied for low-dimensional systems using unstable periodic orbit theory [194]. A detailed investigation of these transitions in our system is beyond the scope of this study.

6.6 Beyond Lock-in: stability of the synchronized oscillation

Once the system locks into the forcing, as the forcing amplitude is increased further, the amplitude of the periodic oscillation at the forcing frequency f_f increases. Beyond a certain forcing amplitude the periodic orbit loses stability. For large amplitudes of forcing there are other transitions from lock-in, and they typically lead to chaotic behavior [89]. Pikovsky *et al.* state that there are three main routes to chaos: the first route is the transition to chaos through period-doublings of the stable periodic orbit, the second and third are via intermittency, which is observed as long laminar nearly synchronized periods and phase slips that occur at chaotic time intervals. The first route is typical for the center of the Arnold tongue. Here, with an increase in the forcing amplitude, the transition to chaos through period-doublings can occur. The second and third routes occur at the border of the Arnold tongue, usually as the frequency detuning is increased [89].

Figure 6.12 shows the first route to chaos described above, the period-doubling route to chaos. In chapter-5 we observed this route to chaos when the flame position in the duct was changed (see Fig. 5.11). In this figure the same behaviour is seen when the forcing amplitude is increased. The period-*1* oscillation undergoes a period-doubling bifurcation to period-*2* oscillations, followed by another period-doubling bifurcation to period-4 oscillations and so on. The spectra show the emergence of a subharmonic at each bifurcation: $^f/_2$ in (b), $^f/_4$ in (c), $^f/_8$ in (d), ultimately leading to chaos in frame (e).

Apart from the possibility of chaotic behaviour there are other features of synchronization at large forcing amplitude that are different compared with small forcing amplitudes [89]. Different synchronization regions can overlap, thus leading to multistability, so that for certain parameters periodic oscillations with

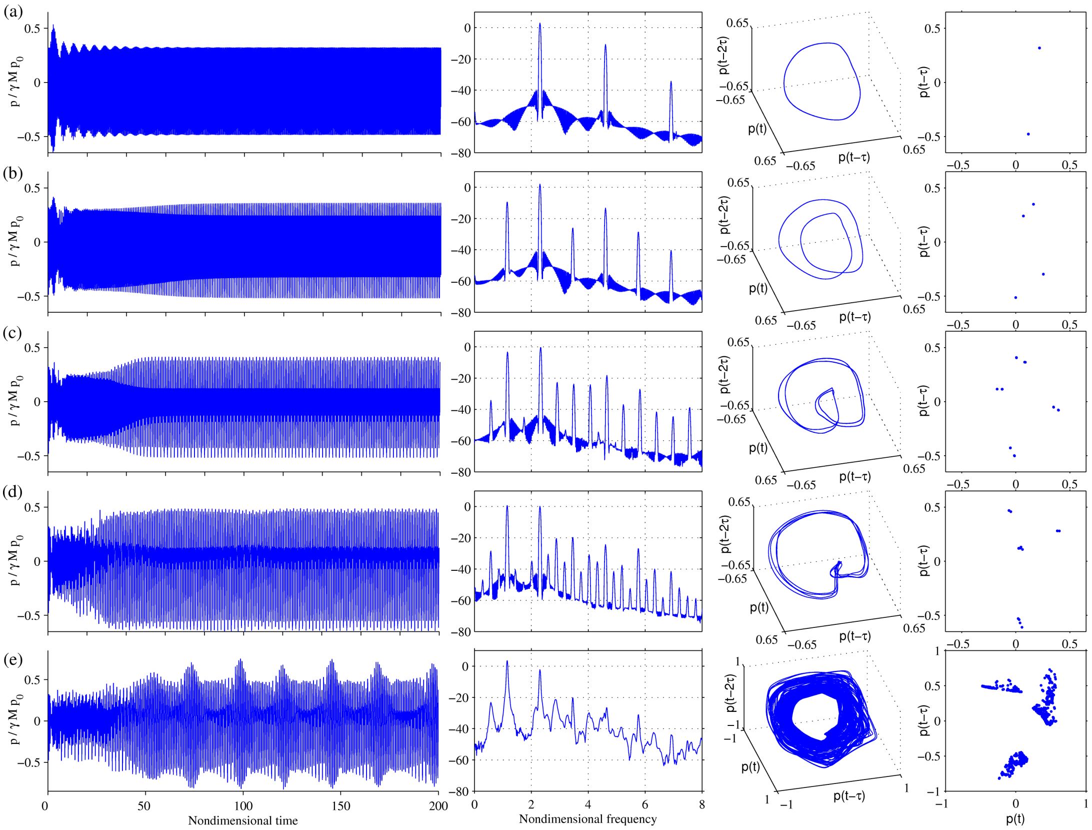

Figure 6.12: Forced response of the system when it is forced at a $f_f/f_n = 1$. The unforced case is case-2 described in §6.3. Time series and Poincaré sections are shown for increasing forcing amplitudes: (a) $\epsilon = 0.16$, (b) $\epsilon = 0.24$, (c) $\epsilon = 0.30$, (d) $\epsilon = 0.34$, (e) $\epsilon = 0.36$.

different rational ratios between the observed and the forcing frequencies coexist. This phenomenon has been experimentally observed by van der Pol and van der Mark [195].

Figure 6.13 shows this phenomenon in our system when it is forced at $f_f/f_n = 1.06$. In (a) we see the characteristic quasi-periodic oscillation after the torus birth bifurcation, followed by lock-in via a torus death bifurcation at $\epsilon = 0.12$. When the forcing amplitude is increased further, the system switches to a periodic oscillation at half the forcing frequency, seen in frame (b). At still larger forcing amplitudes it switches back to the lock-in state at the forcing frequency, seen in frame (e). This occurs because the forcing modifies the stability of different attractors and alters their basins of attraction, making one state more stable than

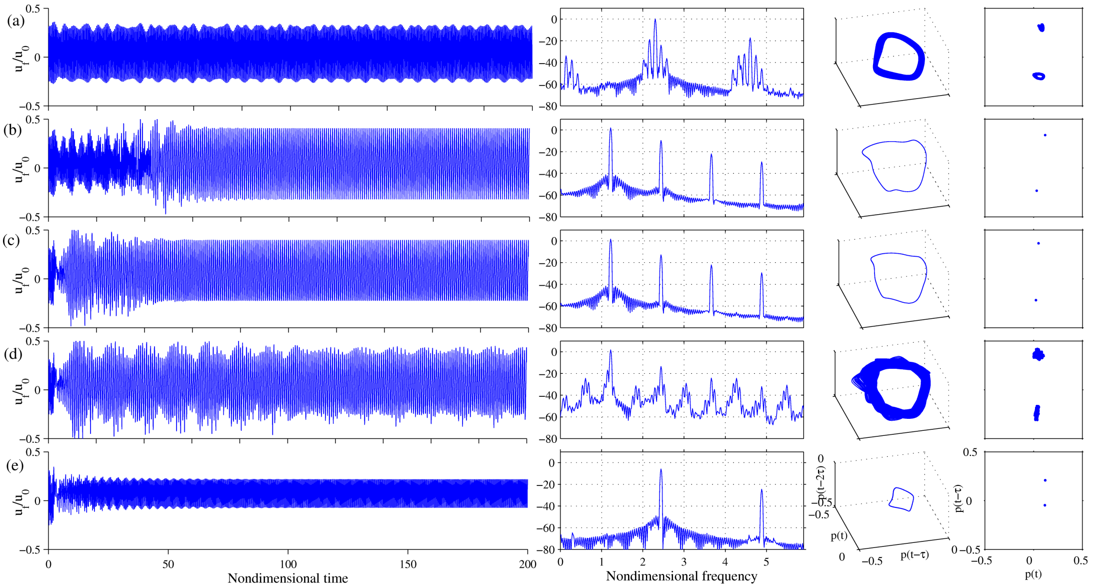

Figure 6.13: Forced response of the system when it is forced at a ${}^{f_f}/_{f_n} = 1.06$. The unforced case is case-1 described in §6.3. Time series and Poincaré sections are shown for increasing forcing amplitudes: (a) $\epsilon = 0.03$, (b) $\epsilon = 0.16$, (c) $\epsilon = 0.18$, (d) $\epsilon = 0.21$, (e) $\epsilon = 0.24$.

the other depending on the forcing amplitude [89].

6.7 Harmonic forcing of aperiodic oscillations

In chapter-5 we showed that this self-excited system can have, besides periodic oscillations, quasi-periodic and chaotic oscillations. In this section we investigate the dynamics of forcing the system when its self-excited unforced state is aperiodic.

First we consider the system on a quasi-periodic oscillation whose characteristic frequencies are $f_1 = 2.22$ and $f_2 = 0.17$, with f_1 being more dominant than f_2. Figure 6.14 shows the response of the system when it is forced at f_1 at increasing forcing amplitudes. The time series show that the beating frequency decreases as the forcing is increased, which is also seen in the spectra as a steady decrease in the bandwidth of the side bands, indicating frequency pulling. The shape of the 2-torus is modified as frequency pulling occurs until the torus undergoes a

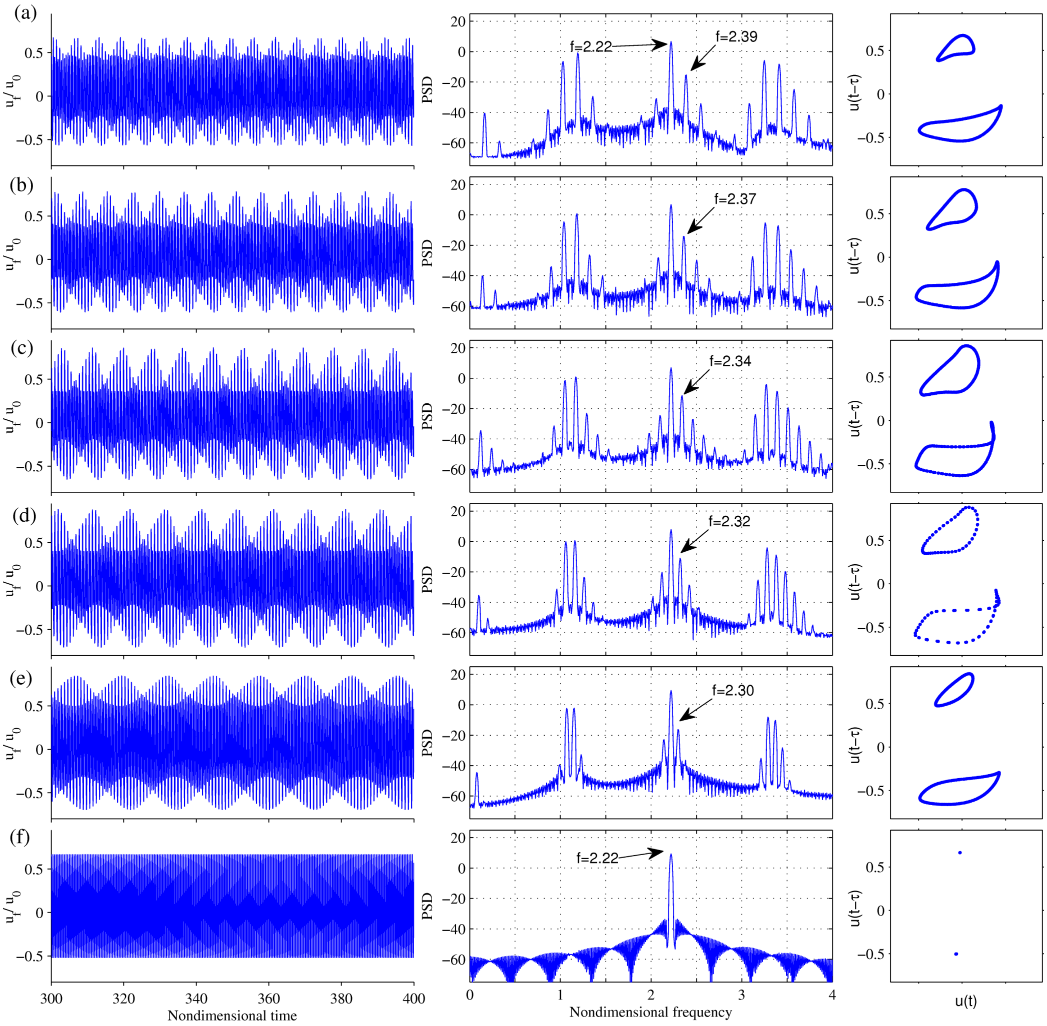

Figure 6.14: Forced response of the system initially on a 2-torus, when it is forced at the dominant characteristic frequency of the 2-torus, $f_f/f_1 = 1$, where $f_1 = 2.22$. Time series, power spectra and Poincaré sections are shown for increasing forcing amplitudes: (a) unforced case, (b) $\epsilon = 0.09$, (c) $\epsilon = 0.18$, (d) $\epsilon = 0.24$, (e) $\epsilon = 0.30$ and (f) $\epsilon = 0.31$.

saddle-node bifurcation to a stable periodic orbit in frame (f). This is the same transition described in §6.4.1.

Synchronization and control of driven and autonomous chaotic oscillators has received much attention in the last two decades [196]. The strength of chaos is indicated by the maximal Lyapunov exponent of the chaotic state. Stronger chaos requires stronger forcing to chaos-destruction (lock-in to a stable periodic

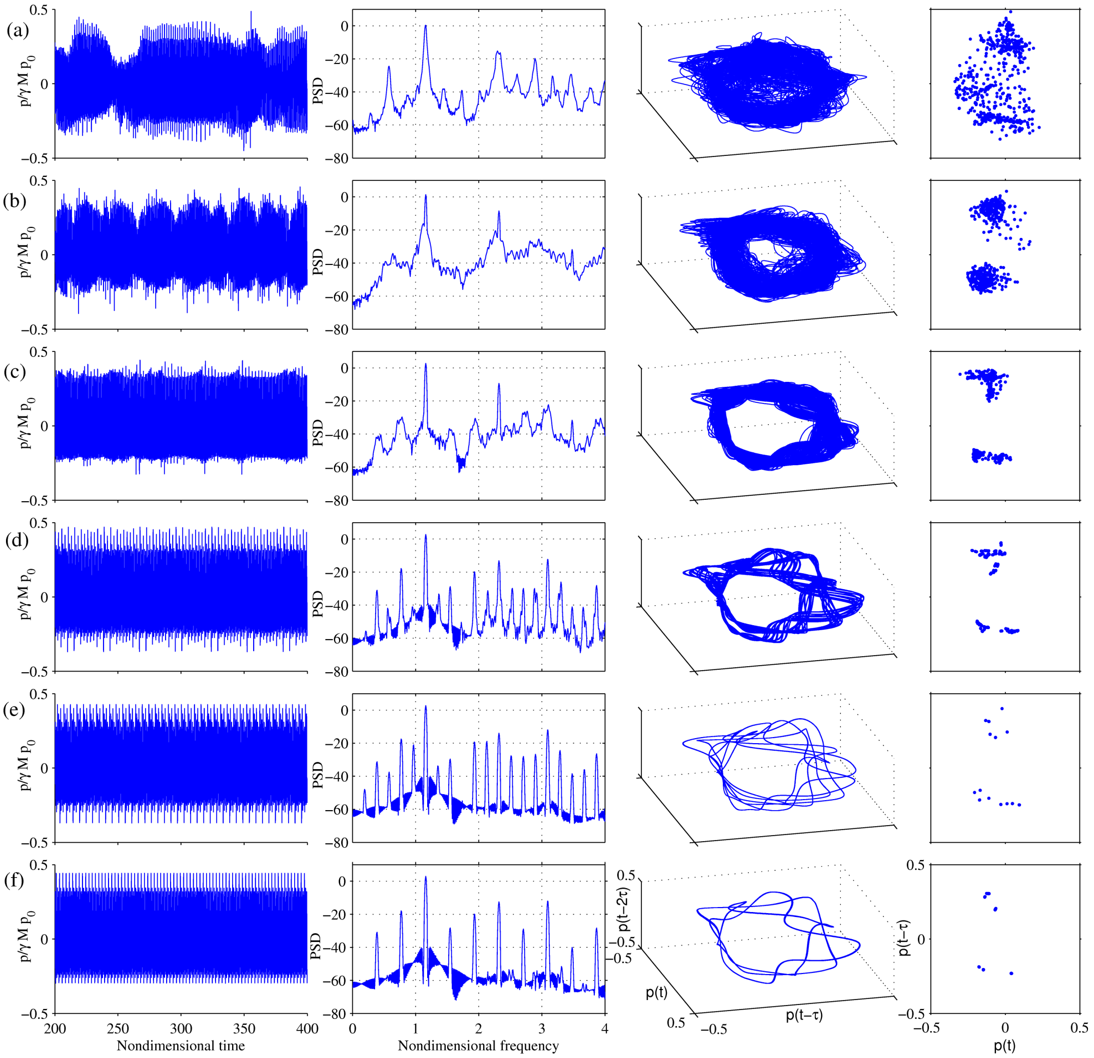

Figure 6.15: Forced response of the system initially on a strange attractor, when it is forced at the dominant frequency in its unforced spectrum, ${}^{f_f}/_{f_n} = 1$, where $f_n = 1.16$. Time series, power spectra, phase portraits and Poincaré sections are shown for increasing forcing amplitudes: (a) unforced case, (b) $\epsilon = 0.09$, (c) $\epsilon = 0.18$, (d) $\epsilon = 0.27$, (e) $\epsilon = 0.30$.

motion). In chapter-5 we characterised some of the strange attractors associated with chaotic oscillations in this system by calculating the Lyapunov exponents and correlation dimensions. This is not done here.

Figure 6.15 shows the response of the system when it is forced at the dominant frequency of the strange attractor, $f_n = 1.16$. As the forcing amplitude is increased, the spectra of the system's response begin to show sharper peaks at discrete frequencies. The time series show the emergence of order and the phase portraits and Poincaré sections show a change in the topology of the attractor. Ultimately, at large forcing amplitudes ($\epsilon \sim 0.30$), the forcing stabilizes a periodic oscillation (period-*3*).

Destruction of chaos may be viewed as the stabilization of one of the infinitely many unstable periodic orbits that comprise the strange attractor [89]. When the forcing amplitude is increased, one (or more) of these unstable periodic orbits are stabilized via a sequence of bifurcations.

6.8 Conclusions

In this chapter a numerical model of a thermoacoustic system with a realistic flame, several acoustic modes and negligible numerical noise is examined with the following objectives: (i) to understand its behaviour by relating it to the behaviour of nonlinear dynamical systems, (ii) to provide 'clean' test cases against which other numerical or experimental results can be campared, and (iii) to investigate the potential of open-loop forcing strategies for suppressions of thermoacoustic oscillations.

It is found that the behaviour of the system is quite elaborate and has the following features: (i) forced period-*1* oscillations have different bifurcations leading up to lock-in and some of these involve transitions to intermittency and chaos; (ii) the critical forcing amplitude required for lock-in depends on two factors: a) whether the forcing frequency is above or below the self-excited frequency, and b) the proximity of the forcing frequency to the self-excited frequency; (iii) the amplitude of self-excited oscillations once the system locks in may be higher or lower than the unforced state, depending on the frequency and amplitude of the forcing. At certain frequencies, even low-amplitude forcing is sufficient to suppress self-excited oscillations to amplitudes that are 80% lower than the amplitude of the unforced state. Therefore, open-loop forcing can be an effective strategy for suppression of thermoacoustic oscillations; (iv) when the locked-in state is forced at increasing amplitudes, two types of behaviour are seen: a) the locked-in state loses stability and transitions to chaos, or b) the forcing leads to multi-stability and mode switching occurs depending on the amplitude of forcing; and (v) forced quasi-periodic and chaotic oscillations lock into periodic oscillations via different bifurcations. Therefore suppressing aperiodic oscillations may be possible by a two-step strategy, first to stabilize the system to a periodic oscillation and then to suppress that periodic oscillation.

In summary, we find that the system has rich dynamical behaviour, similar to recent experiments on a hydrodynamically self-excited jet diffusion flames and low-density jets [88; 179], but previously unreported in the literature on thermoacoustics. The model examined in this study has around 5000 degrees of freedom and consists of 20 coupled oscillators interacting with each other via a nonlinear heat release rate and perturbed by open-loop forcing. The response observed in this study, however, suggests that it behaves similarly to low-dimensional chaotic systems. This implies that a low-order dynamical model of the system may exist that is capable of reproducing the dynamics of the larger system accurately. The pursuit of such a model is attractive because it could provide opportunities to identify the causes of the elaborate nonlinear behaviour, interpret the underlying dynamics and develop and test control strategies to suppress these oscillations, besides making the direct application of well-known results from dynamical systems theory in thermoacoustics possible.

Chapter 7

Conclusions

In this thesis, nonlinear thermoacoustic oscillations of a ducted premixed flame are analysed numerically. The flame is modelled using a nonlinear kinematic model based on the G-equation, the velocity field is governed by continuity and 1-D advection equations, and the acoustics are governed by linearised momentum and energy equations. A Galerkin discretization is used for acoustic pressure and velocity.

The first part of this thesis focuses on deriving analytical criteria for the existence and stability of limit cycles in single-mode thermoacoustic systems. These are used to study the influence of the phase speed of hydrodynamic instabilities on the types of bifurcations in the system.

The second part of this thesis focuses on finding the attractors, bifurcations and routes to chaos in the self-excited system, investigating its transient behaviour and analysing the effect of the number of coupled acoustic modes in the discretization on model's nonlinear behaviour.

The third part of the thesis focuses on studying the response of periodic, quasiperiodic and chaotic oscillations in the self-excited system to external harmonic forcing, relating the response to that of low-dimensional dynamical systems and investigating the potential of open-loop control in thermoacoustic systems.

7.1 Summary of main results

Part 1

In part 1 of the thesis (chapters 3 and 4), assuming the existence of limit cycles, the acoustic momentum and energy equations are used to derive criteria to estimate the amplitudes of limit cycles and their stability for a single-mode thermoacoustic system. These criteria describe how the perturbation energy in thermoacoustic systems is driven by the unsteady heat release and dissipated by the damping. In particular, these criteria show the precise role that the gain and the phase of the flame describing function (FDF) and the damping factor play in determining the growth or decay of perturbation energy, at all amplitudes. It is shown that there exist certain regions where either the gain or the phase is more influential on the perturbation energy, but the combined effect of the gain and the phase has to be considered in order to predict accurately the growth or decay of the perturbation energy. These criteria are also used to find the types of bifurcation in this sytem, the regions of multi-stability and the minimum amplitude of excitation required to trigger a single-mode thermoacoustic system into limit cycle oscillations. The time domain calculations of a single-mode system agree well with the amplitude estimated by these criteria.

The phase speed of velocity perturbations are shown to be crucial for prediction of nonlinear dynamics of thermoacoustic systems. Therefore a detailed numerical study is performed in collaboration with Santosh Hemchandra (Indian Institute of Science, Bangalore) to find the phase speed of velocity perturbations for a harmonically forced laminar premixed flame from forced Direct Numerical Simulation (DNS) of a 2-D premixed flame. The DNS show that the perturbation velocity can be simplified to a travelling wave with a frequency-dependent phase speed. This frequency-dependent phase speed is shown to cause large variations in the gain and phase of the FDF as the oscillation amplitude increases, which are responsible for the existence of multiple limit cycles and subcritical bifurcations in thermoacoustic systems. This is an advance on current models that assume a constant phase speed equal to the mean flow and therefore predict that the system can have only one stable state.

Part 2

In this part of the thesis (chapter 5), the self-excited system is simulated in the time domain and its behaviour is analysed using nonlinear time series analysis and techniques from dynamical systems theory. This study is motivated by recent experiments by Kabiraj *et al.* that show the elaborate nonlinear behaviour of self-excited ducted premixed flames [56; 64; 65].

These simulations show that the system has not only period-*1* oscillations (simple limit cycles) but also period-*2*, period-k, quasi-periodic and chaotic oscillations. The transitions to these types of oscillation are via subcritical or supercritical Hopf, Neimark-Sacker and period-doubling bifurcations. Analysis of the transient behaviour shows that the trajectory of the system is elaborate and involves transient attraction and repulsion by one or more unstable attractors before the system tends towards a stable state. Therefore the unstable attractors strongly influence the system's pathways. Two routes to chaos are established in this system: the period-doubling route and the Ruelle-Takens-Newhouse route. Such elaborate nonlinear behaviour is more likely to be seen in thermoacoustic systems with the following properties: (i) systems with short flames than long flames, because short flames have sharper cusps at lower amplitudes of oscillation, (ii) systems where the flame is close to the end of the duct, because the higher modes have relatively larger amplitudes near the ends of the duct, and (iii) systems with long ducts than short ducts, because the higher modes are more strongly damped in short ducts.

The influence of the number of coupled acoustic modes on the nonlinear behaviour of the system is analysed. It is shown that the single mode system, which gives the same results as a describing function approach, fails to capture the period-2, period-k, quasi-periodic and chaotic oscillations, or the bifurcations and multi-stability seen in the multi-modal case. Furthermore, in regions of parameter space where only period-1 oscillations exist, it underpredicts the oscillation amplitude. The heat release rate is highly nonlinear but, because the acoustic velocity and pressure are assumed to be harmonic, the higher and sub-harmonics of the heat release rate cannot interact with acoustics. The multi-modal simulations show rich behaviour because: (i) the nonlinear unsteady heat release rate results in nonharmonic velocity perturbations that, in turn, cause elaborate flame wrinkling and (ii) more than one mode may be linearly unstable and the energy transfer between them due to nonlinear interactions affects the transient and steady state behaviour of the system.

Instantaneous flame images reveal that the wrinkles on the flame surface and pinch off of flame pockets are regular for periodic oscillations, while they are irregular and have multiple time and length scales for aperiodic oscillations. This is because the magnitude and shape of the acoustic velocity at the flame position, which creates wrinkles by perturbing the flame surface, are different for different types of oscillation. The source of nonlinearity is the flame, but such nonharmonic velocity waveforms are possible because the acoustics responds at several frequencies.

This chapter shows the influence of cusp formation, their destruction by flame propagation normal to itself, and pinch-off and rapid burning of pockets of reactants in generating a heat release rate that is a highly nonlinear function of the velocity perturbations. It also shows that, for a given acoustic model of the duct, several modes are required to capture the influence of this highly nonlinear unsteady heat release rate on the acoustics and the interactions between the acoustic modes via the unsteady heat release rate. Both of these are required to simulate the rich dynamics seen in experiments. The methods from dynamical systems theory and nonlinear time series analysis illustrated in this chapter are superior to the describing function approach in the frequency domain and time domain analysis currently used in nonlinear thermoacoustics. The work in this chapter complements recent experiments by Kabiraj *et al.* [56; 64] by providing a reduced order model of a system that captures much of the elaborate nonlinear behaviour of ducted premixed flames observed in the laboratory.

Part 3

In this part of the thesis (chapter 6) the forced response of the self-excited ducted premixed flame is investigated with the following objectives: (i) to understand its behaviour by relating it to the behaviour of nonlinear dynamical systems, (ii) to provide 'clean' test cases against which other numerical or experimental results can be compared, and (iii) to investigate the potential of open-loop forcing strategies for suppression of thermoacoustic oscillations.

It is found that the behaviour of the system is quite elaborate. Forced period-*1* oscillations have different bifurcations leading up to lock-in and some of these involve transitions to intermittency and chaos. The critical forcing amplitude required for lock-in depends on two factors: a) whether the forcing frequency is above or below the self-excited frequency, and b) the proximity of the forcing frequency to the self-excited frequency. The amplitude of oscillations once the system just locks into the forcing may be higher or lower than the unforced state, depending on the frequency and amplitude of the forcing. At certain frequencies, even low-amplitude forcing is sufficient to suppress self-excited oscillations to amplitudes that are 90% lower than the amplitude of the unforced state. Therefore, open-loop forcing can be an effective strategy for the suppression of thermoacoustic oscillations.

When the locked-in state is forced at increasing amplitudes, two types of behaviour are seen: a) the locked-in state loses stability and transitions to chaos, or b) the forcing leads to multi-stability and mode switching occurs depending on the amplitude of forcing. Forced quasi-periodic and chaotic oscillations lock into periodic oscillations via different bifurcations. Therefore, suppressing aperiodic oscillations may be possible by a two-step strategy, first to stabilize the system to a periodic oscillation and then to suppress that periodic oscillation.

This chapter shows that the forced response of this self-excited system has rich dynamical behaviour, similar to recent experiments in a hydrodynamically self-excited jet diffusion flame [179], but previously unreported in the literature on thermoacoustics. The response of this system is in close correspondence with low-dimensional chaotic systems. The results of this chapter show that open-loop forcing could be a successful means of suppressing thermoacoustic oscillations.

7.2 Future work

The flame model used in this thesis is general and can be applied to more sophisticated geometries than a simple 2-D tent flame, including M-flames and multiple flames adjacent to each other to model flame-flame interactions. The acoustic model, however, is simple. The wave approach is more accurate and versatile in modelling linear acoustics taking into account the effect of temperature changes, area changes, sophisticated boundary conditions and annular geometries [75; 197; 198]. Schuermans has shown that a state space representation of a thermoacoustic network model is a powerful and numerically efficient way to study the time evolution of thermoacoustic systems [199]. Recently, Illingworth has derived state space models in the time domain from a low-order thermoacoustic network model and this has been incorporated into the level set model of the flame by Waugh [60]. Using this upgraded version of the coupled flame-acoustic code, the behaviour of more realistic thermoacoustic systems could be investigated, for example, the dump combustor developed and studied experimentally by Balachandran [200].

In chapter 4 the DNS of a laminar premixed flame showed that a travelling wave model with a frequency-dependent phase speed accurately described the perturbation velocity field for a forced premixed flame. This was extended to the self-excited case using the 1-D advection equation. In this model the base flow is uniform. This can be made more realistic in one of two ways: (i) solving the advection equation with a non-uniform base flow, or (ii) solving the advection equation for vorticity perturbations and then obtaining the velocity field from the vorticity field. These alternatives, however, are likely to be computationally more expensive than the simple 1-D model.

Direct time-marching of the self-excited system is time-consuming. Recent work by Waugh [60] has shown how continuation methods are efficient at finding Hopf, Neimark-Sacker and period-doubling bifurcations and tracking periodic oscillations. Tracking aperiodic oscillations, however, is not possible using continuation. Therefore a combined approach of using continuation methods to find limit cycles and their bifurcations, and using time evolution and nonlinear time series analysis to find and characterize aperiodic oscillations, would be an efficient means of fully characterizing the behaviour of thermoacoustic systems. As a first step, this combined approach could be applied to a conical premixed flame in a duct, with a state space model of more realistic acoustics, to make a *quantitative* comparison of the bifurcations, quasi-periodic oscillations and routes to chaos seen in experiments by Kabiraj [56; 64]. Such a study would validate this model, which can then be extended to more realistic systems.

In chapter 5 the instantaneous flame images during elaborate nonlinear oscillations showed close resemblance to experimental images in experiments by Kabiraj *et al.* on a similar system. Kabiraj *et al.* have observed intermittency due to repeated flame lift-off and reattachment in a subsequent study on the same system [65]. In the current model the flame base can move due to flashback using the boundary condition proposed by Dowling [73], but cannot lift-off. Incorporating a model for flame lift-off would be a step towards simulating more realistic flame behaviour.

Chapter 6 showed that open-loop forcing at certain frequencies is an effective way to suppress the self-excited oscillations of the system. A similar conclusion was drawn by Hallberg and Strykowski from experiments on low-density jets [91]. Furthermore, control of chaos using small periodic perturbations is well-known in the literature in the synchronization of chaos [196]. Open-loop forcing of thermoacoustic systems, however, has received little attention, both in theory and practice. Investigating the potential of open-loop forcing on more realistic models and lab-scale experiments will help determine the feasibility of this technique in practical applications.

Chapter 6 also showed that the model behaves similarly to low-dimensional chaotic dynamical systems. In particular, the bifurcations to lock-in, the system response at lock-in, the route to chaos due to large-amplitude forcing and the transitions from aperiodic to periodic oscillations were shown to be either identical or similar to those seen in low-dimensional nonlinear dynamical systems. Li and Juniper show the close correspondence between their experiments and the behaviour of a forced van der Pol oscillator [88]. Several infinite-dimensional systems have been modelled reasonably accurately using low-dimensional nonlinear systems [89]. This suggests that a low-order dynamical model of the system may exist that is capable of reproducing the dynamics of the larger system accurately. The pursuit of such a model is attractive because it could provide opportunities to identify the causes of the elaborate nonlinear behaviour and interpret the underlying dynamics, besides making the direct application of results from dynamical systems theory in thermoacoustics possible. Furthermore, identifying a low-dimensional nonlinear dynamical system will provide a reliable model that could be used to develop and test control strategies.

References

[1] A. P. Dowling and A. S. Morgans. Feedback control of combustion oscillations. *Annual Review of Fluid Mechanics*, 37:151–182, 2005. 1, 2, 38, 111

[2] A. P. Dowling and J. E. Ffowcs Williams. *Sound and Sources of Sound*. Ellis Horwood, 1983. 1

[3] J. W. S. Rayleigh. *The theory of sound Vol. II*. New York: Dover, 1945. 1, 3, 38

[4] T. Lieuwen, H. Torres, C. Johnson, and B. T. Zinn. A mechanism of combustion instability in lean premixed gas turbine combustors. *Journal of Engineering for Gas Turbines and Power*, 123(1):182–189, 2001. 1

[5] K. R. McManus, T. Poinsot, and S. M. Candel. A review of active control of combustion instabilities. *Progress in energy and combustion science*, 19(1):1–29, 1993. 2, 111

[6] S. J. Illingworth, A. S. Morgans, and C. W. Rowley. Feedback control of flow resonances using balanced reduced-order models. *Journal of Sound and Vibration*, 330(8):1567–1581, 2011. 2

[7] A. S. Morgans and A. P. Dowling. Model-based control of combustion instabilities. *Journal of Sound and Vibration*, 299(1):261–282, 2007. 2, 111

[8] H. C. Mongia, T. J. Held, G. C. Hsiao, and R. P. Pandalai. Challenges and progress in controlling dynamics in gas turbine combustors. *Journal of Propulsion and Power*, 19(5):822–829, 2003. 2

[9] J. M. Cohen and A. Banaszuk. Factors affecting the control of unstable combustors. *Journal of propulsion and power*, 19(5):811–821, 2003. 2

[10] S. M. Candel. Combustion dynamics and control: progress and challenges. *Proceedings of the Combustion Institute*, 29(1):1–28, 2002. 2, 3, 112

[11] W. Polifke. Thermoacoustic system modelling and stability analysis: conventional approaches. In *Workshop on Advanced Instability Methods, IIT Madras, Chennai, India*, 2009. 2, 14

[12] T. C. Lieuwen. *Unsteady Combustor Physics*. Cambridge University Press, 2012. 3, 5

[13] T. C. Lieuwen. Modeling premixed combustion-acoustic wave interactions: A review. *Journal of Propulsion and Power*, 19(5):765–781, 2003. 3, 4, 7

[14] Y. Huang and V. Yang. Dynamics and stability of lean-premixed swirl-stabilized combustion. *Progress in Energy and Combustion Science*, 35(4):293–364, 2009. 3

[15] A. A. Putnam and W. R. Dennis. Survey of organ-pipe oscillations in combustion systems. *The Journal of the Acoustical Society of America*, 28:246, 1956. 3

[16] B. T. Chu and L. S. G. Kovasznay. Non-linear interactions in a viscous heat-conducting compressible gas. *Journal of Fluid Mechanics*, 3:494–514, 1958. 3, 4, 56

[17] F. Nicoud and T. Poinsot. Thermoacoustic instabilities: Should the rayleigh criterion be extended to include entropy changes? *Combustion and Flame*, 142(1):153–159, 2005. 3

[18] F. E. C. Culick. Combustion instabilities in liquid-fueled propulsion systems, paper no. 1. In *AGARD Conference Proceedings*, number 450, 1988. 3, 4, 7, 10, 15, 17, 18

[19] B. T. Zinn. A theoretical study of nonlinear combustion instability in liquid-propellant rocket engines. *AIAA journal*, 6(10):1966–1972, 1968. 4

[20] F. E. C. Culick. Nonlinear behaviour of acoustic waves in combustion chambers - 1. *Acta Astronautica*, 3(9-10):715 – 734, 1976. 4, 18, 38

[21] J. N. Levine and J. D. Baum. A numerical study of nonlinear instability phenomena in solid rocketmotors. *AIAA Journal*, 21(4):557–564, 1983. 4, 11

[22] A. P. Dowling. The calculation of thermoacoustic oscillations. *Journal of Sound and Vibration*, 180(4):557–581, 1995. 4, 15

[23] F. E. Marble and S. M. Candel. Acoustic disturbance from gas nonuniformities convected through a nozzle. *Journal of Sound and Vibration*, 55(2):225–243, 1977. 4

[24] T. C. Lieuwen, V. Yang, and F. K. Lu. *Combustion instabilities in gas turbine engines: operational experience, fundamental mechanisms and modeling*. American Institute of Aeronautics and Astronautics, 2005. 5

[25] B. D. Bellows. *Characterization of nonlinear heat release-acoustic interactions in gas turbine combustors*. PhD thesis, Georgia Institute of Technology, 2006. 5, 6, 20, 125, 127

[26] S. Hemchandra. *Dyamics of turbulent premixed flames in acoustic fields*. PhD thesis, Georgia Institute of Technology, 2009. 5, 23, 31

[27] A. P. Dowling. Nonlinear self-excited oscillations of a ducted flame. *Journal of Fluid Mechanics*, 346(1):271–290, 1997. 5, 7, 16, 27, 29, 76

[28] A. P. Kelley and C. K. Law. Nonlinear effects in the extraction of laminar flame speeds from expanding spherical flames. *Combustion and Flame*, 156(9):1844–1851, 2009. 5

[29] N. Karimi, M. J. Brear, S.-H. Jin, and J. P. Monty. Linear and non-linear forced response of a conical, ducted, laminar premixed flame. *Combustion and Flame*, 156(11):2201 – 2212, 2009. 7, 37, 40, 57, 61, 64, 66, 67

[30] T. Schuller, D. Durox, and S. Candel. A unified model for the prediction of laminar flame transfer functions: comparisons between conical and v-flame

dynamics. *Combustion and Flame*, 134(1-2):21 – 34, 2003. 7, 29, 36, 40, 58, 64, 65

[31] Preetham, S. Hemchandra, and T. C. Lieuwen. Dynamics of laminar premixed flames forced by harmonic velocity disturbances. *Journal of Propulsion and Power*, 394(6):51–72, 2008. 7, 8, 29, 36, 40, 41, 42, 53, 58, 61, 63, 67, 68, 73

[32] Shreekrishna, S. Hemchandra, and T. Lieuwen. Premixed flame response to equivalence ratio perturbations. *Combustion Theory and Modelling*, 14(5):681–714, 2010. 7, 30, 31, 61

[33] M. W. Beckstead and R. Jensen. Non-linear mechanisms of solid propellant combustion instability. In *24th JANNAF Combustion Meeting, CPIA Publication*, volume 476, pages 27–40, 1973. 7

[34] S. Strogatz. *Nonlinear dynamics and chaos: with applications to physics, biology, chemistry and engineering*. Perseus Books Group, 2001. 8, 18, 78, 114

[35] J. Guckenheimer and P. Holmes. *Nonlinear oscillations, dynamical systems, and bifurcations of vector fields*, volume 42. Springer-Verlag New York, 1983. 8, 12

[36] C. C. Jahnke and F. E. C. Culick. Application of dynamical systems theory to nonlinear combustion instabilities. *Journal of Propulsion and Power*, 10(4):508–517, 1994. 8, 13, 18, 19, 76

[37] T. C. Lieuwen. Experimental investigation of limit-cycle oscillations in an unstable gas turbine combustor. *Journal of Propulsion and Power*, 18(1):61–67, 2002. 8, 10, 11

[38] N. Ananthkrishnan, S. Deo, and F. E. C. Culick. Reduced-order modeling and dynamics of nonlinear acoustic waves in a combustion chamber. *Combustion Science and Technology*, 177(2):221–248, 2005. 8, 19, 47

[39] G. Campa and M. P. Juniper. Obtaining bifurcation diagrams with a thermoacoustic network model. In *ASME Turbo Expo*, 2012. 9

[40] F. E. C. Culick. Non-linear growth and limiting amplitude of acoustic oscillations in combustion chambers. *Combustion Science and Technology*, 3(1):1–16, 1971. 10, 18, 76

[41] J. D. Sterling and E. E. Zukoski. Nonlinear dynamics of laboratory combustor pressure oscillations. *Combustion science and technology*, 77(4-6):225–238, 1991. 10, 12

[42] I. Matveev. *Thermo-acoustic instabilities in the Rijke tube: Experiments and modeling*. PhD thesis, California Institute of Technology, 2003. 10, 11, 29

[43] B. D. Bellows, A. Hreiz, and T. C. Lieuwen. Nonlinear interactions between forced and self-excited acoustic oscillations in premixed combustor. *Journal of Propulsion and Power*, 24(3):628–631, 2008. 10, 20, 111

[44] J. P. Moeck. *Analysis, modeling, and control of thermoacoustic instabilities*. PhD thesis, Technische Universitat Berlin, 2010. 10, 11

[45] M. E. Lores and B. T. Zinn. Nonlinear longitudinal combustion instability in rocket motors. *Combustion Science and Technology*, 7(6):245–256, 1973. 10

[46] F. E. C. Culick, V. Burnley, and G. Swenson. Pulsed instabilities in solid-propellant rockets. *Journal of Propulsion and Power*, 11(4):657–665, 1995. 10, 70

[47] J. M. Wicker, W. D. Greene, S. Kim, and V. Yang. Triggering of longitudinal combustion instabilities in rocket motors - nonlinear combustion response. *Journal of Propulsion and Power*, 12(6):1148–1156, 1996. 11, 12, 70

[48] K. Balasubramanian and R. I. Sujith. Thermoacoustic instability in a rijke tube: Non-normality and nonlinearity. *Physics of Fluids*, 20(4):44103–44103, 2008. 11

[49] P. Subramanian, S. Mariappan, R. I. Sujith, and P. Wahi. Bifurcation analysis of thermoacoustic instability in a horizontal rijke tube. *International Journal of Spray and Combustion Dynamics*, 2(4):325–355, 2010. 11, 13, 29, 35

[50] M. P. Juniper. Triggering in the horizontal Rijke tube: non-normality, transient growth and bypass transition. *J. Fluid Mech.*, 667:272–308, 2011. 11, 12, 29, 46, 94

[51] S. Mariappan and R. I. Sujith. Modelling nonlinear thermoacoustic instability in an electrically heated rijke tube. *Journal of Fluid Mechanics*, 680(1):511–533, 2011. 11, 19

[52] K. Balasubramanian and R. I. Sujith. Non-normality and nonlinearity in combustion-acoustic interaction in diffusion flames. *Journal of Fluid Mechanics*, 594:29, 2008. 11

[53] L. Magri, K. Balasubramanian, R. I. Sujith, and M. P. Juniper. Non-normality in combustion-acoustic interaction in diffusion flames: a critical revision. *Journal of Fluid Mechanics*, 733:681–683, 2013. 11

[54] M. P. Juniper. Triggering in thermoacoustics. *International Journal of Spray and Combustion Dynamics*, 4(3):217–238, 2012. 11, 18

[55] N. Noiray, D. Durox, T. Schuller, and S. Candel. A unified framework for nonlinear combustion instability analysis based on the flame describing function. *Journal of Fluid Mechanics*, 615:139–167, 2008. 11, 16, 35, 40, 53, 58, 68, 76

[56] L. Kabiraj and R. I. Sujith. Bifurcations of self-excited ducted laminar premixed flames. *Journal of Engineering for Gas Turbines and Power*, 134(031502), 2012. 11, 12, 13, 21, 76, 112, 140, 141, 144

[57] F. Boudy, D. Durox, T. Schuller, and S. Candel. Nonlinear flame dynamics and mode triggering in a multiple flame combustor. *Proceedings of the Combustion Institute*, 33(1):1121 – 1128, 2011. 11, 58, 71

[58] I. C. Waugh and M. P. Juniper. Triggering in a thermoacoustic system with stochastic noise. *International Journal of Spray and Combustion Dynamics*, 3(4):225–242, 2011. 12, 94

[59] V. Jegadeesan and R. I. Sujith. Experimental investigation of noise induced triggering in thermoacoustic systems. *Proceedings of the Combustion Institute*, 34(2):3175–3183, 2013. 12

[60] I. C. Waugh. *Methods for analysis of nonlinear thermoacoustic systems*. PhD thesis, University of Cambridge, 2013. 12, 19, 23, 31, 106, 108, 143

[61] J. M. T. Thompson and H. B. Stewart. *Nonlinear dynamics and chaos*. John Wiley and Sons, Ltd., 2002. 12, 78, 99, 114

[62] J. D. Sterling. Nonlinear analysis and modelling of combustion instabilities in a laboratory combustor. *Combustion Science and Technology*, 89(1-4):167–179, 1993. 13, 76

[63] S Lei and A Turan. Nonlinear/chaotic behaviour in thermo-acoustic instability. *Combustion Theory and Modelling*, 13(3):541–557, 2009. 13, 76

[64] L. Kabiraj, A. Saurabh, P. Wahi, and R. I. Sujith. Route to chaos for combustion instability in ducted laminar premixed flames. *Chaos*, 22(2):023129–023129, 2012. 13, 21, 76, 99, 107, 112, 140, 141, 144

[65] L. Kabiraj and R. I. Sujith. Nonlinear self-excited thermoacoustic oscillations: intermittency and flame blowout. *Journal of Fluid Mechanics*, 713:376–397, December 2012. 13, 31, 76, 92, 106, 112, 140, 144

[66] H. Gotoda, H. Nikimoto, T. Miyano, and S. Tachibana. Dynamic properties of combustion instability in a lean premixed gas-turbine combustor. *Chaos*, 21(1):013124–013124, 2011. 13, 21, 76

[67] H. Gotoda, M. Amano, T. Miyano, T. Ikawa, K. Maki, and S. Tachibana. Characterization of complexities in combustion instability in a lean premixed gas-turbine model combustor. *Chaos*, 22(4):043128–043128, 2012. 13, 76

[68] F. A. Williams. *Turbulent Combustion in The Mathematics of Combustion (ed J. D. Buckmaster)*. Society for Industrial and Applied Mathematics, 1985, 97–131. 14, 29, 30

[69] S. W. Rienstra and A. Hirschberg. *An introduction to acoustics*. 2001. 15

[70] A. P. Dowling and S. R. Stow. Acoustic analysis of gas turbine combustors. *Journal of Propulsion and Power*, 19(5):751–764, 2003. 15, 19

[71] T. Poinsot and D. Veynante. *Theoretical and numerical combustion*. RT Edwards Incorporated, 2005. 15

[72] M. M. S. Natanzon. *Combustion instability*, volume 222. American Institute of Aeronautics and Astronautics, 1999. 16

[73] A. P. Dowling. A kinematic model of a ducted flame. *Journal of Fluid Mechanics*, 394(1):51–72, 1999. 16, 29, 31, 144

[74] P. Subramanian, V. Gupta, B. Tulsyan, and R. I. Sujith. Can describing function technique predict bifurcations in thermoacoustic systems? *16th AIAA/CEAS Aeroacoustics Conference*, 2010. 16

[75] S. R. Stow and A. P. Dowling. A time-domain network model for nonlinear thermoacoustic oscillations. *Journal of engineering for gas turbines and power*, 131(3), 2009. 17, 76, 143

[76] O. Graham and A. P. Dowling. Low-order modelling of ducted flames with temporally varying equivalence ratio in realistic geometries. In *ASME Turbo Expo ASME GT2011-45255, 2011*, 2011. 17, 29

[77] O. Graham and A. P. Dowling. Low-order modelling of the response of ducted flames in annular geometries. In *Proceedings of the ASME Turbo Expo*, volume 2, pages 479–490, 2012. 17

[78] E. A. Powell and B. T. Zinn. Application of the galerkin method in the solution of combustion-instability problems. Technical report, NASA, 1968. 17

[79] G. Ghirardo and M. P. Juniper. Azimuthal instabilities in annular combustors: standing and spinning modes. *Proceedings of the Royal Society A: Mathematical, Physical and Engineering Science*, 469(2157), 2013. 18

[80] E. Awad and F. E. C. Culick. On the existence and stability of limit cycles. for longitudinal acoustic modes in a combustion chamber. *Combustion Science and Technology*, 46(3-6):195–222, 1986. 18, 19

[81] J. D. Baum, J. N. Levine, and R. L. Lovine. Pulsed instability in rocket motors-a comparison between predictions and experiments. *Journal of Propulsion and Power*, 4(4):308–316, 1988. 18

[82] L. G. Paparizos and F. E. C. Culick. The two-mode approximation to nonlinear acoustics in combustion chambers i. exact solution for second order acoustics. *Combustion Science and Technology*, 65(1-3):39–65, 1989. 18, 19

[83] V. Yang, S. I. Kim, and F. E. C. Culick. Triggering of longitudinal pressure oscillations in combustion chambers. i: Nonlinear gasdynamics. *Combustion Science and Technology*, 72(4-6):183–214, 1990. 18

[84] J. J. Anagnost and C. A. Desoer. An elementary proof of the Routh-Hurwitz stability criterion. *Circuits, Systems and Signal Processing*, 10(1):101–114, 1991. 19

[85] I. C. Waugh, S. J. Illingworth, and M. P. Juniper. Matrix-free continuation of limit cycles for bifurcation analysis of large thermoacoustic systems. *Journal of Computational Physics*, 2013. 19

[86] T. C. Lieuwen and Y. Neumeier. Nonlinear pressure-heat release transfer function measurements in a premixed combustor. *Proceedings of the Combustion Institute*, 29(1):99–105, 2002. 20

[87] R. K. Prasanth, A. M. Annaswamy, J. P. Hathout, and A. F. Ghoniem. When do open-loop strategies for combustion control work? *Journal of Propulsion and Power*, 18(3):658–668, 2002. 20

[88] L. K. B. Li and M. P. Juniper. Lock-in and quasiperiodicity in a forced hydrodynamically self-excited jet. *Journal of Fluid Mechanics*, 726:624–655, 2013. 20, 92, 111, 112, 116, 121, 137, 144

[89] A. Pikovsky, M. Rosenblum, and J. Kurths. *Synchronization: a universal concept in nonlinear sciences*, volume 12. Cambridge University Press, 2003. 20, 111, 112, 113, 114, 118, 121, 122, 126, 128, 131, 133, 136, 144

[90] B. Pier. Open-loop control of absolutely unstable domains. *Proceedings of the Royal Society of London. Series A: Mathematical, Physical and Engineering Sciences*, 459(2033):1105–1115, 2003. 21, 111

[91] M. P. Hallberg and P. J. Strykowski. Open-loop control of fully nonlinear self-excited oscillations. *Physics of Fluids*, 20:041703, 2008. 21, 144

[92] Preetham, S. K. Thumuluru, H. Santosh, and T. Lieuwen. Linear response of premixed flames to flow oscillations: unsteady stretch effects. *Journal of Propulsion and Power*, 26(3):524–532, 2007. 27

[93] L. D. Landau and E. M. Lifshitz. *Fluid Mechanics*. Pergamon Press, 1959. 29

[94] Priya Subramanian and R. I. Sujith. Non-normality and internal flame dynamics in premixed flame-acoustic interaction. *Journal of Fluid Mechanics*, 679:315–342, 2011. 29

[95] T. Schuller, S. Ducruix, D. Durox, and S. Candel. Modeling tools for the prediction of premixed flame transfer functions. *Proceedings of the Combustion Institute*, 29(1):107–113, 2002. 29, 58, 64

[96] Santosh H., Preetham, and T. C. Lieuwen. Response of turbulent premixed flames to harmonic acoustic forcing. *Proceedings of the Combustion Institute*, 31(1):1427–1434, 2007. 29

[97] S. Hemchandra, N. Peters, and T. Lieuwen. Heat release response of acoustically forced turbulent premixed flames - role of kinematic restoration. *Proceedings of the Combustion Institute*, 33(1):1609–1617, 2011. 29

[98] S. Ducruix, D. Durox, and S. Candel. Theoretical and experimental determination of the flame transfer function of a laminar premixed flame. *Proceedings of the Combustion Institute*, 28(1):765–773, 2000. 29, 36, 37, 66

[99] D. H. Shin, D. V. Plaks, T. Lieuwen, U. M. Mondragon, C. T. Brown, and V. G. McDonell. Dynamics of a longitudinally forced, bluff body stabilized flame. *Journal of Propulsion and Power*, 27(1):105–116, 2011. 29, 57, 64

[100] T. C. Lieuwen. Nonlinear kinematic response of premixed flames to harmonic velocity disturbances. *Proceedings of the Combustion Institute*, 30(2):1725 – 1732, 2005. 29, 37, 40, 42, 68, 87

[101] G. S. Jiang and D. Peng. Weighted ENO schemes for Hamilton-Jacobi equations. *SIAM Journal of Scientific Computing*, 21(6):2126–2143, 2000. 31

[102] S. Gottlieb and C. Shu. Total variation diminishing Runge-Kutta schemes. *Mathematics of Computation*, 67(221):73–86, 1998. 31

[103] D. Peng. A PDE-based fast local level set method. *Journal of Computational Physics*, 155(2):410–438, 1999. 31

[104] P. Smereka. The numerical approximation of a delta function with application to level set methods. *Journal of Computational Physics*, 211(1):77–90, 2006. 32

[105] M. Oberlack and A. F. Cheviakov. Higher-order symmetries and conservation laws of the G-equation for premixed combustion and resulting numerical schemes. *Journal of Engineering Mathematics*, 66(1-3):121–140, 2010. 32

[106] M. Fleifil, A. M. Annaswamy, Z. Ghoneim, and A. Ghoneim. Response of a laminar premixed flame to flow oscillations: a kinematic model and thermoacoustic instability results. *Combustion and Flame*, 106:487–510, 1996. 36

[107] F. Baillot, D. Durox, and R. Prud'homme. Experimental and theoretical study of a premixed flame. *Combustion and Flame*, 88(2):149 – 168, 1992. 36, 37, 57, 64, 66

[108] F. Baillot, A. Bourehla, and D. Durox. The characteristics method and cusped flame fronts. *Combustion Science and Technology*, 112:327–350, 1996. 36

[109] A. Cuquel, D. Durox, and T. Schuller. Theoretical and experimental determination of the flame transfer function of confined premixed conical flames. In *7th Mediterranean Combustion Symposium*, 2011. 36, 58, 64

[110] A. Michalke. Instability of a compressible circular free jet with consideration of the influence of the jet boundary thickness. Technical report, NASA 75190, 1971. 36

[111] G. Abu-Orf and R. S. Cant. Reaction rate modelling for premixed turbulent methane-air flames. *Proceedings of the Joint Meeting of Spanish, Portuguese, Swedish and British Sections of the Combustion Institute*, 1996. 37

[112] J. W. S. Rayleigh. The explanation of certain acoustical phenomena. *Nature*, 18:319–321, 1878. 38

[113] A. A. Putnam and W. R. Dennis. Burner oscillations of the gauze-tone type. *Journal of the Acoustical Society of America*, 5:716–725, 1954. 38

[114] B. T. Chu. Stability of systems containing a heat source: the Rayleigh criterion. Technical report, NACA, 1956. 38

[115] D. Durox, T. Schuller, N. Noiray, and S. Candel. Experimental analysis of nonlinear flame transfer functions of different flame geometries. *Proceedings of the Combustion Institute*, 32(1):1391 – 1398, 2009. 40, 57, 64, 68

[116] W. Polifke and C. Lawn. On the low-frequency limit of flame transfer functions. *Combustion and Flame*, 151(3):437–451, 2007. 41

[117] J. Z. Wu, A. D. Vakili, and J. M. Wu. Review of the physics of enhancing vortex lift by unsteady excitation. *Progress in Aerospace Sciences*, 28(2):73 – 131, 1991. 56

[118] K. McManus, U. Vandsburger, and C. Bowman. Combustor performance enhancement through direct shear layer excitation. *Combustion and Flame*, 82(1):75–92, 1990. 56

[119] J. U. Schluter. Large-eddy simulations of combustion instability by static turbulence control. Technical report, Center for Turbulence Research Annual Research Briefs, 2001. 56

[120] D. Wee, S. Park, T. Yi, A. M. Annaswamy, and A. F. Ghoniem. Reduced order modeling of reacting shear flow. In *40th AIAA Aerospace Sciences Meeting and Exhibit*, 2002. 56

[121] L. Boyer and J. Quinard. On the dynamics of anchored flames. *Combustion and Flame*, 82(1):51 – 65, 1990. 57, 64, 66

[122] D. H. Ferguson, D. H. Lee, T. Lieuwen, and G. A. Richards. Velocity field measurements in an oscillating bunsen flame. In *Proceedings of the 2005 Joint States Meeting of the Combustion Institute*, 2005. 57

[123] A. Birbaud, D. Durox, and S. Candel. Upstream flow dynamics of a laminar premixed conical flame submitted to acoustic modulations. *Combustion and Flame*, 146(3):541 – 552, 2006. 57, 63, 64, 66

[124] A. L. Birbaud, D. Durox, S. Ducruix, and S. Candel. Dynamics of free jets submitted to upstream acoustic modulations. *Physics of Fluids*, 19(1):013602, 2007. 57

[125] D. Durox, T. Schuller, and S. Candel. Combustion dynamics of inverted conical flames. *Proceedings of the Combustion Institute*, 30(2):1717–1724, 2005. 57, 64, 66, 81

[126] V. N. Kornilov, K. R. A. M. Schreel, and L. P. H. de Goey. Experimental assessment of the acoustic response of laminar premixed bunsen flames. *Proceedings of the Combustion Institute*, 31(1):1239 – 1246, 2007. 57, 61

[127] V. N. Kornilov, R. Rook, J. H. M. ten Thije Boonkkamp, and L. P. H. de Goey. Experimental and numerical investigation of the acoustic response of multi-slit bunsen burners. *Combustion and Flame*, 156(10):1957–1970, 2009. 57

[128] S. Kartheekeyan and S. R. Chakravarthy. An experimental investigation of an acoustically excited laminar premixed flame. *Combustion and Flame*, 146:513–529, 2006. 57, 64

[129] S. J. Shanbhogue and T. C. Lieuwen. Response of a rod stabilized, premixed flame to longitudinal acoustic forcing. In *ASME Turbo Expo GT2006-90302, 2006*, 2006. 57, 64

[130] S. Santosh, D. H. Shin, S. Hemchandra, D. Plaks, and T. Lieuwen. Flame sheet dynamics of bluff-body stabilized flames during longitudinal acoustic forcing. *Proceedings of the Combustion Institute*, 32:1787–1794, 2009. 57, 64

[131] J. O'Connor and T. Lieuwen. Further characterization of the disturbance field in a transversely excited swirl-stabilized flame. *Journal of Engineering for Gas Turbines and Power*, 134(1), 2012. 58, 64

[132] J. O'Connor and T. Lieuwen. Disturbance field characteristics of a transversely excited burner. *Combustion Science and Technology*, 183(5):427–443, 2011. 58, 64

[133] J. O'Connor and T. Lieuwen. Recirculation zone dynamics of a transversely excited swirl flow and flame. *Physics of Fluids*, 24(7):075107–075107–30, 2012. 58

[134] L. Kabiraj and R. I. Sujith. Investigation of subcritial instability in ducted premixed flames. In *ASME Turbo Expo GT2011-46155, 2011*, 2011. 58, 61

[135] C. A. Kennedy and M. H. Carpenter. Several new numerical methods for compressible shear-layer simulations. *Applied Numerical Mathematics*, 14:397–433, 1994. 59

[136] S. Hemchandra. Premixed flame response to equivalence ratio perturbations: Comparison between reduced order modelling and detailed computations. *Combustion and Flame*, 159:3530–3543, 2012. 59, 60

[137] G. Lacaze, E. Richardson, and T. Poinsot. Large eddy simulation of spark ignition in a turbulent methane jet. *Combustion and Flame*, 156(6):1993–2009, 2009. 59

[138] B. J. McBride, S. Gordon, and M. A. Reno. Coefficients for calculating thermodynamic and transport properties of individual species. Technical report, NASA TM 4513, 1993. 60

[139] C. R. Wilke. A viscosity equation for gas mixtures. *Chemical Physics*, 18:517–519, 1950. 60

[140] S. Mathur, P. K. Tondon, and S. C. Saxena. Thermal conductivity of binary, ternary and quaternary mixtures of rare gases. *Molecular Physics*, 12:569, 1967. 60

[141] L. Kabiraj and R. I. Sujith. Nonlinear self-excited thermoacoustic oscillations: intermittency and flame blowout. *Journal of Fluid Mechanics*, 713:376–397, December 2012. 61

[142] D. Durox, F. Baillot, G. Searby, and L. Boyer. On the shape of flames under strong acoustic forcing: a mean flow controlled by an oscillating flow. *Journal of Fluid Mechanics*, 350:295–310, 1997. 67

[143] V. N. Kornilov. *Experimental research of acoustically perturbed bunsen flames*. PhD thesis, Eindhoven University of Technology, 2006. 68, 69

[144] T. Poinsot and S. M. Candel. A nonlinear model for ducted flame combustion instabilities. *Combustion Science and Technology*, 61(4-6):121–153, 1988. 76

[145] S. B. Margolis. Nonlinear stability of combustion-driven acoustic oscillations in resonance tubes. *Journal of Fluid Mechanics*, 253:67–67, 1993. 76

[146] S. Hemchandra and T. Lieuwen. Local consumption speed of turbulent premixed flames–an analysis of “memory effects”. *Combustion and Flame*, 157(5):955–965, 2010. 77

[147] P. G. Drazin. *Nonlinear systems*. Cambridge University Press, 1992. 78

[148] P. Manneville. *Instabilities, chaos and turbulence*, volume 1. Imperial College Press, 2010. 78

[149] P. Bergé, Y. Pomeau, C. Vidal, and L. Tuckerman. *Order within chaos: towards a deterministic approach to turbulence*. Wiley New York, 1986. 78, 99, 114

[150] P. Ashwin and M. Timme. Unstable attractors: existence and robustness in networks of oscillators with delayed pulse coupling. *Nonlinearity*, 18(5):2035, 2005. 79, 94

[151] H. Kantz and T. Schreiber. *Nonlinear time series analysis*. Cambridge University Press, 2000. 79, 80, 93, 102, 104, 114

[152] R. Hegger, H. Kantz, and T. Schreiber. Practical implementation of nonlinear time series methods: The TISEAN package. *Chaos*, 9(2):413–435, 1999. 79, 92, 102

[153] F. Takens. Detecting strange attractors in turbulence. In *Dynamical systems and turbulence, Warwick 1980*, pages 366–381. Springer, 1981. 79, 80

[154] H. D. I. Abarbanel. *Analysis of observed chaotic data*. Springer-Verlag New York, 1996. 79

[155] A. M. Fraser and H. L. Swinney. Independent coordinates for strange attractors from mutual information. *Physical Review A*, 33(2):1134–1140, 1986. 79

[156] M. B. Kennel, R. Brown, and H. D. I. Abarbanel. Determining embedding dimension for phase-space reconstruction using a geometrical construction. *Physical review A*, 45(6):3403, 1992. 80

[157] P. Grassberger and I. Procaccia. Characterization of strange attractors. *Physical review letters*, 50(5):346–349, 1983. 80, 92

[158] H. Kantz. A robust method to estimate the maximal Lyapunov exponent of a time series. *Physics letters A*, 185(1):77–87, 1994. 80, 102

[159] R. Balachandran, A. P. Dowling, and E. Mastorakos. Non-linear response of turbulent premixed flames to imposed inlet velocity oscillations of two frequencies. *Flow, Turbulence and Combustion*, 80(4):455–487, 2008. 85

[160] Bruno Eckhardt, Tobias M Schneider, Bjorn Hof, and Jerry Westerweel. Turbulence transition in pipe flow. *Annual Review of Fluid Mechanics*, 39:447–468, 2007. 94

[161] J. F. Gibson, J. Halcrow, and P. Cvitanović. Equilibrium and travelling-wave solutions of plane couette flow. *J. Fluid Mech.*, 638(1):243–266, 2009. 95

[162] J. P. Eckmann. Roads to turbulence in dissipative dynamical systems. *Reviews of Modern Physics*, 53(4):643–654, 1981. 97, 99

[163] E. Ott. *Chaos in dynamical systems.* Cambridge University Press, 2002. 97

[164] J. Argyris, G. Faust, and M. Haase. Routes to chaos and turbulence: A computational introduction. *Philosophical Transactions of the Royal Society of London. Series A: Physical and Engineering Sciences*, 344(1671):207–234, 1993. 97

[165] J. P. Gollub and S. V. Benson. Many routes to turbulent convection. *Journal of Fluid Mechanics*, 100(3):449–470, 1980. 97, 99

[166] A. Libchaber. From chaos to turbulence in Benard convection. *Proceedings of the Royal Society of London. A. Mathematical and Physical Sciences*, 413(1844):63–69, 1987. 97

[167] D. Ruelle and F. Takens. On the nature of turbulence. *Communications in Mathematical Physics*, 20(3):167–192, 1971. 99

[168] S. Newhouse, D. Ruelle, and F. Takens. Occurrence of strange Axiom A attractors near quasi periodic flows on m-tori, m greater than or equal to 3. *Communications in Mathematical Physics*, 64(1):35–40, 1978. 99

[169] J. B. McLaughlin and S. Orszag. Transition from periodic to chaotic thermal convection. *Journal of Fluid Mechanics*, 122:123–142, 1982. 99

[170] J. P Gollub and H. L. Swinney. Onset of turbulence in a rotating fluid. *Physical Review Letters*, 35(14):927–930, 1975. 99

[171] P. R. Fenstermacher, H. L. Swinney, and J. P. Gollub. Dynamical instabilities and the transition to chaotic Taylor vortex flow. *Journal of Fluid Mechanics*, 94(01):103–128, 1979. 99

[172] A. M. Guzman and C. H. Amon. Transition to chaos in converging–diverging channel flows: Ruelle–Takens–Newhouse scenario. *Physics of Fluids*, 1994. 99

[173] A. M. Guzman and C. H. Amon. Dynamical flow characterization of transitional and chaotic regimes in converging–diverging channels. *Journal of Fluid Mechanics*, 321(1):25–57, 1996. 99

[174] G. Penelet and T. Biwa. Synchronization of a thermoacoustic oscillator by an external sound source. *American Journal of Physics*, 81:290, 2013. 111

[175] M. Abel, K. Ahnert, and S. Bergweiler. Synchronization of sound sources. *Physical Review Letters*, 103(11):114301, 2009. 111

[176] J. W. S. Rayleigh. *The theory of sound Vol. I.* New York: Dover, 1945. 111

[177] V. S. Anishchenko, V. Astakhov, and T. Vadivasova. *Nonlinear dynamics of chaotic and stochastic systems: tutorial and modern developments.* Springer, 2007. 111

[178] P. Holmes and D. R. Rand. Bifurcations of the forced van der Pol oscillator. *Quarterly of Applied Mathematics*, 35(495–509), 1978. 111

[179] L. K. B. Li and M. P. Juniper. Lock-in and quasiperiodicity in hydrodynamically self-excited flames: Experiments and modelling. *Proceedings of the Combustion Institute*, 2012. 111, 125, 126, 127, 137, 142

[180] K. Rompala, R. Rand, and H. Howland. Dynamics of three coupled van der pol oscillators with application to circadian rhythms. *Communications in Nonlinear Science and Numerical Simulation*, 12(5):794–803, 2007. 111

[181] P. Hovel. *Control of complex nonlinear systems with delay*. Springer, 2010. 111

[182] R. Chacon. Maintenance and suppression of chaos by weak harmonic perturbations: a unified view. *Physical Review Letters*, 86(9):1737, 2001. 111

[183] E. Lubarsky, D. Shcherbik, A. Bibik, and B. T. Zinn. Active control of combustion oscillations by non-coherent fuel flow modulation. *AIAA Journal*, 3180(9), 2003. 111

[184] A. M. Annaswamy. Nonlinear modeling and control of combustion dynamics. In *Control of Fluid Flow*, pages 95–121. Springer, 2006. 111

[185] S. J. Illingworth and A. S. Morgans. Adaptive feedback control of combustion instability in annular combustors. *Combustion Science and Technology*, 182(2):143–164, 2010. 111

[186] D. Gabor. Theory of communication. *Journal of the Institution of Electrical Engineers (London)*, 3:429–457, 1946. 114

[187] J. N. Little and L. Shure. *Processing Toolbox for Use with MATLAB*. Mathworks, Natick, MA, 1992. 114

[188] A. Balanov, N. Janson, and D. Postnov. *Synchronization: from simple to complex*. Springer, 2009. 116, 117, 118, 120

[189] J. E. Walsh, G. L. Johnston, R. C. Davidson, and D. J. Sullivan. Theory of phase-locked regenerative oscillators with nonlinear frequency-shift effects. In *OE/LASE'89, 15-20 Jan., Los Angeles. CA*, pages 161–169. International Society for Optics and Photonics, 1989. 124

[190] S. C. Chen. Growth and frequency pushing effects in relativistic magnetron phase-locking. *IEEE Transactions on Plasma Science*, 18(3):570–576, 1990. 124

[191] A. H. Nayfeh and D. T. Mook. *Nonlinear oscillations*. Wiley, New York, 2008. 127

[192] J. Belair and L. Glass. Self-similarity in periodically forced oscillators. *Physics Letters A*, 96(3):113–116, 1983. 130

[193] L. Glass, M. R. Guevara, J. Belair, and A. Shrier. Global bifurcations of a periodically forced biological oscillator. *Physical Review A*, 29(3):1348, 1984. 130

[194] A. Venkatesan and M. Lakshmanan. Bifurcation and chaos in the double-well Duffing–van der Pol oscillator: Numerical and analytical studies. *Physical Review E*, 56(6):6321, 1997. 131

[195] B. van der Pol and J. van der Mark. Frequency demultiplication. *Nature*, 120(3019):363–364, 1927. 132

[196] J. M. G. Miranda. *Synchronization and control of chaos: an introduction for scientists and engineers*. Imperial College Press, 2004. 134, 144

[197] S. R. Stow and A. P. Dowling. Low-order modelling of thermoacoustic limit cycles. *ASME Turbo Expo ASME GT2004-54245*, 2004. 143

[198] S. R. Stow and A. P. Dowling. A time-domain network model for nonlinear thermoacoustic oscillations. *ASME Turbo Expo ASME GT2008-50770*, 2008. 143

[199] B. Schuermans. *Modeling and control of thermoacoustic instabilities*. PhD thesis, EPFL, Switzerland, 2003. 143

[200] R. Balachandran, B. O. Ayoola, C. F. Kaminski, A. P. Dowling, and E. Mastorakos. Experimental investigation of the nonlinear response of turbulent premixed flames to imposed inlet velocity oscillations. *Combustion and Flame*, 143(1):37–55, 2005. 143